Two-dimensional (2D) MXene as the Building Block of Three-dimensional (3D) Ordered Electrode Architectures and Their Application in Energy Storage Systems

by

Jafar Orangi

A doctoral dissertation thesis submitted to the Graduate Faculty of
Auburn University
in partial fulfillment of the
requirements for the Degree of
Doctor of Philosophy

Auburn, Alabama
December 12, 2020

Keywords: Two-Dimensional Transition Metal Carbides, MXenes, 3D structure, 3D printing, Ordered Structure, Electrochemistry

Approved by
Majid Beidaghi, Chair, Professor of Materials Engineering
Virginia A. Davis, Professor of Chemical Engineering
Dong-Joo Kim, Professor of Materials Engineering
Pengyu Chen, Professor of Materials Engineering
Minseo Park, Professor of Physics

Abstract

Transition metal carbides and nitrides (MXenes) are an emerging class of two-dimensional (2D) materials with interesting properties that have gained enormous attention since their discovery in 2011. Extensive theoretical and experimental research effort has been devoted to this family of materials in various research fields, including energy storage, hydrogen evolution reaction, sensors, water purification, and catalysis due to their unique morphologies properties and diverse chemistries. To date, while $Ti_3C_2T_z$ is the most studied member of the MXene family, other members, including Ti_2CT_z, Nb_2CT_z, $Nb_4C_3T_z$, $Mo_{1.33}CT_z$, $Mo_2TiC_2T_z$, etc. due to their unique electrochemical performance, have been widely and extensively studied for energy storage applications. Similar to other 2D materials, MXenes suffer from restacking, which limits their electrochemical performance. Restacking blocks the ionic transport channels, resulting in inadequate electrolyte access to the active redox sites, hence reducing the electrochemical performance of the electrode material. Thus, designing electrode architectures with a predominant aim to inhibit restacking while being cost-effective and straightforward is of great importance. Employment of new fabrication methods such as additive manufacturing could offer a simple yet effective route to address the current problems and advance the engineering of the electrode structure. I shed light on the importance of structure on electrochemical performance, fabrication of advanced electrode materials, and introduce enlightening progress for effective structural design, and provide perspective and possible opportunities for MXene to get closer to be considered for practical applications and broaden its application in fields beyond energy storage.

Dedications

To my mother Soheila and my father Kuruosh

for all the sacrifices you made during all these years

for the unconditional love and support.

You were not here, but I always felt you in my heart

missed you more than anything in this world.

To Sahar and Soroor

for being with me, supporting me, and listening to me

Thanks you for your love, support, motivation, and understanding during all these years

Acknowledgments

The research presented in this study would not have been possible without many individuals' help and guidance. For this, I would like to express my dearest gratitude to everyone who supported me during my research.

First, I would like to thank my advisor, Dr. Majid Beidaghi, for his support, guidance, and advice since the beginning of my study at Auburn University. Thank you for always being there to help. I am also thankful to my fellow friends in the department, particularly my group members, who have always helped me in different situations. I am also grateful to my fellow researchers and friends that I am actively collaborating on various research projects.

I would like to thank Dr. Virginia A. Davis for her help and valuable insights during my Ph.D. I would like to express special gratitude to the committee members Prof. Dong-Joo Kim, Dr. Pengyu Chen, and Prof. Minseo Park, for their time to review this work and their helpful comments. Special thanks to Steve and Cheryl, who was always there when help was needed.

I would like to thank my friends and collaborators, Dr. Armin VahidMohammadi, Emre Kayali, Hengze (Kane) Chen, Fatima Hamadi, Mackenzie Bockhold, Halil Tetik, Dr. Lin, Dr. Hosein Talebinezhad, and Ali Rashti for their help and support during these years.

Lastly, I would like to express my most profound appreciation to my family and my friends. Because of you and your steady support, I had an enjoyable experience abroad, and Auburn became my second home.

I appreciate the support from the Graduate Research Scholars Program (GRSP) doctoral fellowship (GRSP) rounds 12-14, from The Alabama Established Program to Stimulate Competitive Research (ALEPSCoR).

Table of Contents

List of Tables

List of Figures

List of Abbreviations

2D	2-dimensional
3D	Three-dimensional
LDH	Layered double hydroxides
TMOs	Transition metal oxides
TMDs	Transition metal dichalcogenides
CNTs	Carbon nanotubes
GO	Graphene oxide
rGO	Reduced graphene oxide
LiF	Lithium fluoride
HF	Hydrofluoric acid
CTAB	Cetrimonium bromide
SDS	Sodium dodecyl sulfate
CNCs	Cellulose nanocrystals
CNFs	Carboxymethylated cellulose nanofibrils
BC	Bacterial cellulose
EG	Exfoliated graphene
PPy	Pyrrole
PEDOT:PSS	Poly(3,4- ethylenedioxythiophene):poly(styrenesulfonic acid)
THF	Tetrahydrofuran
EC	Ethylene carbonate
DEC	Diethyl carbonate

PC	Propylene carbonate
FEC	Fluoroethylene carbonate
AgNWs	Silver nanowires
SA	Sodium ascorbate
EDA	Ethylenediamine
PVA	Polyvinyl alcohol
SAP	Super absorbing polymers
HCl	Hydrochloric acid
TAEA	Tris(2-aminoethyl) amine
EDLCs	Electrochemical double-layer capacitors
MSC	Microsupercapacitor
CV	Cyclic voltammetry
EIS	Electrochemical impedance spectroscopy
GCD	Galvanostatic charge-discharge
VAF	Vacuum-assisted filtration
LbL	Layer-by-layer
SSLbL	Spin spray layer-by-layer
DIW	Direct ink writing
XRD	X-ray diffraction
XPS	X-ray photoelectron spectroscopy
FTIR	Fourier-transform infrared spectroscopy
AFM	Atomic Force Microscope
TEM	Transmission electron microscopy

Chapter 1

Introductions

Clean energy conversion and storage technologies have become a critical concern to be solved, mainly due to the increase of severe pollution issues and ever-increasing demand for energy. To address these issues, electrochemical capacitors (ECs) have been gaining attention as energy storage devices due to their high power density, long cycle life, and fast charge-discharge rate.[1–3] Electrode material intrinsic properties, including charge storage mechanism, is of great importance. On the other hand, electrodes' architectures, which affect the surface area, electrical conductivity, and mechanical property, play a significant role in maximizing the energy and power densities.[4] 2-dimensional (2D) materials have the potential to improve advanced ECs performances, due to their large surface area to volume ratios and plenty of electrochemically active surfaces. [1–3] 2D materials such as graphene, black phosphorus, transition metal dichalcogenides, covalent organic frameworks, hexagonal boron nitride, layered double hydroxides (LDH), metal-organic frameworks, transition metal oxides (TMOs), and MXenes showed unparalleled electronic, optical, and physiochemical properties from the bulk counterparts.[5–11] Based on the application, each of the mentioned materials has its superiorities and

drawbacks. For example, MXene offers a highly conductive network and facile ionic diffusion pathways when used as electrode material for ECs.[2,4,12] They can form binder-free freestanding films with improved capacitance and rate capability. [2,4,12]

Several theoretical and experimental studies claimed that, through exfoliation, numerous stable dispersions of 2D sheets could be formed.[2,13,14] MXenes were the first examples of 2D materials produced by selective extraction of strongly bonded layered crystal structures. This distinguishes MXenes from other 2D materials such as graphene, MoS_2, and h-BN, where their bulk counterparts have weakly bonded van der Waals layered structures and can be easily exfoliated to 2D flakes through sonication in liquids or by mechanical separation.

Assembling 2D materials into functional three-dimensional (3D) structures is an attractive method to extend the applications of these materials in various fields.[4,15–17] The advantage of assembling 2D materials in 3D structures has been previously demonstrated by the integration of graphene sheets in hydrogels, aerogels or foams. Interesting physical properties, such as high specific surface area, rich porosity, and low density of such 3D structure with interconnected 3D networks, have been studied and challenged comprehensively in various fields and applications, including catalysis, stretchable electronics, supercapacitors, and environmental protection.[5,18–21] However, a great challenge for further implementing these materials in functional applications is developing methods to engineer their architecture into structures with enhanced ionic and electronic transport and improved mechanical properties that can meet the requirements of practical applications.

For my Ph.D. research, I plan to synthesize, fabricate, and engineer advanced 3D electrode architectures based on 2D MXenes and investigated their electrochemical response in energy storage systems.

The goal of the proposed research is twofold: first, synthesis of functional additive-free water-based MXene ink, which for the first time, enables us to employ extrusion-based 3D printing to fabricate energy storage devices with unique electrode structure. Second, study the effect of synthesis parameters on the 3D MXene-based aerogel's microstructure fabricated by low cast freeze casting technique and investigate the microstructure effects on the aerogel's electrochemical properties. In the following chapter, I will provide more detail regarding the background of MXene, and I will present a literature review about 2D MXenes properties and their applications. Then, I will explain the experimental methods, and discuss the details of my research outcome. At the end, I will discuss the outlook and future impacts of this research.

Chapter 2

Background and Literature Survey

Advanced technologies for efficient storage of electrical energy are critical for large-scale utilization of renewable energy sources as well as the evolution of wearable electronics and electric vehicles.[22–27] ECs are reliable energy storage devices known for their high power density, long cycle life, and fast charge-discharge rates.[1,8,28] The electrochemical properties of ECs are determined, on the one hand, by the intrinsic properties of their electrode materials, including their electrical properties and charge storage mechanism. On the other hand, the morphology of the electrodes plays a significant role in their electrochemical properties by impacting the electrode's accessible surface area, electrical and ionic conductivities, and mechanical properties.[29–32] The content of this chapter has been published in the Journal of Advanced Functional Materials and required copy right permission is obtained.[4]

Conventional ECs, electrochemical double-layer capacitors (EDLCs), store charge in a double-layer formed at the interface of a high surface area carbon material and the electrolyte. This physical charge storage mechanism limits the energy density of EDLCs. Therefore, it is expected that future ECs with high energy and power densities will be based on materials capable of storing charge by pseudocapacitive mechanism or fast redox reactions. In recent years, two-dimensional

(2D) materials with high surface areas have been the forerunners in search of candidate electrode materials for advanced ECs.[2,33–35] Some 2D materials offer an abundance of electrochemically active surfaces, which, combined with high electrical conductivity, leads to fast electrochemical charge storage and high energy and power densities of the electrodes.[2,18,35,36] 2D transition metal carbides and nitrides, MXenes, are prime examples of such electrode materials.

Within a few years from their discovery, the family of MXenes has expanded to about 30 members with different chemical compositions and properties. Some of the most studied MXene compositions are $Ti_3C_2T_z$, Ti_2CT_z, V_2CT_z, Nb_2CT_z, and Mo_2CT_z.[2,13] The experimental and theoretical research on properties of 2D MXene has rapidly expanded in the past few years and MXenes are considered for applications such as energy storage, electronics and optoelectronics, sensors, water purification, and catalysis.[12,37–40] However, the properties of MXenes as electrode materials for energy storage devices has received the most attention so far. This is because the combination of the relatively high surface areas, 2D or layered structure, high electrical conductivities (for most MXene compositions), and functionalized transition metal surfaces leads to high energy and power density of MXene electrodes.[2,12,41,42] Particularly, these materials have shown outstanding performances as electrode materials for ECs with higher volumetric capacitances compared to other electrode materials, including high surface area carbon nanomaterials and pseudocapacitive transition metal oxides.[12,41]

The charge storage mechanism of MXene is a type of pseudocapacitive storage and is based on the fast intercalation of ions between the MXene layers (intercalation pseudocapacitance). The storage mechanism is enabled by MXenes' conductive metal carbide core and functionalized oxide or hydroxide-like surfaces, [31,43] which gives rise to high energy density and specific capacitance without sacrificing cyclability and power density.[2,43–46] Several recent studies have confirmed this

charge storage mechanism.[45–51] For example, *in situ* X-ray absorption spectroscopy studies have shown the change in the oxidation state of Ti in $Ti_3C_2T_z$ MXene during charge and discharge of the electrodes, confirming that surface transition metal participates in redox reactions.[45] While the intrinsic electrochemical properties of MXenes is promising, the final properties of the electrodes are considerably affected by their structure and morphology, which are, for the most part, controlled by the method used for the assembly of 2D MXene sheets and the electrode fabrication method. The morphology and structure also crucially impact the electrochemical performance of hybrid electrodes of MXenes and other materials.

Hierarchical architectures based on MXenes have recently gained attention for designing new electrode materials that harness the synergetic effects of MXene and other nanomaterials **(Figure 2-1).**[31,35,52,53,5,54,55] Hybrids electrodes of MXene with carbon nanotubes (CNTs), reduced graphene oxide (rGO), TMOs, and transition metal dichalcogenides have been reported in recent years.[15,16,30,56–68]The properties of these hybrid electrode materials are also dependent on their structural features and often can be controlled during assembly processes.[5,53] Thus, in this paper, after highlighting the importance of electrode structure and assembly method on the electrochemical performance of MXene electrodes, we will review the recent progress in the design and assembly of MXene electrodes with a focus on electrodes used for EC applications.

2.1 Synthesis of single layer MXene flakes

Although the MXene synthesis process and its effects on the electrochemical performance is not the focus of this review, it is important to discuss the synthesis process briefly. The composition, surface chemistry, lateral size, and thickness dictate the performance of MXenes for various applications.[2,38,69–71] In most common synthesis processes of MXenes, controlling the dimensions of MXene flakes and their surface chemistry is difficult, hindering the systematic

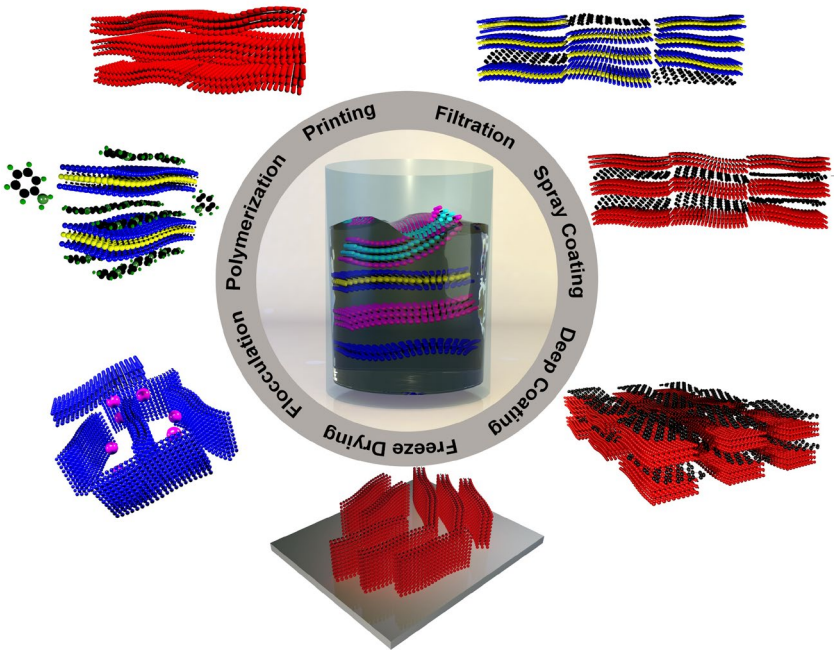

Figure 2.1. Schematic drawing showing some of the reported assembly and fabrication methods used in the fabrication of electrodes based on MXene and their hybrids with other nanomaterials. The assembly method has an immense effect on the electrode architecture.

investigation of the effects of these parameters on the electronic, electrochemical, and mechanical properties of these materials. Several recently published papers have addressed the MXene synthesis process and strategies to control the dimension of single-layer flakes and the readers are encouraged to review these papers for a more detailed discussion.[2,42,69,72]

The synthesis processes used to produce MXenes are somewhat vary depending on the specific compositions. For $Ti_3C_2T_z$, several synthesis routes are proposed so far, and the produced materials are studied for various applications.[46,69] However, the most common process for the synthesis of single-layer flakes of $Ti_3C_2T_z$ is a one-step etching and delamination process which uses a mixture of lithium fluoride (LiF) and hydrochloric acid as the etchant.[2,42,69,71,73,74] It is reported that the concentration of the etchant and etching temperature have a significant effect on the lateral size and presence of defects in the $Ti_3C_2T_z$ flakes synthesized with this method.[42,72,74] The MXene

flakes synthesized in this process usually show lateral dimensions ranging from a few microns to a few hundred nanometers.[42,44,46,72] Recent reports indicate that the process can be modified to produce single-layer $Ti_3C_2T_z$ flakes as large as 15μm.[46]

The electrochemical performance of MXenes, in particular $Ti_3C_2T_z$, has been shown to be directly affected by the lateral dimensions of the produced flakes.[42,72,74] For example, freestanding films produced using larger flakes possess higher electrical conductivity due to less interfacial contact resistance than the ones fabricated using smaller flakes. On the other hand, the films fabricated using smaller flakes offer higher ionic conductivity as they contain more diffusion paths for electrolyte ions. Since early studies of the properties of single-layer MXene flakes, the electrodes fabricated by VAF has been dominantly used to study the electrochemical properties of these materials. Usually, VAF is used to fabricate compact MXene "papers" which are flexible and can be directly used as electrodes in ECs and other energy storage devices.[2,42,122] In these freestanding and densely packed films, MXene flakes are aligned horizontally.[42,72,75] It is demonstrated that the engineering of the electrode structures to contain a mixture of small and large flakes results in improved electrochemical performance of the MXene electrodes.[42] Therefore, flake size is of great importance when comparing the electrochemical performance of MXene electrodes.[42]

V_2CT_z, Mo_2CT_z, $Cr_2TiC_2T_z$, $Mo_2TiC_2T_z$, $Mo_2Ti_2C_3T_z$, and many other MXenes, are usually synthesized through a two-step synthesis process.[32,76–79] The first step is the removal or etching of A layer atoms from the structure of their precursor MAX phases (for example, etching Al atoms from V_2AlC) to produce multilayered MXene (ML-MXene).[32] This etching process is usually performed in concentrated hydrofluoric acid (HF) solutions, although alternative etching approaches have been studied recently.[2,80] The second step in the synthesis process is the

delamination of ML-MXene particles to produce single- or few-layer flakes.[32] This step usually involves pre-intercalation of ML-MXene with large organic molecules, such as tetrabutylammonium hydroxide (TBAOH), to increase the interlayer spacing and to facilitate the separation of layers when the particles are dispersed in water or organic solvents.[2,76]

As mentioned above, the current synthesis methods for almost all MXenes involve etching the precursor materials (MAX phases or other materials) in fluoride-containing acidic solutions. Generation of -F surface groups, unwanted etching of the transition metal element (due to low selectivity towards A-layer atoms), and being environmentally unfriendly are the main problems in these synthesis processes.[2,69,81–83] Moreover, it has been reported that AlF_3, one of the byproducts of the etching reaction, when the A-layer atom is Al, is hard to be eliminated from the mixture under mild conditions.[81] Therefore, recently, many attempts to develop fluoride-free synthesis strategies have been reported.[84–89] Currently, both theoretical and experimental studies show that -F surface groups on MXene flakes inversely affect the change storage process.[90,91] Until reliable alternative etching methods are developed, post-synthesis treatments for removal of -F surface groups can be considered.[2,92–95]

2.2 The impact of electrode structure on electrochemical properties

The impacts of structure and morphology on the electrochemical properties of electrodes have been the subject of much research in the energy storage field.[96–101] When the electrode material is a 2D material, the morphology of the electrode can significantly affect its electronic and ionic conductivities. In the case of solution-processed 2D materials such as rGO and MXene, the 2D flakes tend to restack to form multilayers during various stages of materials synthesis and electrode fabrication process. This significantly limits the accessibility of electrolyte ions to the electrode surfaces,[35,16,102–104,57,105,52,53] leading to a fading capacitive performance at high charge/discharge

rates.[12,41,42,106] Therefore, engineering the structure of the electrodes to prevent restacking through novel material assembly and electrode fabrication processes have been a major theme of research in this area. For example, it has been shown that the assembly of $Ti_3C_2T_z$ MXene in electrode with 3D structures or pre-intercalation of MXene layers with electrolyte ions could significantly influence the rate capability of the electrodes.[12,107] Due to the improved ion accessibility to the redox-active sites and the high electronic conductivity of the electrodes, they could be charged and discharged at rates significantly higher than those of conventional EDLCs (up to 100 V s^{-1}), while maintaining higher volumetric and areal capacitances than the best performing EDLC and pseudocapacitive materials.[12] Similar high rate performances have been reported for templated porous structures and MXene aerogels.[12,107] However, the hydrogel, aerogel, and other porous electrodes share some drawbacks. Firstly, the lower density of these electrodes will generally reduce their volumetric capacitances, which is one of the main attributes of MXene electrodes. Also, the interconnectivity of the 2D flakes and the formation of a conductive network in the structure is often a limiting factor that may hinder the overall performance of the electrodes.

Designing the electrode structure with vertically aligned 2D sheets is another approach to improve ionic and electronic transport properties. Although this approach is technically challenging, a few studies have shown the promise of this morphology on the overall performance of the electrode. Most notably, Xia et al. demonstrated that the vertical alignment of 2D $Ti_3C_2T_z$ enables unimpeded directional ion transport and leads to the thickness-independent electrochemical performance of the MXene electrodes.[108]

Heterostructures and hybrids of MXenes with other nanomaterials have shown promising performances as electrodes for energy storage devices.[9,58,66,109–113] In these hybrid electrode structures, the secondary component prevents the restacking of MXene flakes while its

agglomeration is prohibited by MXene flakes, resulting in enhanced ion transport properties. The electrochemical performance of the electrodes fabricated using this approach is dependent on the electronic and electrochemical properties of the secondary component, its amount, and the method of assembling the components into a robust electrode structure.[2,69,114] Recently, the research efforts have been focused on studying the properties of heterostructures of MXenes and other 2D materials. The research in this direction is motivated by theoretical studies that have explored the properties of 2D heterostructures based on MXenes.[109,115,116] For example, first-principle calculations on Ti_2CT_z/graphene heterostructure has revealed that graphene, while preventing the restacking of MXene layers, improves the electronic conductivity, mechanical properties, and Li-ion absorption of the heterostructure.[15] 2D heterostructures of Ti_2CT_z and 2H MoS_2 (Ti_2CT_z/2H MoS_2) is another theoretically studied electrode material for energy storage devices.[117–119] First-principle calculations by Shao et al. have suggested that these heterostructures have a reduced diffusion barrier for Li-ions, and an enhanced diffusion coefficient, electrical conductivity, and mechanical flexibility.[118] In another study, Li et al. showed that diffusion barriers of MoS_2/Ti_2CT_2 (T = F, O) heterostructure for Li^+ and Na^+ ions are less than 0.57 eV and 0.37 eV, respectively, which are comparable to values calculated for MXene/graphene heterostructures.[119]

It is clear that engineering the electrode structure is the key to achieving MXene-based electrodes with high energy and power densities. The electrode structure is directly impacted by the electrode fabrication method and MXene assembly processes. Therefore, it is important to review the current understanding of the relationship between the assembly and electrode fabrication process with the structure and properties of the electrodes.

2.3 Assembly processes and electrode fabrication methods

As mentioned above, due to their functionalized surfaces, 2D MXene flakes can be easily dispersed in water and some organic solvents to prepare stable dispersions. Therefore, MXene electrodes can be fabricated through solution-based processes. These processes usually offer high yields at lower costs, while providing a high level of control over various parameters, such as the composition of the electrode and the spatial arrangement and orientation of MXene nanosheets in the electrode structure. Moreover, the availability of stable colloidal dispersions (or inks) of MXenes enables the utilization of cost-effective and scalable electrode fabrication methods such as printing or spray coating.[35,120,121] Furthermore, solution-based processes can be employed to fabricate simple hybrid electrodes composed of MXenes and other electroactive nanomaterials as well as more complex electrodes with periodically ordered 2D-2D heterostructures or vertically aligned nanosheets. In the following sections, we will review the current state-of-the-art in the solution-based electrode fabrication and MXene assembly processes.

2.4 Vacuum-assisted filtration (VAF) for the assembly of pristine and hybrid MXene films

Since early studies of the properties of single-layer MXene flakes, the electrodes fabricated by VAF has been dominantly used to study the electrochemical properties of these materials. Usually, VAF is used to fabricate compact MXene "papers" which are flexible and can be directly used as electrodes in ECs and other energy storage devices.[2,42,122] In these freestanding and densely packed films, MXene flakes are aligned horizontally. Freestanding and binder-free MXene/CNT films were the first of the reported hybrid electrodes fabricated by VAF and proved the effectiveness of this hybridizing strategy to improve electrode performance.[2,12,42,124] For example, $Ti_3C_2T_z$ and Nb_2CT_z-based electrodes were prepared by mixing the MXene dispersions with CNT dispersions

(stabilized with sodium deoxycholate surfactant) followed by VAF (.[12,42] MXene paper electrodes usually show very high volumetric capacitances when tested as EC electrodes, but they often suffer from low ionic conductivity in most electrolytes arising from the inevitable MXene flake self-restacking, resulting in capacitance fading at high scan rates.[12,44,105] However, as mentioned, incorporation of other nanomaterials such as CNTs, graphene, rGO, and metal oxide particles or nanobelts can improve the overall charge storage performance of the electrodes by effectively preventing the restacking of the MXene flakes.

To improve ionic conductivity and, in turn, electrochemical performance and study the effect of electrode morphology on MXene high rate performance, fabrication of electrode architectures via templating method was investigated. 3D microporous MXene films were fabricated via wrapping MXene ($Ti_3C_2T_z$ and Mo_2CT_z) around poly(methyl methacrylate) (PMMA) spheres due to the presence of surface hydroxyl groups.[12,107] The sacrificial templates were removed from the structure (annealing under inert atmosphere), leaving freestanding, flexible, and highly conductive MXene architecture.[12,107] Lukatskaya et al. showed that fabricated microporous films, in aqueous electrolyte, can deliver an outstanding capacitive performance (210 F g^{-1} at 10 V s^{-1}) and capacitance retention at a high charge-discharge rate (100 F g^{-1} at 40 Vs^{-1}).[12] In another study, Zhao et al. employed the same fabrication method to assemble the 3D microporous $Ti_3C_2T_z$ architectures. As the anode material for Na-ion storage, the fabricated electrodes showed improved electrochemical performance in terms of capacity, rate capability, and cycling stability compared with MXenes and MXene/carbon nanotube hybrid architectures.[107] Recently, Xu and coworkers employed the sulfur-template method to fabricate freestanding and highly conductive porous electrodes as anode material for Li-ion battery.[123] These flexible 3D porous MXene architecture delivered improved capacity (455.5 mAh g^{-1} at 50 mA g^{-1}), rate capability (101 mAh g^{-1} at 18 A

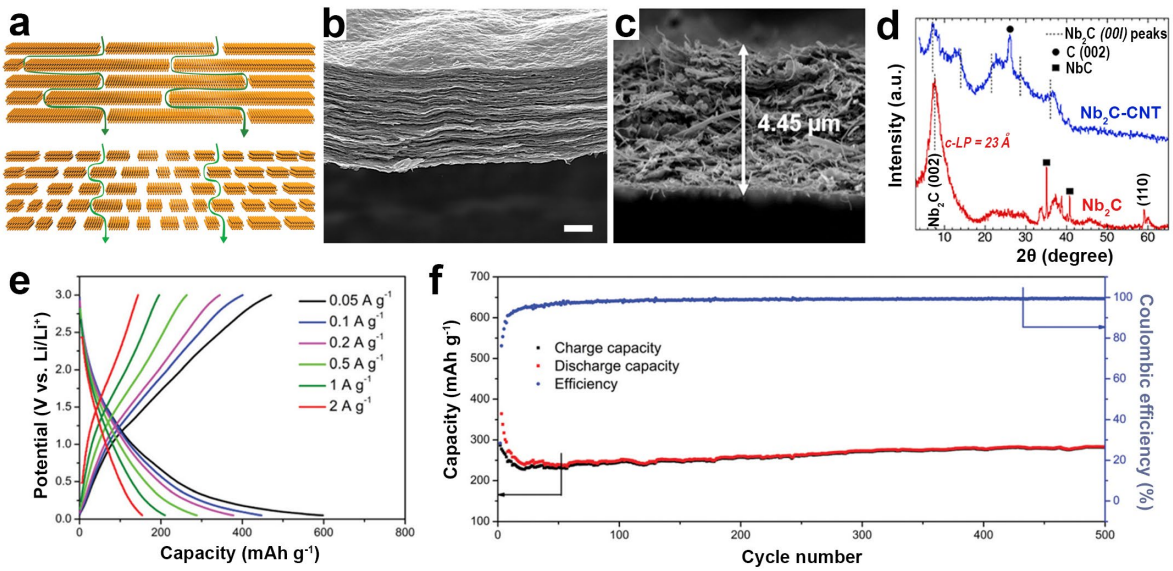

Figure 2.2. (a) Schematic drawing showing the effect of flake size on ion diffusion path in the structure of freestanding MXene film. Reproduced with permission [42] Copyright 2018, American Chemical Society. Cross-sectional SEM images of (b) a MXene film (scale bar 1µm) (Reproduced with permission [42] Copyright 2018, American Chemical Society), and (c) a MXene/CNT hybrid film prepared by VAF. (d) XRD pattern of Nb_2CT_z and Nb_2CT_z/CNT hybrid films showing the effect of CNT addition on the film structure. Reproduced with permission [61] Copyright 2016, Elsevier Ltd. (e) Charge–discharge curves of a $Ti_3C_2T_z$/CNT film at different current densities. (f) Cycling performance of a $Ti_3C_2T_z$/CNT film electrode at a current density of 0.5 A g^{-1}. Reproduced with permission from reference [125] Copyright 2018, Royal Society of Chemistry.

g^{-1}), and cycle stability (220 mAh g^{-1} at 1 A g^{-1} after 3500 cycles). Improving the ion transport through the fabrication of micropores in the structure, while preserving the good electrical conductivity can be accounted for the improved electrochemical performances.

Freestanding and binder-free MXene/CNT films were the first of the reported hybrid electrodes fabricated by VAF and proved the effectiveness of this hybridizing strategy to improve electrode performance.[2,12,42,124] For example, $Ti_3C_2T_z$ and Nb_2CT_z-based electrodes were prepared by mixing the MXene dispersions with CNT dispersions (stabilized with sodium deoxycholate

surfactant) followed by VAF **(Figure 2-2c).**[56,124] The X-ray diffraction (XRD) studies of the Nb_2CT_z and Nb_2CT_z/CNT hybrid films revealed that the presence of CNTs created a turbostratic structure by disrupting the crystallographic alignment of the Nb_2CT_z flakes **(Figure 2-2d).** In other words, while flakes were preserving crystallographic ordering along MXene (002) plane, they were restacked randomly along (110) plane.[56] Similar structures were observed for hybrid films of $Ti_3C_2T_z$ and CNTs.[56] When a $Ti_3C_2T_z$/CNT hybrid film was tested as the electrode in a Li-ion capacitor, an improved specific capacity (489 mAh g^{-1} for $Ti_3C_2T_z$/CNT at a current density of 50 mA g^{-1}) and cycling performance was observed.[56] The voltage profile of the hybrid electrodes showed no plateaus or any other sign that indicate the involvement of CNTs in the charge storage process **(Figure 2-2e).**[56,124] In both cases of the pure and hybrid electrodes, the shape of the charge-discharge curves resembled a capacitor-like behaver with a reversible Li-ion shuttling mechanism rather than a battery behavior. Also, a continuous increase in the capacity was observed for the $Ti_3C_2T_z$/CNT film, which can be related to the improved accessibility of electrolyte ions to the active redox sites at the surface of the individual MXene flakes **(Figure 2-2f).**

In a study by Xie et al., negatively charged $Ti_3C_2T_z$ flakes were mixed with both positively (cetrimonium bromide (CTAB) treated) and negatively (sodium dodecyl sulfate (SDS) treated) charged CNTs to fabricate porous MXene/CNT composite films.[46] The addition of CTAB treated CNTs (CTAB-CNTs) to the MXene dispersions led to precipitation of MXene/CTAB-CNTs hybrids while adding the negatively charged SDS treated CNTs resulted in the formation of a stable dispersion[16,59] Both dispersion were used in the fabrication of films using VAF and the fabricated films were tested for their Na-ion storage properties. The electrochemical performance of $Ti_3C_2T_z$/CTAB- CNT was superior to $Ti_3C_2T_z$/SDS-CNT and $Ti_3C_2T_z$ films, showing improved capacitive and cycling behavior.[16,59] The aggregation of MXene flakes upon adding the CTAB-

CNT solution implies a successful attachment of CNTs to $Ti_3C_2T_z$ flakes. This not only effectively prevents the restacking of MXene flakes, but also results in the formation of a conductive 3D structure with enhanced electrolyte diffusion properties.[16,59] Mo_2CT_z/CTAB-CNT films prepared using the same method also showed a similar enhancement of electrochemical properties compared to the pristine Mo_2CT_z electrodes.[16,59]

Cellulose nanocrystals (CNCs), carboxymethylated cellulose nanofibrils (CNFs), and bacterial cellulose (BC) fibers are examples of other 1D additives that are used as spacers to address the restacking problem in MXene films while enhancing their mechanical properties.[125,126] For practical applications, excellent electronic conductivity of MXene films should be combined with good mechanical properties. For example, flexible freestanding $Ti_3C_2T_z$/CNFs (10 wt%) hybrid film showed an improved combination of mechanical and electronic properties,[126] with high mechanical strength (154 MPa) and Young's modulus (41.9 GPa) in combination with high electric conductivity (690 S cm^{-1}) and high specific capacitance (325 F g^{-1}) **(Figure2-3 a-e).**[126] The pure MXene papers and the hybrid films fabricated using ~57 wt% BC showed a tensile strength of 21.3 MPa and 70.0 MPa and strain at the break of ~0.8% and ~15.5%, respectively.[125] While increasing the 1D CNFs or BC fibers content increased the *c*-lattice parameter, adding CNC to $Ti_3C_2T_z$ did not affect the XRD pattern suggesting that CNC was not effectively distributed between MXene sheets in the film structure.[125,126] In the case of $Ti_3C_2T_z$/CNFs electrodes, the improved mechanical properties were related to interfacial interaction by van der Waals forces and MXene flakes bridging due to the presence of long 1D fibers.[126] It is worth mentioning that the electrical conductivity of the fabricated films could be tailored to reach the desired conductivity by manipulating the additive ratio.[126]

The hybrid electrodes of MXene with CNFs and BC were used to fabricate planar microsupercapacitor (MSC), and their electrochemical properties were investigated under various conditions such as elongation, twisting, and bending. When tested using cyclic voltammetry (CV), the $Ti_3C_2T_z$/CNFs composite film showed a lower capacitance at low scan rates, but a higher capacitance at higher rates (over 100 mV s^{-1}) compared to pristine $Ti_3C_2T_z$ film, indicating its improved rate capability.[126] Although BC is an insulating additive, the hybrid $Ti_3C_2T_z$/BC films showed improved electrochemical performance with a higher specific capacitance (111.5 mF cm^{-2}) and rate capability compared to the pure MXene film **(Figure2-3f).**[125] The improved electrochemical performance of hybrid films of MXene and 1D nanomaterials are attributed to restacking prevention, facilitating ionic diffusion, and in the case of conductive additives, such as CNTs, providing electron transport paths between MXene flakes.[124,125]

Hybrid films and heterostructures of MXenes with other 2D materials have been fabricated and studied for energy storage applications.[61,109,113,127,128] Particularly, fabrication and electrochemical studies of hybrid films of $Ti_3C_2T_z$ and exfoliated graphene or rGO have been the subject of many studies.[129–131] In general, in these 2D hybrid films and heterostructures, the restacking of both 2D materials are prevented, and the ion accessibility of the films is improved. In many of the reported studies, MXene flakes with smaller size act as the active material between larger graphene or rGO sheets.[129–131] One example of such hybrid films is reported by Li et al., where ultrasonicated dispersions of $Ti_3C_2T_z$ in water was mixed with a dispersion of electrochemically exfoliated graphene (EG) followed by VAF.[132] It was suggested that the good mechanical properties of this hybrid film stem from the EG skeleton formed in its structure.[132] In the study by Li et al., the performance of the electrodes largely depended on their composition. On the one hand, as the $Ti_3C_2T_z$ content is reduced, the large EG flakes tend to aggregate, hindering ionic diffusion. On

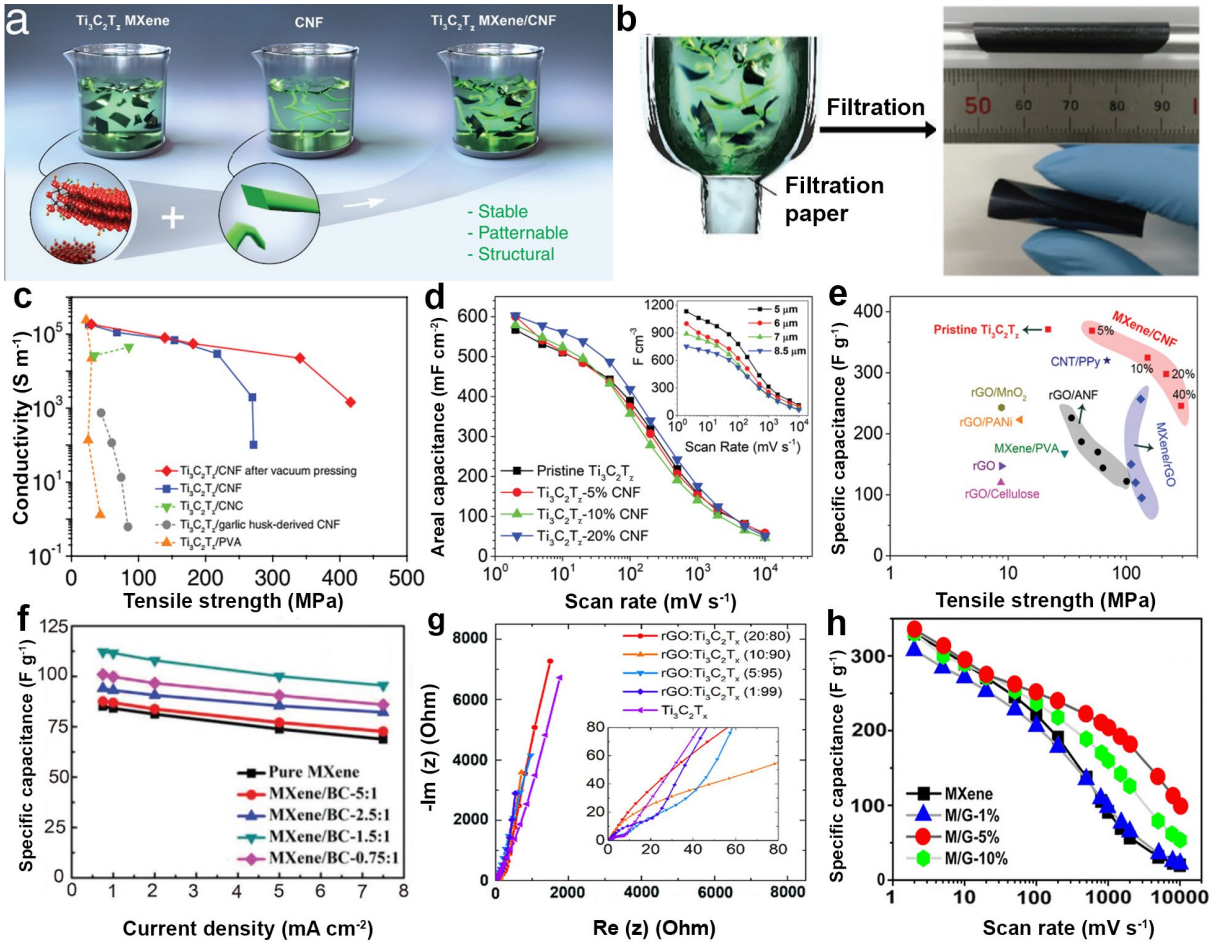

Figure 2.3. (a, b) Schematic drawings showing the fabrication process of freestanding $Ti_3C_2T_z$/CNF films and a digital photograph of a fabricated film. Reproduced with permission [65] Copyright 2017, WILEY-VCH. Reproduced with permission [126] Copyright 2019, Wiley-VCH. (c) Tensile strength versus conductivity for hybrid films of $Ti_3C_2T_z$ with various CNF content compared with other $Ti_3C_2T_z$ hybrid films. (d) Areal and volumetric capacitances of MXene/CNF hybrid film composites. (e) Capacitance versus mechanical strength of $Ti_3C_2T_z$/CNF films compared with some other notable reported multifunctional composites. Reproduced with permission [126] Copyright 2019, Wiley-VCH. (f) Areal capacitance of various MXene-based electrodes at various current densities. Reproduced with permission [125] Copyright 2019, Wiley-VCH. (g) Nyquist plots of pristine MXene and MXene-rGO composite electrodes. Inset: the high-frequency region of the Nyquist plot. Reproduced with permission [57] Copyright 2017, Wiley-VCH. (h) The rate capability of MXene/rGO (M/G) hybrid electrodes. Reproduced with permission [136] Copyright 2019, Wiley-VCH.

the other hand, due to the small size of the $Ti_3C_2T_z$ flakes used, the long-range electrical conductivity was reduced with increasing the MXene content. Compared with the pristine MXene or EG electrodes, a hybrid electrode of $Ti_3C_2T_z$:EG with a 3:1 weight ratio showed favorable electron transport properties and the best measured capacitive performance (3.2 mF cm^{-2} and 33 F cm^{-3} at 5 mV s^{-1}).[132]

Similarly, rGO is also an interesting candidate to be hybridized with MXene as it offers improved solution processability, large surface area, and possible surface modifications by functional groups. Another factor that makes MXene/rGO hybrids more interesting is the synergic contribution of different charge storage mechanism of EDLC and pseudocapacitance from rGO and MXene, respectively.[133–135] Xu et al. have suggested that in these hybrid films, rGO flakes form a porous structure and connect MXene flakes, improving electrolyte access and electronic conductivity, yielding to further utilization of the MXene's intercalation capacitance.[134] Zhao et al. reported that $Ti_3C_2T_z$/rGO hybrid films fabricated by mixing $Ti_3C_2T_z$ and rGO dispersions followed by VAF show improved capacitance and cycle stability as electrode materials for MSCs due to enhanced electronic/ionic transport capabilities.[135] The electrochemical impedance spectroscopy (EIS) studies of the fabricated electrodes showed a nearly vertical line at low frequencies, indicating capacitive behavior and facile ionic diffusion for $Ti_3C_2T_z$/rGO composite.[134,135]

Functionalizing rGO flake with positively charged surface functional groups and self-assembly of MXene/rGO heterostructure is another reported method for the fabrication of hybrid films.[57,136] The positively charged rGO is attracted by the negatively charged MXene flakes (zeta potential of ~ -39.5 mV for $Ti_3C_2T_z$), resulting in the electrostatic self-assembly of the 2D flakes and formation of agglomerates that precipitate. Electrostatic attraction of flakes, as opposed to their van Der

Waals attraction in physical mixing, provides more intimate contacts between rGO and MXene flakes and effectively reduces their restacking. In other studies, dispersions of rGO functionalized by poly(diallyldimethylammonium chloride) (PDDA, the zeta potential of ~+63.0 mV) and amine groups (NH_2, the zeta potential of ~+41.0 mV) were employed to fabricate flexible electrostatically assembled rGO and MXene heterostructures.[57,136] It was shown that the rGO content significantly affects the physical and electrochemical properties of fabricated films. For instance, increasing the rGO content reduces the electrical conductivity of the hybrid films due to the lower conductivity of rGO compared to the pristine $Ti_3C_2T_z$. [57,136,137] As the content of rGO is increased, the size of the semicircles from the EIS tests was also increased, suggesting an increase in the resistance of the electrodes (**Figure 2-3g**). Also, the CV curves indicated that the charge storage mechanism originates from the change of Ti oxidation state and reversible intercalation/deintercalation of protons.[57,136,138] The incorporation of 5 wt% rGO (corresponding to 3–4 layers of $Ti_3C_2T_z$ for each rGO layer) resulted in the fabrication of films with high densities (3.1 g cm^{-3}), increased interlayer spacing (1.51 nm), and excellent electrical conductivity, leading to enhanced electrochemical properties, including high volumetric energy density and rate capability (**Figure 2-3h**).[57,136]

Xie et al. compared the electrochemical performance of self-assembled $Ti_3C_2T_z$/rGO and $Ti_3C_2T_z$/CNT hybrid electrodes as anode material for Na-ion batteries and capacitors.[16] The hybrid electrodes were fabricated by first assembling $Ti_3C_2T_z$ nanoflakes, and CTAB treated rGO or CNT (CTAB-rGO and CTAB-CNT) in aqueous dispersions followed by VAF. The EIS studies showed a higher charge transfer kinetic for $Ti_3C_2T_z$/CTAB-rGO electrodes, as the low-frequency region slope in the Warburg plot was lower compared to $Ti_3C_2T_z$/CTAB-CNT electrode, resulting in worse electrochemical performances.[16] It was argued that the ion accessibility of MXene/CNT

hybrid electrodes is higher than the MXene/rGO electrodes as the CNTs prevent the MXene layers restacking more effectively and creates a more porous structure in the electrode.[16]

Oxidant-free *in situ* polymerization of monomers between MXene layers is another interesting approach to tailor the mechanical, electrical, and electrochemical properties of MXene-based electrodes. Controlled deposition of the polymers at the MXene surface would result in the synthesis of MXene/polymer hybrids dispersed in water or other solvents. These hybrid MXene flakes can be converted to freestanding films using VAF. The *in situ* polymerization of aniline, pyrrole (PPy), and poly(3,4- ethylenedioxythiophene):poly(styrenesulfonic acid) (PEDOT:PSS) on MXene surfaces have been previously reported for the fabrication of layered MXene/polymer hybrids (**Figure 2-4a**).[41,139,140] The formation of conductive polymer chains between the MXene flakes prevents the restacking of MXene flakes and hence provides plenty of diffusion channels for electrolyte ions.

The *in situ* polymerization mechanism is believed to be initiated by the MXene's oxidizing surface functional groups, but more studies are required to understand the polymerization process.[41,139,140] It is clear from the past studies that the properties of these hybrid electrodes are significantly affected by the process conditions such as the amount of monomer available during the polymerization process. At a very high monomer to MXene ratios, the ordered and layered microstructure, and the electrical conductivity of the electrodes are affected by the presence of unreacted monomers (**Figure 2-4b**).[41,139,140] However, when the monomer amount and the polymerization process were controlled, significant improvements in the electrochemical performance of the electrodes were observed. For example, fabricated $Ti_3C_2T_z$/PPy (2:1 mass to volume ratio) hybrid films, which had a layered architecture composed of periodic layers of $Ti_3C_2T_z$ and PPy, showed a specific capacitance of 416 F g^{-1} at 5 mV s^{-1} compared to 238 F g^{-1} for

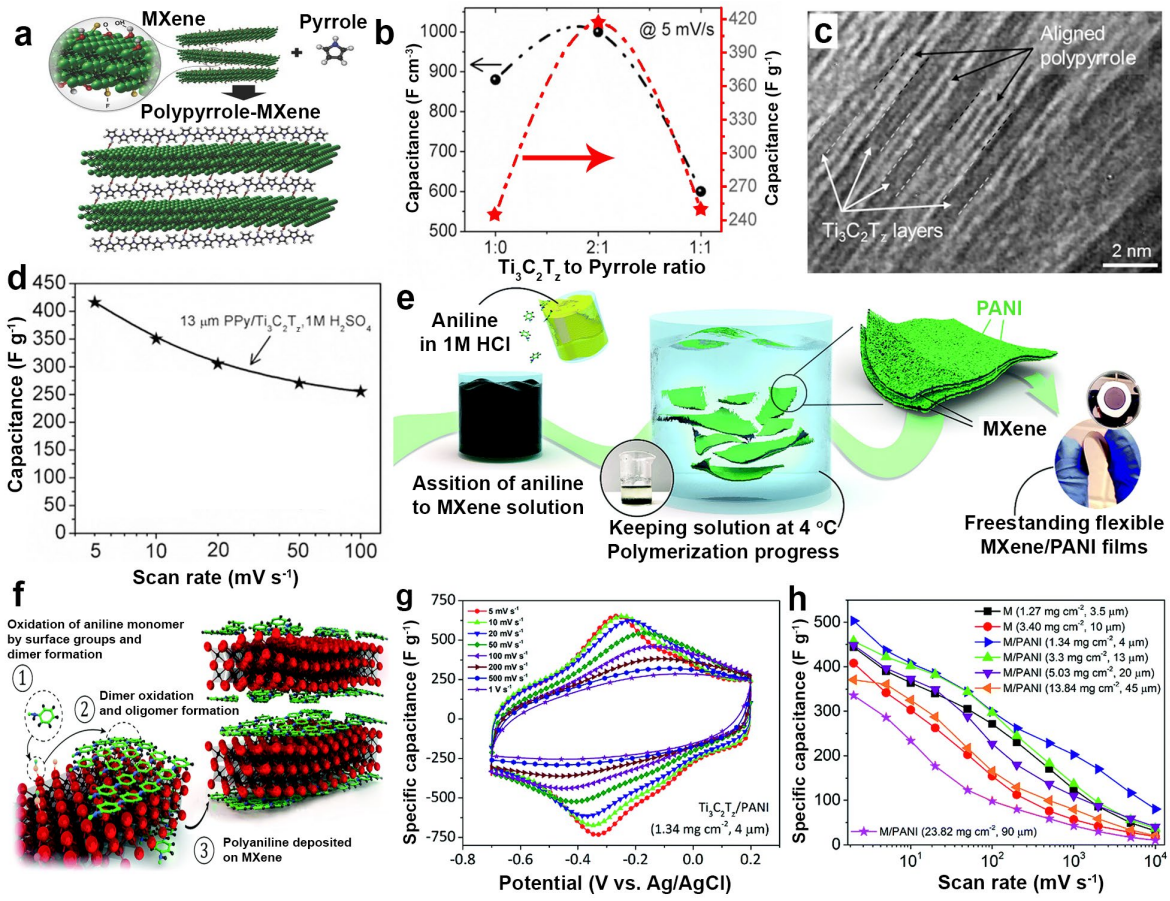

Figure 2.4. *In situ* deposition of polymers on MXene surfaces. (a) Schematic drawing showing the alignment PPy on the MXene surface. (b) Effect of pyrrole content on the volumetric and gravimetric capacitance of PPy/$Ti_3C_2T_z$ hybrid electrodes at 5 mV s^{-1} CV scan rate. (c) A cross-sectional transmission electron microscopy (TEM) image of aligned PPy chains between MXene layers. (d) The rate capability of a 13 μm thick PPy/$Ti_3C_2T_z$ electrode. Reproduced with permission [140] Copyright 2015, Wiley-VCH. (e) Schematic representation of the process used for the synthesis of $Ti_3C_2T_z$ /PANI hybrid film. (f) Schematic drawing suggesting the mechanism of aniline polymerization on MXene surfaces. (g) CV curves of $Ti_3C_2T_z$ /PANI hybrid electrode at different scan rates. (h) Comparison of the rate capability of $Ti_3C_2T_z$ /PANI hybrid electrodes with different mass loadings. *M* represents pristine $Ti_3C_2T_z$ electrodes, and M/PANI indicates hybrid $Ti_3C_2T_z$/PANI electrodes. Reproduced with permission [41] Copyright 2018, Royal Society of Chemistry.

a pristine $Ti_3C_2T_z$ electrode (**Figure 2-4c and d**).[140] As another example, the $Mo_{1.33}CT_z$/PEDOT:PSS (with 10:1 mass ratio) hybrid films treated in an H_2SO_4 solution, showed

enhanced gravimetric and volumetric performances (1310 F cm^{-3} with high conductivity of 29674 S m^{-1}).[139] Similarly, the hybrid films of PANI deposited $Ti_3C_2T_z$ flakes showed excellent pseudocapacitive charge storage for electrodes as thick as ~45 μm (1141 F cm^{-3} at 2 mV s^{-1}, **Figure 2-4 e-h**).[41] A better understanding of the polymerization mechanism is of great importance to expanding the application of this approach to other MXene-polymer hybrid electrodes. [41,139,140]

VAF processes have also been used in the fabrication of hierarchical MXene-based structures with the incorporation of nanosized TMOs and transition metal dichalcogenides (TMDs). This method has been reported to be an effective strategy to enhance the structure (prevent aggregation and restacking) of the electrodes and enhance their electrochemical performances.[141,142] In the structure of these electrodes, MXene flakes offer a highly conductive interconnected network supporting the nanoparticles and also control the volume change of the nanoparticles, while the nanoparticles create diffusion channels between MXene layers.[142] Thus, these hierarchical structures have the potential to deliver high capacities, long cycle lives, and good rate capabilities. For example, self-assembled $Ti_3C_2T_z/SnS_2$ hybrid electrodes were synthesized by adding SnS_2 solution to a colloidal dispersion of $Ti_3C_2T_z$ (at various weight ratio) followed by VAF to fabricated electrodes.[141] When the layered heterostructure of $Ti_3C_2T_z/SnS_2$ (1:5 mass ratio) was tested as anode for Na-ion battery, it demonstrates facilitated kinetics and lower charge transfer resistance resulting in the improvement of specific capacity, rate capability, and cycling stability (322 mAh g^{-1} after 200 cycles at 100 mA g^{-1}).[141]

Using pseudocapacitive 2D TMOs flakes as a supercapacitor electrode is often limited by the low electrical conductivity of the oxides. However, heterostructures and hybrids of 2D TMOs and highly conductive MXenes have shown excellent electrochemical performances.[65] Liu et al. employed a simple method based on mixing and ultrasonication of dispersion of 2D MnO_2 and

$Ti_3C_2T_z$ in water to fabricate flexible freestanding films with the facial alignment of 2D flakes.[65] The capacitive performance and rate behavior of the hybrid film showed significant improvement compared to electrodes fabricated without the addition of MXene flakes **(Figure 2-5 a and b)**. It is suggested that improved electrical conductivity of the electrode by $Ti_3C_2T_z$ flakes, as well as reduced restacking of MnO_2 flakes, which results in the exposure of more active sites at the surface of MnO_2 flakes, are the main causes on the improved performance. In addition, the ordered architecture of the electrodes fabricated with this method resulted in the flexibility and mechanical integrity of the electrodes.[65]

It is worth mentioning that self-assembly processes can be combined with other electrode fabrication methods such as casting rather than VAF to fabricate electrodes. A general strategy for the assembly of TMOs (i.e., TiO_2, SnO_2) on MXene flakes through van der Waals interactions was proposed by Liu and coworkers.[142] The assembly method is based on the difference in the surface energy of MXenes and TMOs in tetrahydrofuran (THF) solutions. MXene flakes tend to form agglomerates in THF solutions due to their high surface energy. However, TMOs show low surface energy when dispersed in THF due to the presence of an organic layer (oleylamine/oleic acid) on their surfaces. Upon mixing the two dispersions, the TMOs are assembled on surfaces of MXene flakes to reduce the free energy of the system (surface energy) through van der Waals forces forming micelle-like heterostructures.[142] Liu et al. reported a uniform distribution of SnO_2 nanowires and TiO_2 nanorods on $Ti_3C_2T_z$ flakes using this assembly method.[142] The fabricated MXene/TMO hybrids were homogeneously mixed with a conductive additive and a polymer binder, and the mixture was casted on the copper foil as the current collector. The electrode materials showed enhanced charge storage properties as the two components (MXene and TMOs)

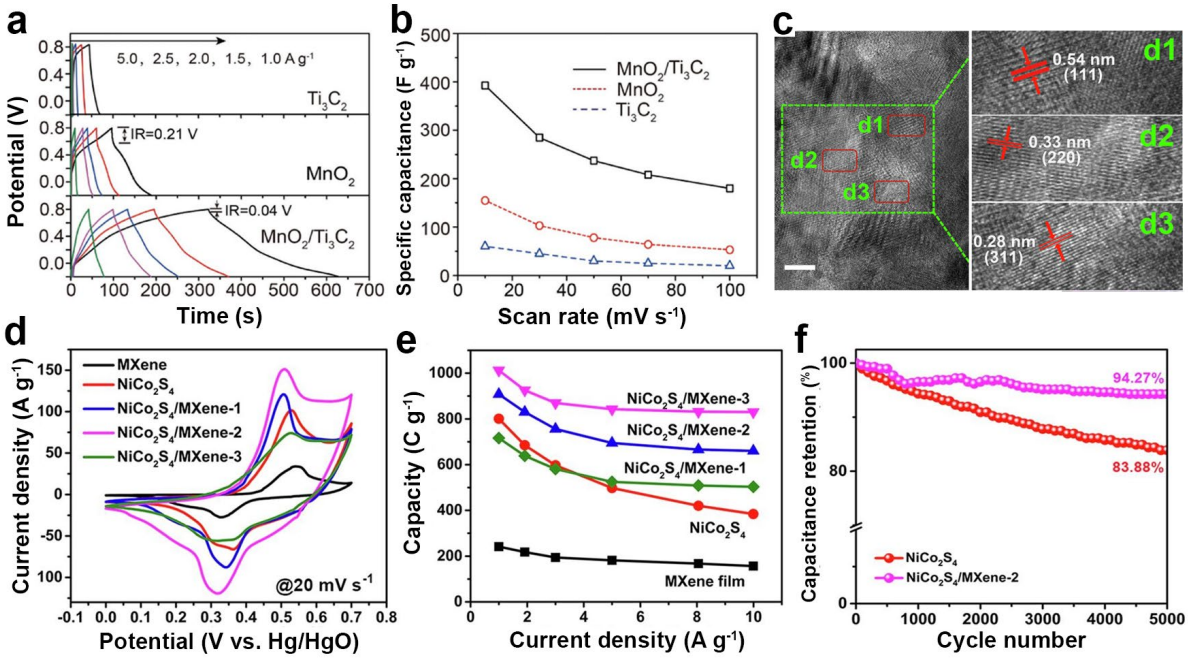

Figure 2.5. (a) Charge–discharge curves of a $MnO_2/Ti_3C_2T_z$ hybrid electrode at various current densities compared with curves of MnO_2 and $Ti_3C_2T_z$ electrodes, showing the significantly prolonged period of discharge for the hybrid electrode. (b) Rate capability of the hybrid $MnO_2/Ti_3C_2T_z$ electrode compared with neat MnO_2 and $Ti_3C_2T_z$ electrodes. Reproduced with permission [65] Copyright 2017, Wiley-VCH. (c) High-resolution TEM (HRTEM) images of the $NiCo_2S_4$/MXene composite electrodes. (d) CV curves of $NiCo_2S_4$/MXene electrodes at a scan rate of 20 mV s^{-1} in 3M KOH electrolyte. (e) The rate capability of $NiCo_2S_4$, $Ti_3C_2T_z$, and their hybrid electrode. (f) Cycling stability of $NiCo_2S_4$ and $NiCo_2S_4$/MXene hybrid electrodes at 5 A g^{-1}. Reproduced with permission [63] Copyright 2019, Elsevier Ltd.

prevented the aggregation of each other.[142] When tested against Li metal, the synergistic effects of MXenes and TMOs in the hybrid electrodes resulted in higher capacity and better rate performance (530 mAh g^{-1} after 500 cycles at 1 A g^{-1} for MXene/SnO_2 heterostructure) of the electrode compared to either pure MXene or TMO electrodes.[142]

In another study, $Ti_3C_2T_z$ dispersions were mixed with a dispersion of positively charged CTAB modified $NiCo_2S_4$ (CTAB-$NiCo_2S_4$) to synthesize electrostatically self-assembled hybrid electrodes. The synthesized materials were homogeneously mixed with a conductive additive and

a polymer binder and pressed onto Ni foam substrates to prepare electrodes and showed a good electrochemical performance in an aqueous electrolyte. For example, an electrode with a 10:1 mass ratio of CTAB-$NiCo_2S_4$ to $Ti_3C_2T_z$ showed a specific capacity of 1028 C g^{-1} at 1 A g^{-1} and a 94.27% capacity retention after 5000 charge/discharge cycles at 5 A g^{-1}, (**Figure 2-5 c-f**).[63] Fu et al. showed that the mass ratio of CTAB-$NiCo_2S_4$ to $Ti_3C_2T_z$ plays an important role in the fabricated structure morphology, as the low amount of $Ti_3C_2T_z$ adversely affect the electrical conductivity and its excessive amounts would hinder the ionic accessibility, both reducing the electrochemical performance. Moreover, the authors argued that the driving forces for the assembly is determined by the CTAB-$NiCo_2S_4$ to $Ti_3C_2T_z$ ratio. At low MXene ratios ($NiCo_2S_4$: MXene ratio of 15:1), electrostatic interactions were dominant, while at higher MXene ratio ($NiCo_2S_4$: MXene ratio of 10:1) hydrogen bonding and van der Waals forces would be the dominant driving forces. $Ti_3C_2T_z$ flakes provide high conductivity, flexibility, and open surfaces for the electrode material and facilitated the ionic diffusion. At the same time, expansion/contraction $NiCo_2S_4$ was confined in the electrode structures, reducing pulverization during repeated charge and discharge of the electrodes.[63]

The assembly of MXene electrodes using VAF is a simple approach enabled by the hydrophilicity of the MXene surface and their dispersibility in water. This process can be readily used for the fabrication of pure MXene electrodes or its hybrids with other nanomaterials with applications in energy storage systems **(Table 2-1)**. Very effective strategies have been developed to control the microstructure of the electrodes, particularly as it pertains to preventing the restacking of the MXene flakes and increasing their interlayer spacing. However, VAF is a very limited process in terms of precise engineering of the microstructure of the electrode. Also, VAF is primarily a batch fabrication process and is not suitable for scale-up. Therefore, as discussed

below, more advanced electrode fabrication processes that enable more control over the microstructure and process parameters have been recently employed in the fabrication of high performance MXene electrodes.

Table 2-1. Electrochemical performance of MXene-based electrodes fabricated through assembling MXene flakes.

Material	Fabrication method	Electrolyte	Test condition	Performance	Energy density	Power density	Ref.
$Ti_3C_2T_z$	Template, VAF	3 M H_2SO_4	10 mV s^{-1} 40 V s^{-1}	310 F g^{-1} 100 F g^{-1}	NA	NA	12
$Ti_3C_2T_z$	Template, VAF	1 M $NaClO_4$ EC:PC:FEC	50 mA g^{-1}	340 mAh g^{-1}	NA	NA	107
$Ti_3C_2T_z$	Template, VAF	1 M $LiPF_6$ in EC:DEC	50 mA g^{-1}	455.5 mAh g^{-1}	NA	NA	123
Mo_2CT_z	Template, VAF	3 M H_2SO_4	10 V s^{-1}	100 F g^{-1}	NA	NA	12
V_2CT_z	Template, VAF	1 M $NaClO_4$ in EC:PC:FEC	50 mA g^{-1}	330 mAh g^{-1}	NA	NA	107
Mo_2CT_z	Template, VAF	1M $NaClO_4$ EC:PC:FEC	50 mA g^{-1}	380 mAh g^{-1}	NA	NA	107
$Ti_3C_2T_z$/CNT	VAF	1 M $LiPF_6$ in EC:DEC:DMC	50 mA g^{-1}	489 mAh g^{-1}	67 Wh kg^{-1}	258 W kg^{-1}	124
$Ti_3C_2T_z$/CNT	Self-assembly, VAF	1 M $NaClO_4$ EC:PC:FEC	20 mA g^{-1}	421 mAh cm^{-3}	NA	NA	16
Mo_2CT_z/CNT	Self-assembly, VAF	1M $NaClO_4$ EC:PC:FEC	50 mA g^{-1}	164 mAh g^{-1}	NA	NA	16
Nb_2CT_z/CNT	VAF	1 M $LiPF_6$ in EC:DEC	50 mA g^{-1}	270 mAh g^{-1}	49 Wh kg^{-1}	546 W kg^{-1}	56
$Ti_3C_2T_z$/ SWCNT	Self-assembly, VAF	1 M KOH	2 mV s^{-1}	220 mF cm^{-2} 314 F cm^{-3}	NA	NA	59
$Ti_3C_2T_z$/ Graphene	VAF	PVA/H_3PO_4	2 mV s^{-1}	3.26 mF cm^{-2} 33 F cm^{-3}	3.4 mWh cm^{-3}	200 mW cm^{-3}	132
$Ti_3C_2T_z$/rGO	VAF, cast	2 M KOH	2 A g^{-1}	154.3 F g^{-1}	NA	NA	135

$Ti_3C_2T_z$/rGO	Self-assembly, VAF	1 M H_2SO_4	2 mV s^{-1}	254 F g^{-1}	NA	NA	57
$Ti_3C_2T_z$/rGO	Self-assembly, VAF	3 M H_2SO_4	2 mV s^{-1}	335.4 F g^{-1} 1040 Fcm^{-3}	32.6 Wh L^{-1}	74.4 kW L^{-1}	136
$Mo_{1.33}C$/ PEDOT:PSS	VAF	PVA/H_2SO_4	0.5 A cm^{-3}	568 F cm^{-3}	24.72 mWh cm^{-3}	19.4 W cm^{-3}	139
$Ti_3C_2T_z$/BC	VAF	PVA/H_2SO_4	0.5 mA cm^{-2}	112.2 mF cm^{-2}	5.5 μW cm^{-2}	NA	125
$Ti_3C_2T_z$/PANI	VAF	3 M H_2SO_4	2mV s^{-1}	503 F g^{-1} 1682 F cm^{-3}	79.8 Wh L^{-1}	575 W L^{-1}	41
$Ti_3C_2T_z$/PPy	VAF	1 M H_2SO_4	5 mV s^{-1}	416 F g^{-1}	NA	NA	140
$Ti_3C_2T_z$/MnO_2	VAF	1 M H_2SO_4	10 mV s^{-1}	390 F g^{-1}	8.3 Wh kg^{-1}	21.33 W kg^{-1}	65
$Ti_3C_2T_z$/SnS_2	VAF	1 M $NaClO_4$ EC:PC:FEC	50 mA g^{-1}	901 mAh g^{-1}	NA	NA	141
$Ti_3C_2T_z$/TiO_2	Self-assembly, cast	1 M $LiPF_6$ in EC:DEC	50 mA g^{-1}	303 mAh g^{-1}	NA	NA	142
$Ti_3C_2T_z$/SnO_2	Self-assembly, cast	1 M $LiPF_6$ in EC:DEC	100 mA g^{-1}	720 mAh g^{-1}	NA	NA	142
$Ti_3C_2T_z$/ $NiCo_2S_4$	Self-assembly, Pressed	3 M KOH	1 A g^{-1}	1028 C g^{-1}	68.7 Wh kg^{-1}	0.85 kW kg^{-1}	63

*ethylene carbonate (EC), diethyl carbonate (DEC), propylene carbonate (PC), fluoroethylene carbonate (FEC)

2.5 Cation-induced self-assembly of MXene flakes

The impact of intercalated ions on the electrochemical properties of MXenes has been the subject of much research since the discovery of these materials. Several studies have confirmed that the insertion of cations between MXene flakes can significantly improve the electrochemical properties of the electrodes through various mechanisms, such as increasing the interlayer spacing and modification of the surface termination groups.[143,144] For example, it is shown that treating multilayered $Ti_3C_2T_z$ (ML-$Ti_3C_2T_z$) in alkali solutions increases the c-lattice parameter (confirmed

with X-ray diffractometry and transmission electron microscopy), due to the intercalation of the cations between the MXene flakes.[94,145] The effects of such treatments on surface chemistry have been studied by X-ray photoelectron spectroscopy (XPS) and Fourier-transform infrared spectroscopy (FTIR). Lian et al. reported that the ML-$Ti_3C_2T_z$ treated in a KOH solution has more -O and -OH surface groups than -F.[94] In addition, *Ab initio* studies of intercalation of alkali metal ions (Na^+, K^+, and Ca^{2+}) in various MXenes (Ti_2CO_2, V_2CO_2, and $Sc_2C(OH)_2$) and their van der Waals heterostructures with graphene suggested that the intercalated layered materials are stable without phase separation or formation of bulk alkali metals.[109]

Due to the negative surface charge of the MXene flakes in aqueous dispersions, their electrostatic interactions with organic and inorganic cations can results in the assembly of flakes into intercalated layered structures with favorable electrochemical properties. Zhao et al. reported the formation of porous 3D networks of crumpled $Ti_3C_2T_z$ induced by alkali ions.[146] They showed that after mixing a dispersion of $Ti_3C_2T_z$ flakes with solutions containing Li^+, Na^+, and K^+ cations, MXene flakes crumple, flocculate, and form a porous 3D architecture.[146] The assembled MXenes showed a *d*-spacing in the range of 15.3 Å and 16 Å, which, in line with previous studies, was more or less independent of the nature of the hydrated intercalating cation.[146,147] The authors argued that this *d*-spacing corresponds to about two water layers between the MXene layers. Electrodes fabricated using the assembled MXene showed excellent capacitive charge storage and rate performance behavior when tested as in Na-ion cells.[146] The trapped water molecules and pre-intercalated cations between MXene flakes caused a pillaring effect and suppressed the volume change due to the intercalation/deintercalation of Na ions.[146,148,149]

In another study, the fabrication of highly stable and flexible freestanding films of V_2CT_z and Ti_2CT_z by a cation-induced assembly process was reported **(Figure 2-6a).**[150] Single-layer flakes

of MXenes such as V_2CT_z and Ti_2CT_z tend to rapidly oxides when dispersed in water, and their films fabricated by VAF can quickly disintegrate in the air **(Figure 2-6 b).** Thus, the electrochemical performance of electrodes fabricated using single-layer flakes of these MXenes had barely been studied before.[150] VahidMohammadi et al. used the cation-induced assembly processed to assemble pre-intercalated layered V_2CT_z and Ti_2CT_z flakes. Freestanding films fabricated using the assembled MXenes showed ordered microstructures while being highly stable in the ambient atmosphere and during electrochemical tests in aqueous electrolytes **(Figure 2-6c).**[150] The suppression of the oxidation of MXene flakes is contributed to the charge transfer between MXene flakes and the intercalated cations, which keeps the surface V atoms in a more reduced state.[150] The films fabricated using the assembled flakes showed not only improved mechanical properties and stability compared to pure MXene films but also demonstrated enhanced electrochemical performances. For example, electrodes fabricated using assembled V_2CT_z showed a high capacitance (~420 F g^{-1} and ~1315 F cm^{-3} for Na-V_2CT_z electrode in a 3M H_2SO_4 electrolyte at 5 mVs^{-1}), rate capability, cycle ability (77% capacity retention over one million cycle for Na-V_2CT_z electrode in a 0.5M K_2SO_4 electrolyte) and therefore, high power and energy densities in different electrolytes **(Figure 2-6 d and e).**[150]

Cation-induced assembly has also been used in the assembly of MXene flakes with other 2D materials. Heterostructures of $Ti_3C_2T_z$ and holey graphene (h-graphene) were synthesized by adding NaOH to a mixture dispersion of $Ti_3C_2T_z$ and H-graphene followed by flocculation of 2D flakes.[62] The porous structure of the MXene/H-graphene hybrid films facilitated ions transportation and prevented restacking of the flakes, resulting in a high specific capacitance (1445 F cm^{-3}), and a good rate capability of the electrodes (69% at 500 mV s^{-1}). In this assembly process, the Ti-F bonds which are unstable in the alkali environment are largely replaced by -OH

termination groups. [62,151] It was reported that further improvement of the electrochemical performance could be achieved by removing the -OH groups by an annealing process (1h at 200 °C under Argon atmosphere) to increase the Ti atoms ratio and reaction sites for the pseudocapacitive reaction.[62,66]

Ma et al. reported the fabrication of porous films of MXene-graphene oxide (GO) using the ion-induced assembly of the $Ti_3C_2T_z$ and GO flakes for the fabrication of freestanding films.[66] They demonstrated that the addition of a solution containing NH_4^+ ions (solution of ammonium bicarbonate, NH_4HCO_3, in water) to a mixture dispersion of negatively charged $Ti_3C_2T_z$ and GO flakes broke the electrostatic balance between MXene and GO flakes, resulting in their flocculation and formation of hybrid microclusters.[66] The morphological studies suggested that increasing the GO content would increase the porosity of the fabricated films while reducing their electrical conductivity. The assembled films were annealed to reduce GO, and the resulting MXene/rGO films exhibited a remarkable cycle performance and high rate capability (98.9 mAh g^{-1} at 4 A g^{-1}) as the anode material for Li-ion batteries.[66] This electrochemical behavior can be attributed to the synergistic effect of MXene and rGO in maximizing the ionic and electronic transport properties of the electrodes.[66]

The 3D networks of crumpled MXene produced by cation-induced assembly can provide a porous and conductive substrate for the deposition of other electrochemically active nanomaterials. For example, Zhao et al. reported a hydrothermal process for uniform deposition of NiCoP nanoparticles on a 3D $Ti_3C_2T_z$ architecture synthesized by the addition of a NaOH solution to a $Ti_3C_2T_z$ dispersion in water.[145] The synthesized hybrid material was characterized as anode materials for Na-ion batteries.[145] The crumpled $Ti_3C_2T_z$ flakes provided a conductive porous

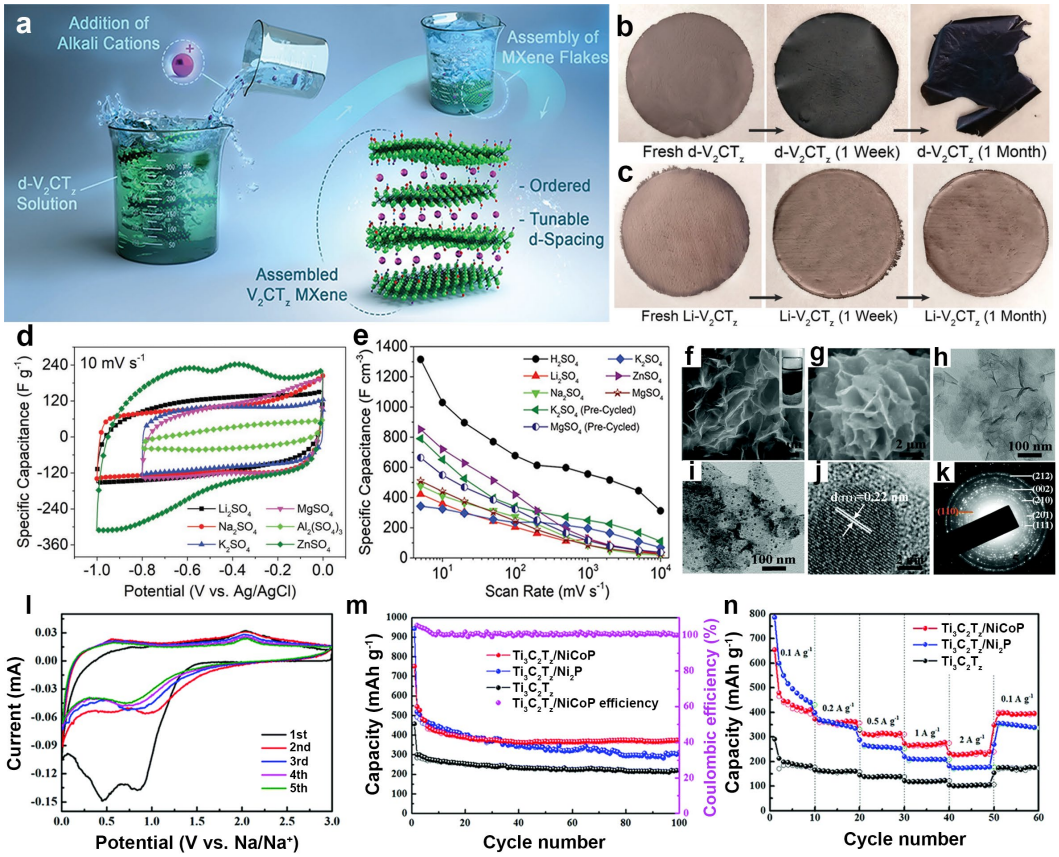

Figure 2.6. (a) Schematic illustration of the assembly of the ordered and highly stable V_2CT_z flakes by a cation-driven assembly process. (b) Digital photographs showing oxidation and color change in d-V_2CT_z films stored in ambient conditions over time (change in color from a grayish brown to black). (c) Digital photographs of a V_2CT_z film assembled using Li salt over time with no visual sign of degradation after a week or a month in ambient conditions. (d) CV curves of Na-V_2CT_z in various electrolytes at 10 mV s^{-1}. (e) Rate performance of a 3–4 μm thick Na-V_2CT_z electrodes in various sulfate-based electrolytes. Reproduced with permission [150] Copyright 2018, Wiley-VCH. (f-g) SEM images of the reassembled $Ti_3C_2T_z$ network and $Ti_3C_2T_z$/NiCoP hybrid. (h-i) Low-magnification TEM images of MXene flakes, the reassembled $Ti_3C_2T_z$ and the $Ti_3C_2T_z$/NiCoP hybrid. (j) HRTEM lattice image of NiCoP shows a d-spacing of 0.22 nm corresponding to the (111) planes of NiCoP. (k) Electron diffraction pattern of the MXene/NiCoP hybrid. (l) CV curves of the $Ti_3C_2T_z$/NiCoP hybrid electrodes at 0.1 mV s^{-1}. (m) The cycling performances of $Ti_3C_2T_z$, $Ti_3C_2T_z$/Ni_2P, and $Ti_3C_2T_z$/NiCoP electrodes at 100 mA g^{-1}. The right axis of the graph shows the coulombic efficiency of the electrodes over cycling. (n) The rate capability of the $Ti_3C_2T_z$, $Ti_3C_2T_z$/Ni_2P, and $Ti_3C_2T_z$/NiCoP electrodes at various current densities (from 0.1 to 2 A g^{-1}). Reproduced with permission [145] Copyright 2019, Royal Society of Chemistry.

network for Na^+ ion diffusion while inhibiting the pulverization and aggregation of NiCoP nanoparticles during Na^+ intercalation/deintercalation processes **(Figure 2-6**Error! Reference source not found. **f-k)**. Also, homogeneously distributed NiCoP nanoparticles would prevent the MXene restacking and provide an interconnected porous network, synergistically improving the electrochemical reaction kinetic, and a higher electrical conductivity, resulting in improved electrochemical performance (262 mAh g^{-1} after 2000 cycle at 1 A g^{-1}, **Figure 2-6 l-n).**[145]

In summary, the improved stability and electrochemical performance of MXene electrodes fabricated by the cation-driven assembly are due to better ion accessibility to the active redox sites at the surface of the individual MXene flakes, modification of surface groups, and an increased interlayer spacing **(Table 2-2)**. The electrodes assembled using this method are capable of intercalation of cations of different sizes and charges. Moreover, employing this method provides the opportunity to study the electrochemical performance of MXenes with low chemical or electrochemical stability.

Table 2-2. Cation-induced self-assembled MXene-based electrodes electrochemical performance.

Material	Fabrication method	Electrolyte	Test Condition	Performance	Rate Capability	Ref.
$Ti_3C_2T_z$/LiOH	Ion-induced assembly, Casted	1 M $NaClO_4$ in EC:DMC:FEC	25 mA g^{-1}	326 mAh g^{-1}	164 mAh g^{-1} at 1 A g^{-1}	146
$Ti_3C_2T_z$/NaOH	Ion-induced assembly, Casted	1 M $NaClO_4$ in EC:DMC:FEC	25 mA g^{-1}	172.5 mAh g^{-1}	61 mAh g^{-1} at 1 A g^{-1}	146
$Ti_3C_2T_z$/KOH	Ion-induced assembly, Casted	1 M $NaClO_4$ in EC:DMC:FEC	25 mA g^{-1}	175 mAh g^{-1}	48 mAh g^{-1} at 1 A g^{-1}	146
V_2CT_z/NaCl	Ion-induced assembly, VAF	3M H_2SO_4	5 mV s^{-1}	420 F g^{-1} 1315 F cm^{-3}	200 F g^{-1} at 100 A g^{-1}	150

V_2CT_z/LiCl	Ion-induced assembly, VAF	1M KOH	2mV s^{-1}	200 F g^{-1}	NA	150
Ti_2CTz/LiCl	Ion-induced assembly, VAF	5 M LiCl	2 mV s^{-1}	172 F g^{-1} 640 F cm^{-3}	NA	150
$Ti_3C_2T_z$/rHGO /NaOH	Ion-induced assembly, VAF	3M H_2SO_4	2 mV s^{-1}	438 F g^{-1} 1445 F cm^{-3}	302 F g^{-1} at 500 mV s^{-1}	62
$Ti_3C_2T_z$/NaOH /NiCoP	Hydrothermal, Cast	1 M $NaClO_4$ in EC:DMC:EMC: FEC	0.1 A g^{-1}	417 mAh g^{-1}	240 mAh g^{-1} at 2 A g^{-1}	145

2.6 Layer-by-layer assembly

Layer-by-layer (LbL) assembly is an effective nanofabrication process to fabricate electrode structures with great ordering and superior functionalities. Oppositely charged nanomaterials or homo- or hetero-phase compounds can be assembled into various structures through electrostatic interactions or hydrogen bonding with high accuracy.[152] Alternate deposition of active materials to form uniform films or 3D networks by electrospinning, electrospraying, and dip-coating are among the most studied LbL assembly methods.[105,152–155] As mentioned above, when dispersed in water, MXene flakes show a negative surface charge. For example, for $Ti_3C_2T_z$, a zeta potential of ~-35mV is reported when the dispersion pH is ~6.5.[31] Therefore, MXene flakes can be utilized in electrostatic LbL fabrication in combination with a positively charged material. LbL assembly has been used for the fabrication of conductive and highly flexible MXene coating and films with good mechanical properties on various substrates (flexible polymer films, glass, silicon wafer, etc.).[156]

In a study by Zhou et al., aqueous dispersions of $Ti_3C_2T_z$ flakes and aminated CNTs with opposite surface charges were used to fabricate highly flexible and foldable electrodes through

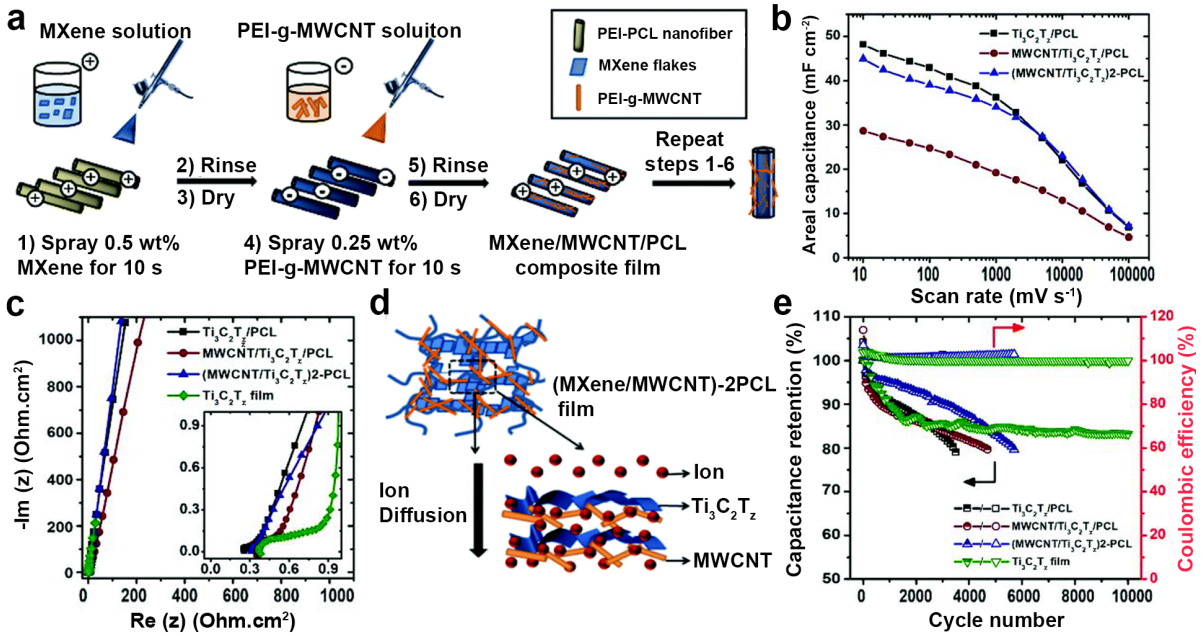

Figure 2.7. (a) Schematic drawing showing the LbL spray coating process used for the fabrication of the MXene/MWCNT electrode with hierarchical structures. (b) The rate capability of the fabricated $Ti_3C_2T_z$/MWCNT electrodes. (c) Nyquist plots of pristine MXene versus MXene/MWCNT composite electrodes. Inset: the high-frequency region of the Nyquist plot. (d) A schematic illustration showing the mechanism for facile ion diffusion in fabricated hierarchical electrodes. (e) Capacitance retention and coulombic efficiency versus cycle number for the pristine and composite electrodes. Reproduced with permission [153] Copyright 2019, Elsevier Ltd.

LbL spray coating on an electrospun polycaprolactone (PCL) fiber substrate **(Figure 2-7a)**.[153] Beside improved mechanical properties, the fabricated electrodes showed enhanced electrochemical performance compared to $Ti_3C_2T_z$ film fabricated using VAF, especially at higher rates **(Figure 2-7b).** EIS of the electrodes showed that both the $Ti_3C_2T_z$ film and $Ti_3C_2T_z$/CNT hybrid electrodes lack the appearance of a semicircle at the high-frequency range of their Nyquist plots, indicating their low charge transfer resistance. However, the EIS spectra of the hybrid electrode was notably different in the mid-frequency region **(Figure 2-7c).** The increased resistance of VAF fabricated $Ti_3C_2T_z$ film in this region (Warburg resistance) implies the limited electrolyte access to the inner regions of the electrode structure.[153,157] The employment of CNTs

as the spacer to prevent restacking and the ordered electrode architecture achieved by the LbL assembly resulted in the improved performance of the electrodes in terms of capacitance, rate capability, and cyclic performance **(Figure 2-7 d and e).**[153]

Zhao et al. fabricated freestanding and flexible heterostructure films of $Ti_3C_2T_z$ and rGO through a spray-assisted LbL assembly of $Ti_3C_2T_z$ and rGO dispersions (**Figure 2-8a**).[137] Adding rGO to MXene decreased the electrical conductivity of the fabricated film's (from 1750 S cm^{-1} for pure $Ti_3C_2T_z$ film to 130 S cm^{-1} for $Ti_3C_2T_z$-20 wt% rGO film) and density (from 3.8 g cm^{-3} for

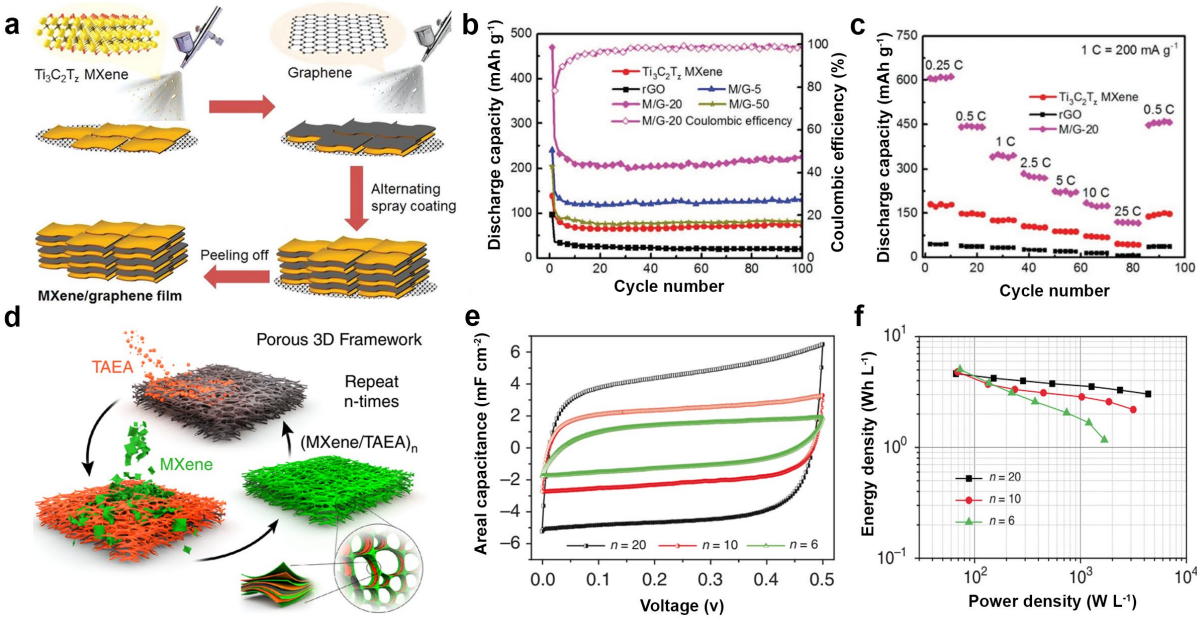

Figure 2.8. (a) Schematic drawing showing the fabrication process of freestanding and flexible 2D MXene/graphene heterostructure films by a spray-assisted LbL process. Electrochemical responses of the $Ti_3C_2T_z$, rGO, and MXene/rGO heterostructure films, (b) comparison of cycling profiles at 2.5 C, and (c) rate profiles. Reproduced with permission [137] Copyright 2019, Wiley-VCH. (d) Schematic illustration of the LbL assembly of $(MXene/TAEA)_n$ multilayer onto porous 3D framework such as a melamine foam. Electrochemical performance of flexible solid-state supercapacitors based on $(MXene/TAEA)_n$ electrodes, (e) CV curves at a scan rate of 2 mV s^{-1}, and (f) Ragone plot of $(MXene/TAEA)_n$ solid-state supercapacitors calculated based on the total volume of the electrode. Reproduced with permission [31] Copyright 2019, Springer Nature.

pure $Ti_3C_2T_z$ film to 1.8 g cm^{-3} for $Ti_3C_2T_z$-50 wt% rGO film). The reported electrical conductivity of films fabricated with spray-assisted LbL was lower than the one fabricated with self-assembly or VAF method, mainly due to a loose stacking of the flakes.[137] When the fabricated electrodes (MXene-20 wt% rGO film) were used as the anode material for Ni-ion batteries, they showed an improved electrochemical performance in terms of capacity (600 mAh g^{-1} at 50 mA g^{-1}), rate capability (220 mAh g^{-1} at 500 mA g^{-1}), and cyclability, compared to pristine $Ti_3C_2T_z$ or rGO films, confirming the importance of structural modifications on the enhancement of electrochemical properties (**Figure 2-8 b and c**).[137]

LbL assembly of MXene with polyelectrolytes such as polyethyleneimine, poly(diallyldimethylammonium chloride), or poly(sodium 4-styrene sulfonate) produce a large interlayer gap between MXene flakes disturbing the electron conduction paths and reducing the conductivity.[105,156,158] The inactive polymer would increase the dead volume/mass of the electrode, and due to their large molecular size, the formation of LbL assembled MXene with high accuracy is not likely.[31,132,156] However, as it was demonstrated by Tian et al. that using small positively charged molecules such as tris(2-aminoethyl) amine (TAEA) for LbL fabrication of $Ti_3C_2T_z$ multilayers and pillared films resulted in a highly ordered and a quasi-intimate face-to-face contact between the MXene flakes (**Figure 2-8 d-f**).[31] When tested as electrodes in a solid-state supercapacitor, the fabricated electrodes showed high mechanical performances in combination with high energy and power densities of 3.0 WhL^{-1} and 4400 W L^{-1}, respectively. Tian et al. argued that the TAEA pillars in the architecture provide more active surface area and facilitate the protons to reach the deep-trap sites of MXene flakes, enhancing the redox reactions. Besides, a small increase in the gap distance did not affect electrical conductivity, ensuring fast charge transport at high rates.[31]

In another study in this direction, Zhao et al. reported the effects of fabrication methods and resulting structures on the electrochemical performance of porous MXene/TMO (Co_3O_4 and $NiCo_2O_4$). The heterostructures were fabricated via LbL spray coating, alternate filtration, and *in situ* growth of oxides.[122] In the LbL process, MXene and TMO suspensions were alternately sprayed onto a polypropylene substrate for the fabrication of freestanding flexible hybrid films (**Figure 2-9 a and b**). The fabricated structures offered plenty of active redox sites, enlarged surface area, effective electron transport network, and improved wettability.[122] The $Ti_3C_2T_z/Co_3O_4$ heterostructure showed improved capacity and rate performance behavior when tested as the anode materials for Li-ion batteries. This was attributed to the oxide's contribution to the total capacity of the electrode (**Figure 2-9 c**). Electrodes fabricated by LbL spray coating of $Ti_3C_2T_z$, and $NiCo_2O_4$ dispersions showed the best electrochemical performance among the studied electrodes (specific capacities of 1330, 650, and 330 mAh g^{-1} at 32, 1600 and 3200 mA g^{-1}, respectively) due to the $NiCo_2O_4$ intrinsic properties and the favorable electrode architecture provided by LbL spray coating compared with alternate filtration or *in situ* growth process (**Figure 2-9 d-f**).[122]

To fully utilize the MXene electrochemical properties, uniform distribution of $Ti_3C_2T_z$ flakes on a porous conductive substrate, such as Ni foam, was proposed by Tian et al.[105] The suggested method significantly prevents the restacking, while increasing the effective contact area. These electrodes showed quasi-core-shell structures and were fabricated through alternative immersion of the substrate in positively charged polyethyleneimine solution and negatively charged $Ti_3C_2T_z$ dispersion offering precise control over the active material loading on the substrate. The $Ti_3C_2T_z$ quasi-core-shell electrodes showed a superior performance (370 F g^{-1} at 2 mV s^{-1} and 117 F g^{-1} at 1000 mV s^{-1}) when compared with pristine $Ti_3C_2T_z$ films (33 F g^{-1} at 1000 mV s^{-1}) when tested as

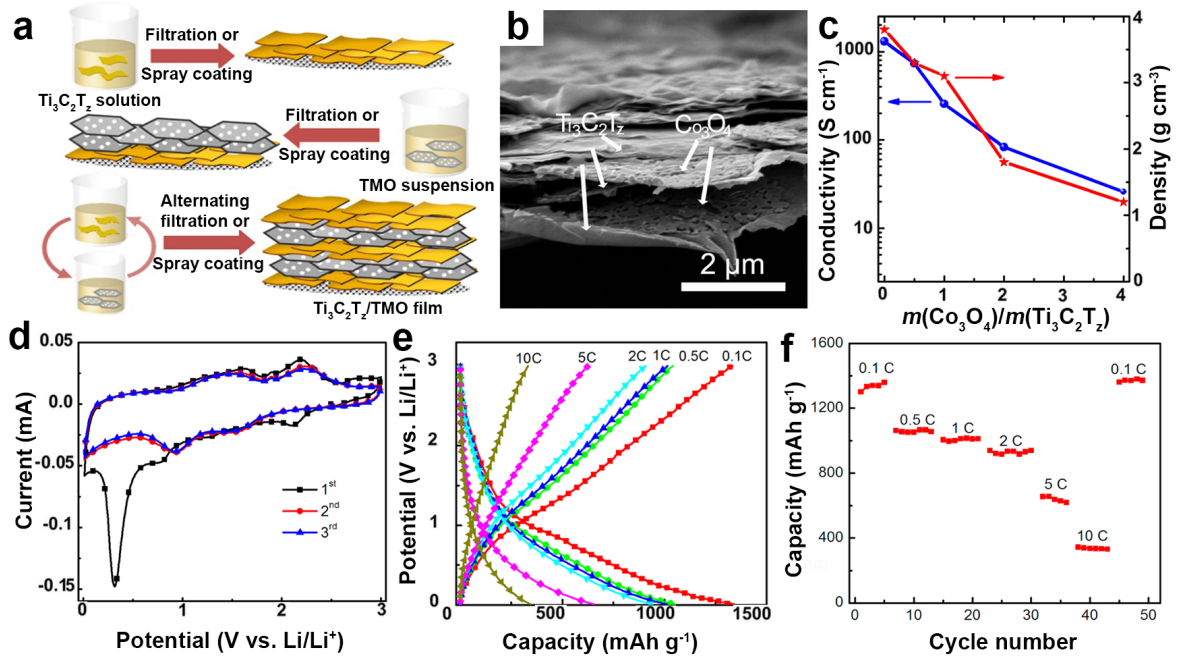

Figure 2.9.(a) Schematic illustrating of alternate filtration and spray coating as the synthesis processes for the fabrication of freestanding MXene/TMO hybrid films. (b) A cross-sectional SEM image of MXene/Co_3O_4 hybrid film. (c) Electrical conductivity and film density as a function of $Ti_3C_2T_z/Co_3O_4$ mass ratio (d) CV curves of spray coated $Ti_3C_2T_z/NiCo_2O_4$ film at 0.1 mV s^{-1}. (e, f) Charge-discharge profile of the fabricated $Ti_3C_2T_z/NiCo_2O_4$ film and their rate performance (1 C equals 320 mA g^{-1}) at different current densities, respectively. Reproduced with permission [122] Copyright 2016, Elsevier Ltd.

supercapacitor electrodes in a 1M Li_2SO_4 electrolyte. The higher specific surface area, less restacking, more accessible ionic diffusion channels, and improved electron transport properties provided by Ni foam, resulted in a higher charge storage capacity and rate performance.[105]

The LbL fabrication methods based on dip-coating of the substrates in a dispersion of charged species, although it provides control over the composition, material loading, and the resulting structure, it can be extremely time-consuming (e.g., 80 h for 300 bilayers in ref.[11]); thus its broad application for scalable manufacturing is restricted. To shorten the manufacturing time in the fabrication of LbL electrodes, an automated spin spray layer-by-layer (SSLbL) method (which is

not limited by the polyelectrolyte diffusion) was proposed by Weng et al.[158] They demonstrated that SSLbL offers control over conductivity, transparency, and thickness of the MXene/CNT hybrid films that were subsequently used for electromagnetic interference shielding and energy storage. The lightweight LbL MXene/CNT architecture was fabricated on various substrates, including glass slide, polyester film, and silicon wafer. It delivered high electrical conductivities (up to 130 S cm^{-1}), flexibility, and environmental stability, which are important for electrochemical applications, but the fabricated electrodes were not tested as electrode material for energy storage.[158]

From what has been reported regarding the LbL assembly of MXene-based structures, it can be concluded that the fabricated electrodes show less restacking, enhances ionic transport, and ion adsorption strength in combination with outstanding mechanical properties, which guarantees structural stability during ion intercalation/deintercalation.[15,90,105,118,119,137,153]

Table 2.3. Comparison between the electrochemical performance of MXene-based electrodes fabricated via the LbL assembly process.

Material	Fabrication method	Electrolyte	Test condition	Performance	Rate Capability	Ref.
$Ti_3C_2T_z$/SWCNT	Alternate VAF	1M $MgSO_4$	2 mV s^{-1}	390 F cm^{-3} 150 F g^{-1}	280 F cm^{-3} at 200 mV s^{-1}	129
$Ti_3C_2T_z$/CNT	LbL Spray coating	1M H_2SO_4	10 mV s^{-1}	45 mF cm^{-2}	23 mF cm^{-2} at 10 V s^{-1}	153
$Ti_3C_2T_z$/rGO	Alternate VAF	1M $MgSO_4$	2 mV s^{-1}	435 F cm^{-3}	320 F cm^{-3} at 200 mV s^{-1}	129
$Ti_3C_2T_z$/rGO	LbL Spray coating	1M $NaClO_4$ EC:PC:FEC	50 mA^{-1}	600 mAh g^{-1}	120 mAh g^{-1} at 5 A g-1	137
$Ti_3C_2T_z$/TAEA	Spin-assist/Spray LbL assembly	PVA/H_2SO_4	2 mV s^{-1}	4.8 mF cm^{-2} 583 F cm^{-3}	3.1 mF cm^{-2} at 200 mV s^{-1}	31
$Ti_3C_2T_z$@Ni foam	LbL self-assembly	1M Li_2SO_4	2 mV s^{-1}	370 F g^{-1}	117 F g^{-1} at V s^{-1}	105
$Ti_3C_2T_z$/Co_3O_4	Alternate VAF	1 M $LiPF_6$ in EC:DEC	32 mA g^{-1}	810 mAh g^{-1}	150 mAh g^{-1} at 6.4 A g^{-1}	122
$Ti_3C_2T_z$/$NiCo_2O_4$	LbL spray coating	1 M $LiPF_6$ in EC:DEC	32 mA g^{-1}	1330 mAh g^{-1}	330 mAh g^{-1} at 3.2 A g^{-1}	122

2.7 Fabrication of MXene electrodes by printing processes

Self-powered electronics and micro/nanosystems often require energy storage devices that can be integrated with other electronic components on a variety of substrates in a limited space.[1] This requirement has led to the recent interest in the design and fabrication of 2D or 3D on-chip energy storage devices. For example, the fabrication of MSCs in 3D architectures can significantly improve their energy density in a limited foot-print area due to the higher loading of active material per area. However, the 3D electrode should show the typical properties of high performance supercapacitor electrodes, such as a porous structure, high surface area, and in case of 2D materials, low restacking of the 2D sheets.[159–163]

Printing, as a simple, cost-effective, and scalable fabrication process, has been employed to fabricated MXene-based energy storage devices with high energy densities **(Figure 2-10a).**[121,163] Recent studies have demonstrated electrode and device fabrication using versatile and simple printing processes enabled by the development of water-based inks based on $Ti_3C_2T_z$.[121,164–166] Yu et al. reported the fabrication of 3D electrodes using an ink prepared by mixing crumpled nitrogen-doped $Ti_3C_2T_z$ (N-$Ti_3C_2T_z$) flakes with activated carbon, CNTs, and GO.[167] The crumpled N-$Ti_3C_2T_z$ was synthesized through a sacrificial templating method (using melamine formaldehyde nanospheres as the template).[166,167] Following the printing process, the 3D electrodes were freeze-dried and reduced for 2h at 90 °C. The 3D printed electrodes were fixed on titanium mesh substrate to be tested in a three-electrode test set up. Three-layered electrodes of N-$Ti_3C_2T_z$ composite showed a high areal capacitance with good cycling stability (96.2% capacitance retention after 5,000 cycles) in 3M H_2SO_4 electrolyte.[167] In another study, a similar ink formulation (N-$Ti_3C_2T_z$:CNTs:GO:5:2:3 weight ratio) was used by Fan et al. for printing electrodes for Na-ion

hybrid capacitor.[166] The Na-ion hybrid capacitor showed areal energy and power densities of 1.18 mWh cm^{-2} and 40.15 mW cm^{-2}, respectively.[166]

Due to the advantages of 3D device architecture, among various printing methods, 3D printing processes are most interesting for the fabrication of energy storage devices such as MSCs. Very recently, 3D printing of MXene-based MSCs through the extrusion-based printing process have been reported.[121,163,164,166] In this 3D printing method, an ink that exhibits viscoelastic properties and shear-thinning behavior is extruded out of a nozzle and deposited on a substrate in a layer-by-layer fashion to construct a 3D structure. Therefore, the viscoelastic properties of the ink play a crucial role in this process to allow each deposited layer to retain its shape and tolerate the additional deposited layers while providing enough fluidity for interlayer adhesion.[121,163,168]

Printable inks based on MXene have been used in other printing processes for the fabrication of energy storage devices. Xu et al. used a two-step screen printing process to fabricate asymmetric hybrid devices.[169] To increase the voltage window, the asymmetric device was designed to use $Ti_3C_2T_z$ and Co-Al LDH as the negative and positive electrodes, respectively. The fabricated devices showed an areal specific capacitance of 40.0 mF cm^{-2} at 0.75 mA cm^{-2}, high cycling stability (92% capacitance retention after 10,000 cycles), and an energy density of 10.80 μWh cm^{-2} in alkaline electrolytes.[169] In another study, Li et al. used single-layer $Ti_3C_2T_z$ flakes decorated with hydrous RuO_2 nanoparticles mixed with silver nanowires (AgNWs) to prepare a thixotropic ink for screen printing.[170] The hydrous RuO_2 nanoparticles promoted the pseudocapacitive behavior and functioned as spacers between MXene flakes to facilitate ionic transport. AgNWs were added to achieve favorable rheological properties and increase the ink viscosity while boosting the electrical conductivity of the printed electrodes. The screen-printed MSCs showed a

high rate capability and acceptable cycling stability (90% capacitance retention after 10,000 cycles).

One of the main concerns in the preparation and printing of the water-based MXene inks is the low stability of MXene flakes and their oxidation or hydrolysis in aqueous dispersions, which limits their long-term storage. Wu et al. have studied the stability of the ligand-capped MXene inks prepared by the delamination of multilayered $Ti_3C_2T_z$ in dispersions containing sodium ascorbate, sodium oxalate, sodium citrate, and sodium phosphate.[171] Among the prepared inks, the sodium ascorbate-capped MXene (SA-MXene) showed excellent oxidation stability after 80 days of exposure to air at ambient conditions, while the $Ti_3C_2T_z$ flakes in other prepared dispersion oxidized and turned to anatase.[171] It was suggested that the oxidation and hydrolysis of MXene are prevented due to the interaction of undercoordinated Ti atoms on the surface and edges of MXene flakes with the ascorbate through hydrogen and coordinate bonding.[171] To achieve better rheological properties, the SA-MXene dispersion was mixed with a non-ionic surfactant (Triton X) to decrease the surface tension and a co-solvent (propylene glycol) to increase the viscosity. The prepared ink was used for inkjet printing of MSCs, and the fabricated interdigital devices showed an areal capacitance of 108 mF cm^{-2} and volumetric capacitance of 720 F cm^{-3} at a current density of 1A g^{-1} with a relatively high rate capability and cycling stability (94.7% capacitance retention after 4,000 cycles).[171]

In conclusion, MXenes can easily form additive-free stable colloidal dispersions in various aqueous and organic solvents, which makes them particularly valuable in the context of environmental-friendly printing.[2,121,164] Developing stable MXene-based ink without adding any surfactant and rheology modifier provides the opportunity to employ printing methods such as inkjet printing, screen printing, and extrusion-based 3D printing as scalable, simple, and

inexpensive fabrication techniques for devices fabrication **(Table 2-)**. Besides, MXene-based inks can be used for printing complex 3D architecture, and through careful designing of these structures, the performance of MXene-based energy storage devices can be significantly improved.

Table 2-4. Electrochemical performance of MXene-based printed structures.

Material	Printing method	Electrolyte	Test condition	Performance	Energy density	Power density	Ref.
$Ti_3C_2T_z$	Inkjet	PVA/H_2SO_4	4 μA cm^{-2}	12 mF cm^{-2}	NA	NA	165
SA-$Ti_3C_2T_z$	Screen	PVA/H_2SO_4	1 A g^{-1}	108.1 mF cm^{-2} 720.7 F cm^{-3}	0.1 Wh cm^{-3}	1.9 W cm^{-3}	171
N-$Ti_3C_2T_z$	Screen	PVA/H_2SO_4	10 mV s^{-1}	70.1 mF cm^{-2}	NA	NA	167
$Ti_3C_2T_z$/AgNWs/ $RuO_2.xH_2O$	Screen	PVA/KOH	1 mV s^{-1}	864.2 F cm^{-3}	13.5 mWh cm^{-3}	48.5 W cm^{-3}	170
$Ti_3C_2T_z$	Extrusion	PVA/H_2SO_4	2 mV s^{-1}	1035 mF cm^{-2}	51.7 μWh cm^{-2}	5.7 μW cm^{-2}	121
$Ti_3C_2T_z$	Extrusion	PVA/H_2SO_4	5 μA cm^{-2}	43 mF cm^{-2}	0.32 μWh cm^{-2}	11.4 mW cm^{-2}	165
$Ti_3C_2T_z$	Extrusion	PVA/H_2SO_4	1.7 mA cm^{-2} 0.2 A g^{-1}	2.1 Fcm^{-2} 242 F g^{-1}	24.4 μWh cm^{-2}	0.64 mW cm^{-2}	163
N-$Ti_3C_2T_z$/CNT/ GO/AC	Extrusion	3 M H_2SO_4	10 mV s^{-1}	8.2 F cm^{-2}	0.42 mWh cm^{-2}	NA	167
$Ti_3C_2T_z$/SWCNT	Duplex	PVA/H_3PO_4	25 μA cm^{-2}	30.76 mF cm^{-2}	8.37 μWh cm^{-2}	17.31 μW cm^{-2}	172

2.8 Assembling MXene aerogels and hydrogels

Aerogels and hydrogels of 2D materials have been widely considered as electrodes for energy storage devices. For MXenes, significant improvement in the electrochemical properties are reported when the 2D flakes are assembled in aerogel or hydrogel structures. The current interest in this direction originated from a study by Lukatskaya et al., where a record high volumetric capacitance (~1,500 Fcm^{-3}) was reported for $Ti_3C_2T_z$ hydrogel electrodes in H_2SO_4 electrolytes.[12] Due to their open and highly accessible structures, the hydrogel electrodes showed ultra-high rate capability and could deliver acceptable capacitances at high scan rates as high as 10 Vs^{-1}.[12]

Aerogels, fabricated by freeze-drying of MXene dispersions, show highly porous structures in which MXene flakes are crumbled and form a 3D conductive network. MXene aerogels show high

mechanical stability, plenty of interconnected micro- and mesopores that provide facile electrolyte diffusion channels, and large active surface areas and, therefore, excellent electrochemical performances.[159,173,174] It is worth mentioning that besides their application in energy storage, these structures have often shown superior properties in other applications such as electromagnetic interface shielding.[159,175–178]

Li et al. reported the fabrication of 3D $Ti_3C_2T_z$ aerogel via a self-assembly method by introducing EDA (ethylenediamine) as a weak reducing agent to MXene colloidal dispersions **(Figure 2-10d).**[173] It was suggested that EDA helps $Ti_3C_2T_z$ flakes to reassemble and form a hydrogel that can be transformed into a lightweight aerogel by freeze-drying. The fabricated aerogel showed a specific surface area of 176.3 m^2 g^{-1}, which is much higher than the previously reported surface areas for MXene powders and films. The aerogel had an excellent mechanical property in combination with enhanced electrochemical performance with a measured areal capacitance of up to 1012.5 mF cm^{-2} at 2 mV s^{-1} in a 1M KOH electrolyte **(Figure 2-10 e and f).**[173]

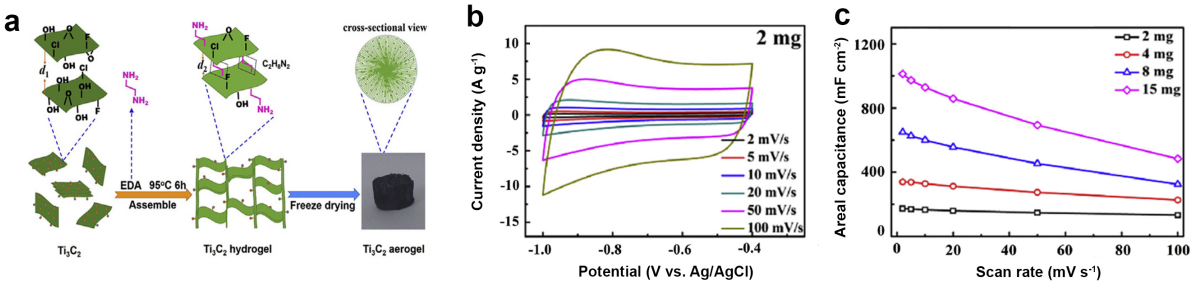

Figure 2.10. (a) Schematic illustration showing the formation mechanism of $Ti_3C_2T_z$ aerogels, and a digital image showing the fabricated 3D $Ti_3C_2T_z$ aerogel. (b) CV curves of the $Ti_3C_2T_z$ aerogel electrode at various scan rates. (c) Areal capacitance as a function of scan rates for electrodes with different mass loadings. Reproduced with permission [173] Copyright 2017, Elsevier Ltd.

Recently, Yue et al. reported the fabrication of 3D self-healable devices based on $Ti_3C_2T_z$/rGO through a process that involves freeze-drying of a mixed dispersion of $Ti_3C_2T_z$ and rGO followed by laser cutting of the electrodes to a predesigned interdigitated pattern. The fabricated devices were wrapped with carboxylated polyurethane (PU) shells, which were responsible for the healing ability of the device through the interface hydrogen bonds.[159] The encapsulated $Ti_3C_2T_z$/rGO devices showed good capacitive and cycling performance at high current densities. The healing ability of the fabricated device was demonstrated when it was bisected for 5 times and kept 81.7% of its original specific capacitance when it was reconstructed by pressing the bisected pieces together. For all the reported MXene aerogel and hydrogel electrodes, the formation of a porous 3D structure, prevention of flake restacking, increased surface areas, and high electronic and ionic transport properties of the electrodes are cited as the reason for the improved electrochemical performances.[12,159,174]

As described in this review paper, various fabrication methods, each having some advantages and disadvantages, have been used in the fabrication of MXene electrodes for energy storage applications. VAF is straight forward fabrication method and suitable for the fabrication of freestanding films (thicknesses in μm range) while transferring the fabricated films into other substrates is very challenging, and the process is a batch process. LbL assembly is a tunable, and facile fabrication method which can be adopted for the fabrication of films (thicknesses in nm to μm range) on various substrates with control over structure and loading of the active material per area of the electrode. However, LbL is a time-consuming multistep process and often requires multiple washing steps and using polyelectrolytes, which can affect the properties of the fabricated structure. Printing processes such as extrusion printing, screen printing, and inkjet printing are flexible processes that provide control over the design and thickness (thicknesses in nm to μm

range) of the pattern and have advantageous in terms of scalability and resolution. However, printable materials are limited, and complex procedures are required to formulate materials into printable inks.

Chapter 3

Electrochemical Properties of 3D Printed MXene-based Structures

This chapter presents the results of my research on the fabrication of all-solid-state MSCs through a 3D printing of additive-free and water-based MXene ink. The fabricated MSCs benefit from the high electrical conductivity and excellent electrochemical properties of 2D $Ti_3C_2T_x$ MXene and a 3D interdigital electrode architecture to deliver high areal and volumetric energy densities. We demonstrate that a highly concentrated MXene ink shows desirable viscoelastic properties for extrusion printing at room temperature and therefore can be used for scalable fabrication of MSCs with various architectures and electrode thicknesses on a variety of substrates. The goal of this research was to develop a printable and additive-free MXene-based ink as well as studying the electrochemical properties of the MXene-based printed structures. The developed printing process can be readily used for the fabrication of flexible MSCs on polymer and paper substrates. Our study introduces $Ti_3C_2T_x$ MXene as an excellent choice of electrode material for the fabrication of 3D MSCs and demonstrates 3D printing of MXene inks at room temperature.

3.1 Introduction

For efficient integration of storage devices with self-powered systems, direct fabrication of these devices on different substrates is required.[1,179,180] This requirement has stimulated much

research on the design and fabrication of "on-chip" batteries and supercapacitors.[1] In particular, on-chip supercapacitors, often referred to as MSCs, have been introduced as high power devices with relatively high energy densities and suitable for integration with miniaturized electronics. Similar to conventional supercapacitors, the storage properties of MSCs are highly dependent on the intrinsic properties and the charge storage mechanism of their electrode materials.[2,181–186] However, the properties of MSCs are also significantly influenced by the configuration of different components of the device- the so-called device "architecture". For example, it was shown that in-plane fabrication of electrodes in interdigital arrangements with controlled spacing can significantly improve the ion transport between electrodes resulting in ultrahigh power performance of the fabricated MSCs.[187]

The performance metrics for MSCs are usually different than those of conventional supercapacitors.[1,188] For miniaturized MSCs, the gravimetric performance of the electrodes is not an appropriate metric to evaluate their performance as the weight of the electrodes is a small fraction of the total weight of the device.[1,188] However, since MSCs are fabricated in limited footprint areas, maximizing areal and volumetric performances should be the main factors considered in the selection of electrode materials and designing the device architecture.[1,179,187] Therefore, MSCs with 3D architectures have received much attention in the past few years as they allow loading more active materials per unit area of the device to increase areal performance.[179,189] However, scalable fabrication of 3D devices that utilize high-performance electrode materials is still very challenging.[190]

Direct ink writing (DIW) or robocasting is an extrusion-based additive manufacturing method that has been extensively used for the fabrication of complex structures used in various fields, including energy storage.[189,191–196] In this printing method, a colloidal or gel-type ink

(filament) is extruded through a nozzle and deposited on a substrate in a layer-by-layer fashion to fabricate 3D structures. This direct printing method is significantly more efficient and less complex compared to lithography and deposition methods that have been previously used for the fabrication of 3D energy storage devices.[195,196] However, fabrication of 3D MSCs using extrusion-based 3D printing depends on the availability of printable inks that are based on highly conductive and electrochemically active electrode materials. To be printable, the ink should exhibit shear-thinning behavior and viscoelastic properties, which enable each layer to retain its shape while still providing enough fluidity for substrate and interlayer adhesion.[189,197] Although significant progress has been made in the ink writing of electrochemical devices and electrodes based on the materials such as CNTs, graphene, molybdenum disulfide, and a few other materials, most printable inks are prepared by using additives such as secondary solvents or surfactants to adjust their rheological properties.[194,197–199] These additives can affect the electrical and electrochemically properties of the printed electrodes and may require removal after printing.[200]

Herein, we demonstrate low-cost and scalable fabrication of high-performance 3D MSCs based on 2D $Ti_3C_2T_x$, which is a member of the MXene family of materials. MXenes are an emerging class of 2D transition metal carbides and nitrides with a general formula of $M_{n+1}X_nT_X$ (n = 1, 2, or 3), where M denotes a transition metal (Ti, Cr, V, *etc*.), X is carbon and/or nitrogen, and T_X denotes surface functional groups (=O, –OH, and –F) randomly distributed on the surface of the 2D flakes.[2,69,201–203] $Ti_3C_2T_x$ exhibits a combination of high electrical conductivity, outstanding electrochemical properties, and hydrophilicity and therefore, is an attractive material for 3D printing of MSCs.[2] The pseudocapacitive performance of $Ti_3C_2T_x$ was first studied using freestanding and binder-free film electrodes, which demonstrated outstanding volumetric capacitances (300–400 F cm^{-3}), exceeding the performance of EDLCs based on carbon

nanomaterials.[71,202] Later, improved performance of $Ti_3C_2T_x$ electrodes was reported by modification of the synthesis process,[91,202,204] hybridization with other nanomaterials,[41,44,71,129,140,205] and engineering the microstructure of the electrodes.[12,206–208] Recently, specific capacitances as high as ~1500 F cm^{-3} for pure $Ti_3C_2T_x$ and 1682 F cm^{-3} for its hybrid with conductive polymers are reported.[12,41] In the past few years, there have been few reports on the fabrication of MSCs based on MXenes with higher areal and volumetric capacitances and energy densities compared to MSCs based on other electrode materials.[207] Recently, Zhang *et al*. reported the preparation of MXene inks and utilizing inkjet and high-temperature extrusion printing to fabricate MSCs with areal capacitances of as high as 43 mF cm^{-2}.[165] However, to the best of our knowledge, the preparation, and printing of MXene inks with ultrahigh concentrations and fabrication of MXene MSCs through room temperature DIW have not been previously reported.

In this research, the fabrication of 3D MSCs using a viscoelastic, highly concentrated, water-based, and additive-free MXene ink is demonstrated. The prepared ink can be directly used for extrusion printing at room temperature and fabricating MXene devices with interdigital electrode configurations on a variety of substrates, including flexible polymer films and papers. The height of the electrodes and the loading of active materials per unit area are controlled by the number of deposited layers. The 3D printed all-solid-state MSCs showed excellent electrochemical performance with exceptional areal capacitances and energy densities. Our results reveal the high potential of MXene inks for scalable 3D printing of future electronic and electrochemical devices.

3.2 Materials and Methods

3.2.1 MAX Phases Synthesis

The synthesis of Ti_3AlC_2 MAX phase was performed in 2 steps according to a previously reported method.[209] Frist, Ti_2AlC MAX phase was synthesized by mixing TiC powder (99.5% Alfa Aesar), Ti powder (99.5%, Alfa Aesar), and Al powder (99.5%, 325 mesh, Alfa Aesar) in a 1:1:1 molar ratio. The mixture was ball milled for 24 hours, then sintered at 1400 °C for 2 h under flowing Argon with a 5 °C/min heating rate. The resulting material was milled into a fine powder, sieved, and Ti_2AlC powder with a particle size of less than 38 μm was used in the next step. For the synthesis of Ti_3AlC_2, the resulting Ti_2AlC powder was mixed with TiC powder (99.5% Alfa Aesar) in a 1:1 molar ratio, ball milled for 24 h and then sintered at 1400 °C for 2 h under flowing Argon with a 10 °C/min heating rate. The resulting sintered material was milled, sieved, and particles of less than 38 μm were used for MXene ink preparation.

3.2.2 MXene Synthesis

The $Ti_3C_2T_x$ suspension was prepared based on a previously reported method.[71] Briefly, concentrated hydrochloric acid (HCl, ACS Grade, BDH) solution was diluted with DI water to obtain 40 mL of 6 M HCl solution. 2g lithium fluoride (LiF, 98+% purity, Alfa Aesar) was added to the solution and stirred for 10 minutes using a Teflon coated magnetic stir bar at room temperature. The solution was then moved to an ice bath, and 2g of Ti_3AlC_2 powder was slowly added to the solution (to prevent overheating). The resulting mixture was transferred to a hot bath (35 °C) and kept for 24 hours (stirring at 550 rpm). The mixture was then washed several times with DI water and centrifuged at 3500 rpm until the supernatant pH was ~6. The MXene powder was then collected (filtered using a Celgard® porous membrane), redispersed in DI water, and

sonicated for 30 min. The resulting suspension was centrifuged at 3500 rpm for 1 hour, and the supernatant was collected and used as the initial solution.

3.2.3 Ink Preparation

The printable MXene ink was produced without any additives or high-temperature drying, which can affect the properties of $Ti_3C_2T_x$. The MXene solution was directly used in this step. Super absorbing polymers (SAP) beads were used to absorb water from the solution while the solution was stirred continuously at 400 rpm to prevent possible concentration gradient and to speed up the absorption process. The SAP beads could be easily collected from the solution (after saturation) and replaced by new beads to precisely tune the solution concentration. This step was repeated until a homogeneous and highly concentrated solution was achieved. During the water absorption step a small amount of $Ti_3C_2T_x$ flakes adhered to the surface of SAP beads but they could be easily removed with DI water. The hydrogel beads change to their initial shape by simply keeping them at room temperature for a couple of days to evaporate the absorbed water.

3.2.4 3D Printing

A benchtop robotic dispenser (Fisnar F4200n) was used for the 3D printing MXene ink. The desired pattern was designed (AutoCAD, Autodesk Inc), transferred to the robotic dispenser, and printed using control software. The ink flow was controlled by a pneumatic fluid dispenser (DSP501N, Fisnar), the pressure of the dispenser and the printhead speed were ~4 psi and ~3 mm s^{-1}, respectively. For printing interdigital electrodes with various height, after printing the first layer (current collector), the ink was deposited layer by layer on the finger part of the interdigital electrodes to increase the height of the electrodes.

3.2.5 Fabrication of MSCs

Unless otherwise stated, a glass substrate (MAS-GP, Matsunami Glass, IND., LTD., Japan) was cleaned with DI water and used for printing. Although the ink has high conductivity and could be used as both current collector and active material, we found that sputtering a thin layer of gold on the substrate (underneath the printed current collectors) slightly improves the electrochemical performance of the devices. The gel polymer (PVA/H_2SO_4) electrolyte was prepared by first adding 1 g of PVA powder to 10 ml DI water with continues stirring at 85 °C until a clear solution was achieved. Then, 1 mL of H_2SO_4 (95.0-98.0%, ACS, Alfa Aesar, USA) was added to the mixture and stirred for another 1 h.

3.2.6 Material Characterization

The structure and morphology of the synthesized MAX powders and printed electrodes and devices were studied using a scanning electron microscope (JEOL JSM-7000F) equipped with an energy dispersive spectrometer (EDS detector).

3.2.7 Atomic Force Microscope (AFM)

AFM (Park Systems, NX10) was used to measure the size and thickness of the synthesized $Ti_3C_2T_x$ flakes. To prepare the AFM samples, a small amount of the solution was diluted with DI water and drop-casted on the pieces of thermally oxidized silicon wafers.

3.2.8 Rheology

Rheological properties of the prepared MXene inks were studied in collaboration with Dr. Davis group from Chemical Engineering Department at Auburn University using a strain-controlled rotational rheometer (Physica MCR301, Anton Paar). Fixture geometries (made of stainless steel) used for testing were parallel-plates (25 mm diameter) and cone and plate (25 mm

diameter, cone angle = 0.03 rad) to ensure there are no artifacts in the data due to testing geometry. After loading the rheometer with MXene ink at 25°C, multiple times up to 2 hours were selected to allow the sample to equilibrate and eliminate viscoelastic history before the investigation of rheological properties. A time of 20 minutes was chosen since no significant change was observed in elastic and storage moduli at a strain amplitude of 0.01 and steady shear viscosity data. All experiments were performed with a silicone oil coating along the edges of the fixtures and a solvent trap of deionized water to prevent water loss due to extended testing. A preliminary shear protocol was established at a shear rate of 0.01 s^{-1} to prevent structure change before measuring oscillatory dynamics.

3.2.9 Electrochemical Measurements

The fabricated symmetrical 3D MSCs electrochemical performance were tested using a VMP3 potentiostat (Biologic, France) using pieces of silver wire to connect the printed current collectors to the potentiostat cables. Silver wires were connected to the current collectors by a silver adhesive (fast-drying Ag paint, SPI Supplies). To protect the silver paint and wires from the electrolyte, nail polish was used to cover the contact area. The prepared PVA/H_2SO_4 gel electrolyte was carefully drop cast onto the printed $Ti_3C_2T_x$ interdigital electrodes and then dried in air overnight. Two-electrode configuration was used to test the printed devices. Cyclic voltammetry tests were performed at scan rates ranging from 2 to 1000 mVs^{-1} in a potential window of 0 to 0.6 V to avoid oxidation of MXene.[202] Electrochemical impedance spectroscopy was performed at open circuit potential, with a small sinusoidal amplitude of 5 mV, and frequencies of 10 mHz to 100 kHz. The areal, gravimetric, and volumetric capacitances were used to evaluate the electrochemical performance of the printed MSCs.[1]

Cell capacitance (*C/A*) was derived from the CV curve, according to the following equations.

$C = \frac{\int I(V)dV}{\upsilon.\Delta V}$ (F), (2-electrode configuration)

where 'I(V)' was the voltammetric discharge current (mA), 'υ' is the scan rate (mV s^{-1}), ΔV is the potential window (0.6 V).

The normalized areal (C/A) and volumetric (C/V) capacitances were calculated based on the total area and volume of the devices. The total area (A) was calculated considering the area of the interdigital electrodes and the space between the fingers and the total volume (V) was calculated by multiplying the total area by the maximum thickness of fingers (height of the electrodes) measured from SEM images. The following equations were used for calculating the normalized capacitances:

$$C/_A = \frac{C_{device}}{A}$$

and

$$C/_V = \frac{C_{device}}{V}$$

The power and energy densities of the devices were measured according to the following equations.

Energy density *(E)*= $\frac{C/A*V^2}{7200}$ (Wh cm^{-2})

Power density *(P)*= $\frac{3.6*E*\upsilon}{V}$ *(*W cm^{-2}).

where *C/A (F* cm^{-2}), V (V), and υ (mV s^{-1}) are as described above.

3.3 Results and Discussion

The first step in 3D printing of MSCs was the preparation of a printable MXene ink. The formulation of inks for extrusion printing requires consideration of solvent-particle interactions,

substrate wetting, solvent evaporation rate, and ink rheological properties.[168,191,195,197,210–212] Water is a favorable solvent for printing because it is environmentally friendly, has a moderate evaporation rate, and a low cost. Functionalized $Ti_3C_2T_x$ is hydrophilic, and preparation of a stable dispersion of its 2D flakes in water has been demonstrated before.[2,168] However, these colloidal dispersions are usually prepared at relatively low concentrations which lack the favorable rheological properties required for extrusion printing.[168]

In this research, the dispersions of $Ti_3C_2T_x$ flakes in water were prepared following a previously reported method as described in synthesis section above MXene Synthesis.[71] Briefly, $Ti_3C_2T_x$ was first synthesized by selective etching of Al atoms from the structure of Ti_3AlC_2 MAX phase particles in a LiF and HCl aqueous mixture solution. The produced $Ti_3C_2T_x$ was then dispersed in DI water and tip sonicated for 30 minutes to produce delaminated MXene flakes. AFM measurements showed that the synthesized MXenes are mostly single-layer flakes with an average lateral dimension of ~0.3 μm (**Figure 3-1 a**), which is consistent with previous reports.[208,213] However, the concentration of the prepared dispersions (~10 mg mL^{-1}) was too low to achieve the rheological properties required for extrusion printing.[168,198,210] Increasing the concentration of MXene dispersions by solvent evaporation is not straightforward. Evaporation of excess water under vacuum at room temperature is time-consuming and may result in agglomeration of $Ti_3C_2T_x$ flakes. In addition, increasing the temperature to accelerate water evaporation rate may result in the oxidation of $Ti_3C_2T_x$ flakes.[214] Therefore, the method reported by Akbari *et al.* [215] for concentrating graphene oxide dispersions by using SAP beads was adopted in this work for concentrating $Ti_3C_2T_x$ dispersions (**Figure 3-2**). As schematically demonstrated in **Figure 3-1 b**, the dispersion concentration was uniformly increased to as high as 290 mg mL^{-1}

(~28.9 wt%), proving that this simple method is very effective in the preparation of highly concentrated MXene dispersions.

The concentrated ink contained MXene flakes with an average flake size of ~0.3 μm and could be directly used for 3D printing of MSCs (**Figure 3-1 a** and **Figure 3-3).**

Achieving good dispersion quality, including homogeneity and controlled rheological properties, plays a critical role in the line width and uniformity of printed structures.[168,198,216] Shear thinning behavior (**Figure 3-1 c**) above yield stress that can be overcome in the print head is essential for a uniform flow out of a narrow orifice. **Figure 3-1 c** shows that the viscosity *versus* shear rate behavior of the 28.9 wt % (Ø= 7.5×10^{-2}) $Ti_3C_2T_x$ ink could be fit to Herschel-Bulkley model

$$\tau = \tau_0 + k\dot{\gamma}^n \qquad (1)$$

where τ_0 is the yield stress, $\dot{\gamma}$ is the shear rate, and k is the consistency factor, and n is the flow index. This resulted in the model parameters τ_0 = 24, k = 1.07, and n = 0.73, where the model maintains <10% error with the data. **Figure 3-1 d** highlights the dramatic decrease in viscosity that occurs at the yield stress.

The structure of the printed layers, including shape retention and interlayer adhesion, is largely determined by ink viscoelastic properties. An elastic modulus G' greater than the viscous modulus G″ (tanδ<1) enables the printed tracks to retain their shape while still having enough viscous character to enable interlayer coalescence. **Figure 3-1 e** shows that for the prepared MXene ink G′ is greater than G″ throughout the measured frequency range; the lower frequencies probe the long-timescale dynamics of the microstructural rearrangement prior to solidification while the higher frequencies probe shorter time scales. **Figure 3-1 e** also shows that G′ is nearly independent of frequency indicating a percolated (continuous) network of sheets even prior to the

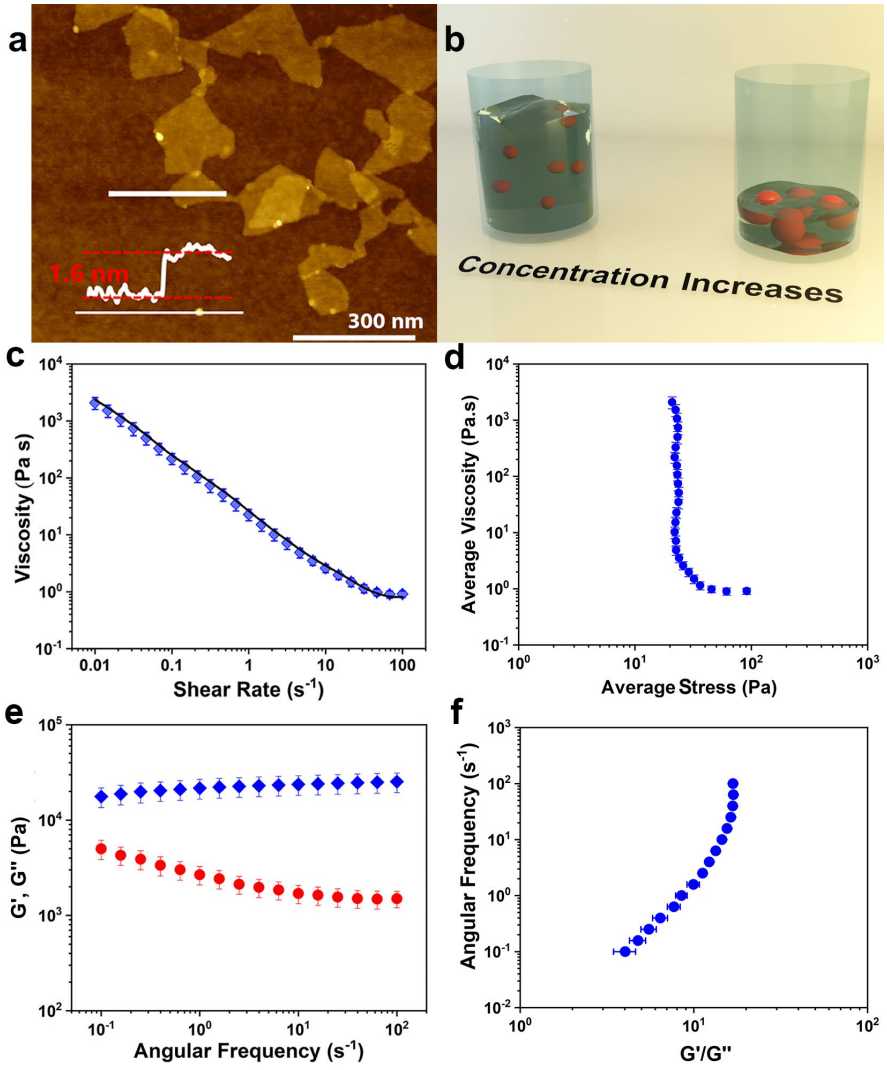

Figure 3.1. Schematic of MXene ink preparation and 290 mg mL^{-1} (~28.9 wt%) MXene ink rheology. (a) AFM image of the initial MXene dispersion confirming single-layer flakes. Inset is the height profile of the MXene flakes. (b) schematic of the MXene solution at low and high concentrations; adding SAP beads to the dispersion resulted in a uniform concentrated MXene solution. Steady shear rheological behavior (c) blue diamonds viscosity and line Herschel-Bulkley model fit, and (d) highlighting the dramatic viscosity drop at the yield stress. Small amplitude oscillatory shear (SAOS) data (e) show G′ (blue diamonds) > G″ (red diamonds) and G′nearly constant over the measured frequency range, and (f) ratio of G′ to G″ over the measured frequency range. Note: error bars represent standard error (n = 5 for SAOS data and n = 10 for steady shear data). Reproduced with permission [121] Copyright 2020, Elsevier Ltd. In collaboration with Dr. Davis group from the Chemical Engineering deparmetn at Auburn University

concentration increase accompanying solvent evaporation. The inverse of tanδ or G′/G″ *versus* frequency ω is increasingly being used to establish whether an ink has suitable viscoelastic behavior for specific processes including electrospraying, inkjet printing, fiber spinning, and extrusion printing.[168,210,212] Akuzum et. al.[168] predicted that for single-layer MXene $2< G'/G'' <20$ in the frequency range of $0.01< \omega <10$ Hz would be appropriate for 3D printing process. A similar range was found for the printing ink used in this work (**Figure 3-2 f**).

After material preparation and rheological measurements, the MXene ink was loaded into syringes with an attached tip (230-600 μm inner diameter) and used for 3D printing by a robotic dispenser (schematically shown in **Figure 3-4 a**). The ink was printed into fine lines and the ink was printed into fine lines and predetermined shapes in a layer-by-layer fashion. MSCs with interdigital architectures were fabricated using the prepared ink for printing both current collectors and 3D electrodes. Due to the viscoelastic properties of the $Ti_3C_2T_x$ MXene ink, the deposited layers were mechanically robust, and multiple layers could be stacked to achieve printed electrodes several millimeters in height without collapse (as demonstrated in **Figure 3-4 b**). Moreover, a variety of shapes and geometries could be printed with fabricated ink. For instance, the Auburn University logo with all its fine features was printed, as shown in **Figure 3-4 c**.

The produced MXene inks contained a large amount of water (~71 wt%), thus drying the electrodes in air resulted in the shrinkage of the printed electrodes. Interestingly, the electrodes mostly shrunk along the height of the electrodes; the shrinkage along the length and width of the electrodes was minimal. This is attributed to contact line pinning between the deposited MXene ink and hydrophilic substrates. After complete drying, the electrodes' thickness was reduced to between a few microns and one millimeter (depending on the number of deposited layers), which is a more appropriate height range for on-chip energy storage device.[1]

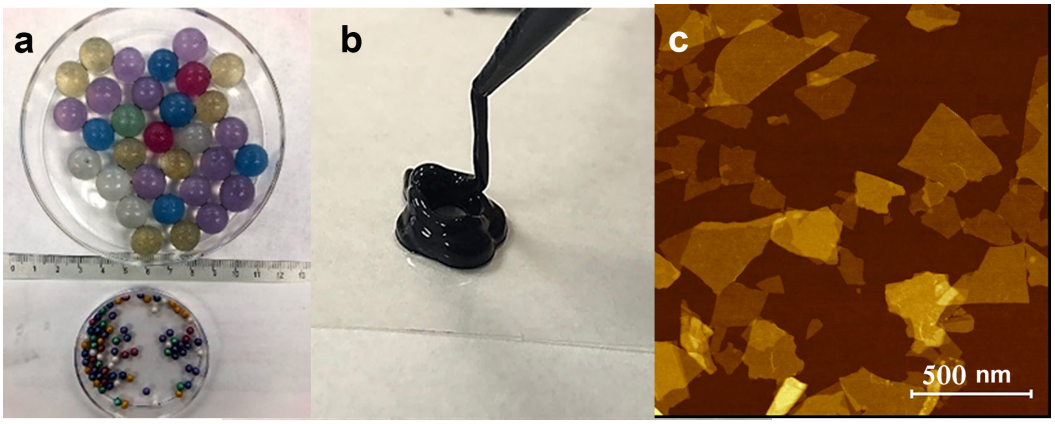

Figure 3.2. (a) Super absorbent polymer (SAP) balls were used to remove excess water from the prepared $Ti_3C_2T_x$ dispersion and increase its concentration. (b) Highly concentrated MXene ink prepared for 3D printing. The ink showed suitable viscoelastic properties. (c) An AFM image of the synthesized MXene flakes presented in the developed ink. To prepare the solution, small amount of ink was mixed with 50 mL of DI water and bath sonicated for 3 min. Reproduced with permission [121] Copyright 2020, Elsevier Ltd.

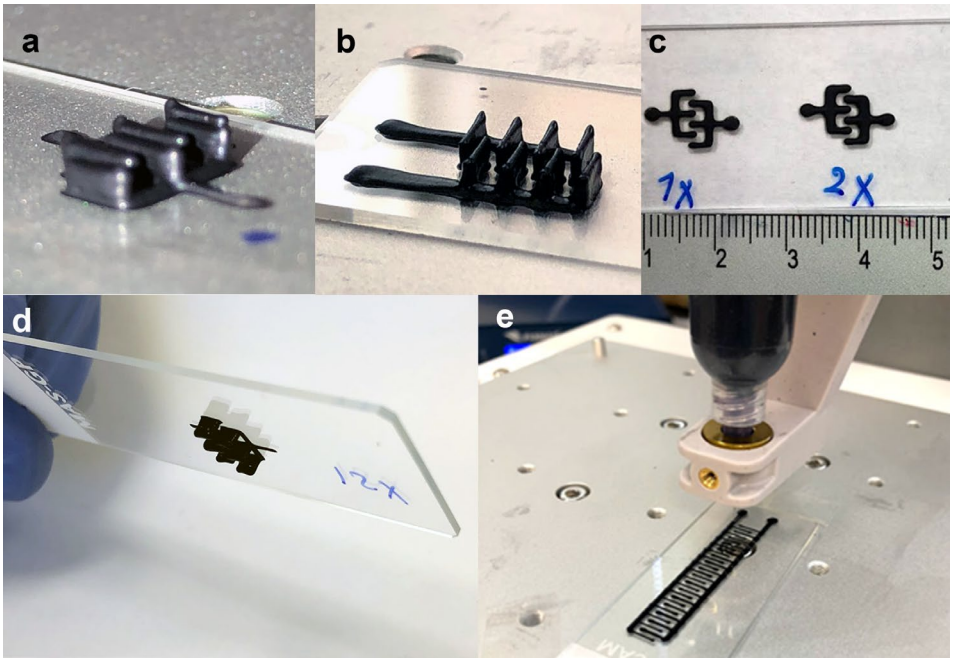

Figure 3.3. The prepared MXene ink was used to print MSCs with different designs and number of layers. (a, b) Printed interdigital MSCs before drying. (c) Top-view image of MSC-1 and MSC-2 after drying. (d) A photograph of MSC-12 device printed on a glass substrate before drying, showing the good adhesion of the printed electrodes to the substrate and the stability of the printed electrodes in wet condition. (e) Printing a device with 15 sets of interdigital electrodes with high accuracy on a glass substrate. Reproduced with permission [121] Copyright 2020, Elsevier Ltd.

MSCs with interdigital electrodes were printed on various substrates including glass slides, papers, Si/SiO_2 wafer, and polymer films (**Figure 3-5, Figure 3-6, and Figure 3-7**). For the fabrication of each device first the current collectors were printed, and then additional layers were printed only on the finger part of the patterns to the desired height (schematically shown in **Figure**

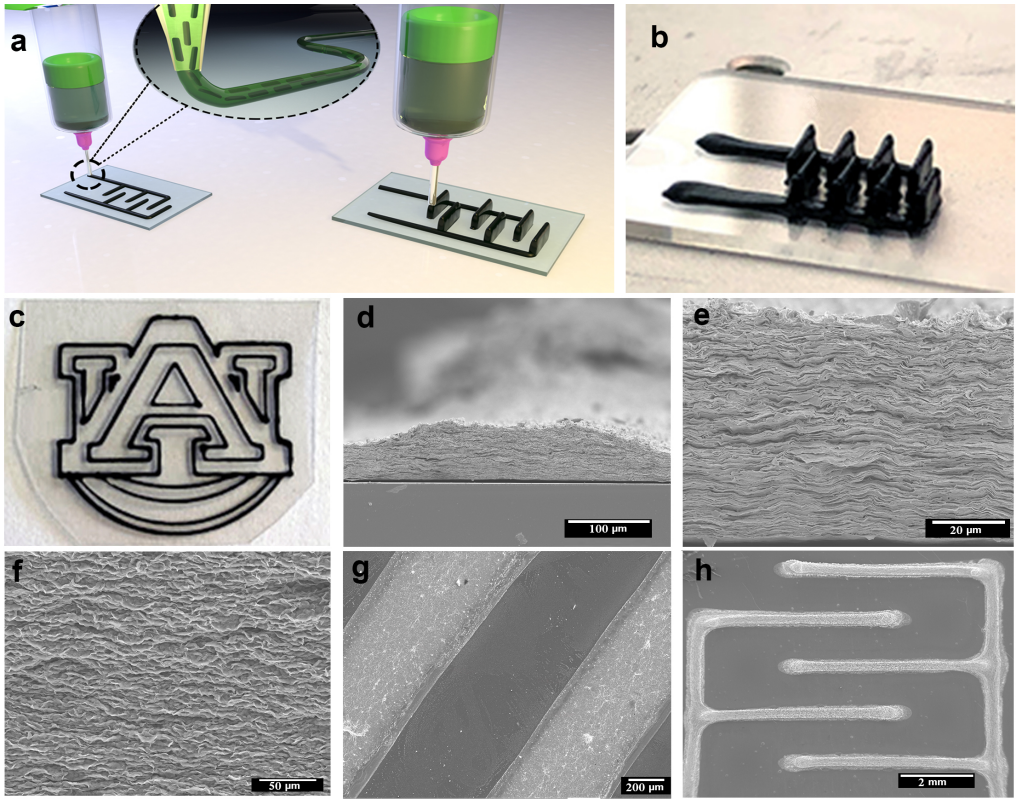

Figure 3.4. (a) Schematic drawing demonstrating the 3D printing of MSCs with interdigital architectures. The shear stress induced in the nozzle aligns the flakes resulting in their horizontal alignment in the direction of nozzle movement. The height of the printed electrodes can be increased by printing additional layers. (b) An optical image of MSC-10 device printed on a glass substrate before drying. (c) An optical image of the Auburn University logo printed on a polymer substrate using the prepared MXene ink (with permission from Auburn University, copyright 2019, Auburn University). (d-e) Cross-sectional SEM images of the electrodes in MSC-10 device in different magnifications showing that $Ti_3C_2T_x$ flakes are compactly stacked and horizontally aligned. (f) Side-view SEM image of MSC-10 showing alignment of $Ti_3C_2T_x$ flakes. Top-view SEM image of (g) MSC-1 device and (h) MSC-5 device printed on glass and polymer substrates, respectively. Reproduced with permission [121] Copyright 2020, Elsevier Ltd.

3-4 a). MSCs with higher electrode thickness were printed by increasing the number of deposited layers to 2, 5, and 10 layers. The fabricated devices were then labeled as MSC-n, where n designates the number of printed layers for interdigital electrodes in each device (e. g., MSC-10 has 10 layers of printed MXene ink). The measured height of the electrodes after drying at room temperature for MSC-1, -2, -5, and -10 were about 1.5, 3.5, 12, and 75 µm, respectively. The length and width of the interdigital electrodes, as well as the gap distance between electrodes, can be engineered by changing the size of the features in the designed device and adjusting the nozzle size and printing conditions. **Figure 3-5 d-f** show cross-sectional SEM images of electrodes in MSC-10 device, which show that the printed MXene flakes are horizontally aligned. We believe

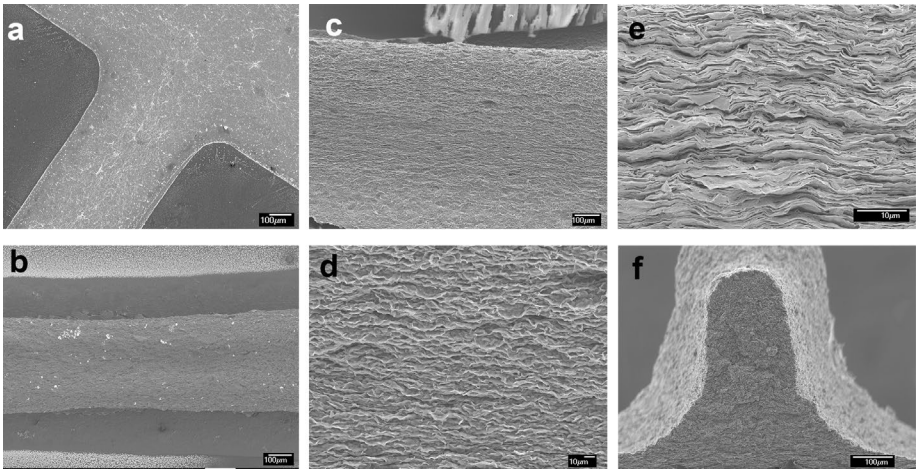

Figure 3.5. SEM images of the 3D printed interdigital electrodes with different thicknesses on a glass substrate. (a,b) Top view SEM images of MSC-1 and MSC-7, respectively. These images show the accuracy of the printing process in replicating the designed shape of the electrodes. The first printed layer was wider than the latter printed layers (scale bar is 100 µm). (c, d) Side view SEM images showing long rang horizontal orientation of MXene flakes in direction of nozzle movement with low (100X) and high (430X) magnifications (scale bar is 100 and 10 µm, respectively). (e) High magnification cross-section images of an electrodes with 10 printed layers showing the alignment of flakes (scale bar is 10 µm). (f) Increased electrode height by printing more layers of developed ink on top of each other (scale bar is 100 µm). Reproduced with permission [121] Copyright 2020, Elsevier Ltd.

this is due to the alignment of flakes in the nozzle during extrusion and their shear alignment in the direction of the nozzle movement during the printing.[194]

To perform electrochemical characterization on fabricated devices, a gel electrolyte based on PVA/H_2SO_4 was prepared and carefully drop cast onto the interdigital electrodes of printed devices. **Figure 3-8 a** shows the normalized CV curves of MSC-1 device at different scan rates. The capacitive charge storage behavior of the device can be inferred from the quasi-rectangular shape of the CV curves and the rapid current response upon voltage reversal. As shown in **Figure 3-8 b and Figure 3-9**, similar CV shapes were observed for MSC-2, MSC-5, and MSC-10 devices. **Figure 3-8c** shows galvanostatic charge-discharge (GCD) profiles of MSC-1 device at different current densities and **Figure 3-8 d** compares the GCD profiles of various fabricated MSCs at the same current density of 0.5 mA cm^{-2}. These figures show the near-linear change in the potential during both charge and discharge half-cycles for all the tested devices, confirming the capacitive

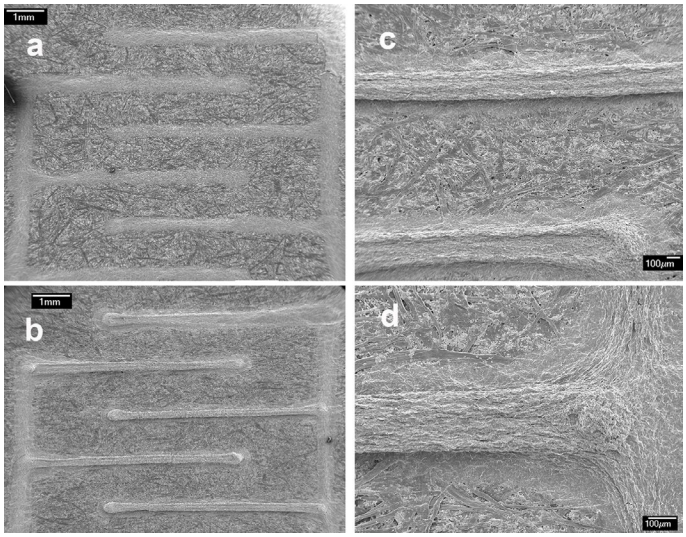

Figure 3.6. SEM images of 3D printed interdigital electrodes with different thicknesses printed on paper substrates. Low magnification (12X) top view SEM images electrodes (a) MSC-1 and (b) MSC-4 (scale bar is 1 mm). (c, d) Top view images of MSC-4 printed on a paper substrate (scale bar is 100 μm) showing the fingers and corners, respectively. Reproduced with permission [121] Copyright 2020, Elsevier Ltd.

performance observed by CV tests. Note that CV, GCD, and EIS results for all the fabricated devices at various scan rates and current densities. At a scan rate of 2 mV s^{-1} **(Figure 3-8 a**), the MSC-1, MSC-2, MSC-5, and MSC-10 devices show specific capacitances of 168.1, 315.8, 685.4, and 1035 mF cm^{-2}, respectively. shown in **Table 3-1**, the calculated areal capacitances, even for the device with only one printed layer (MSC-1), are significantly higher than the previously reported values for MXene-based MSCs, which shows the advantage of the 3D printing for the fabrication of high performance MSCs in limited footprint areas.

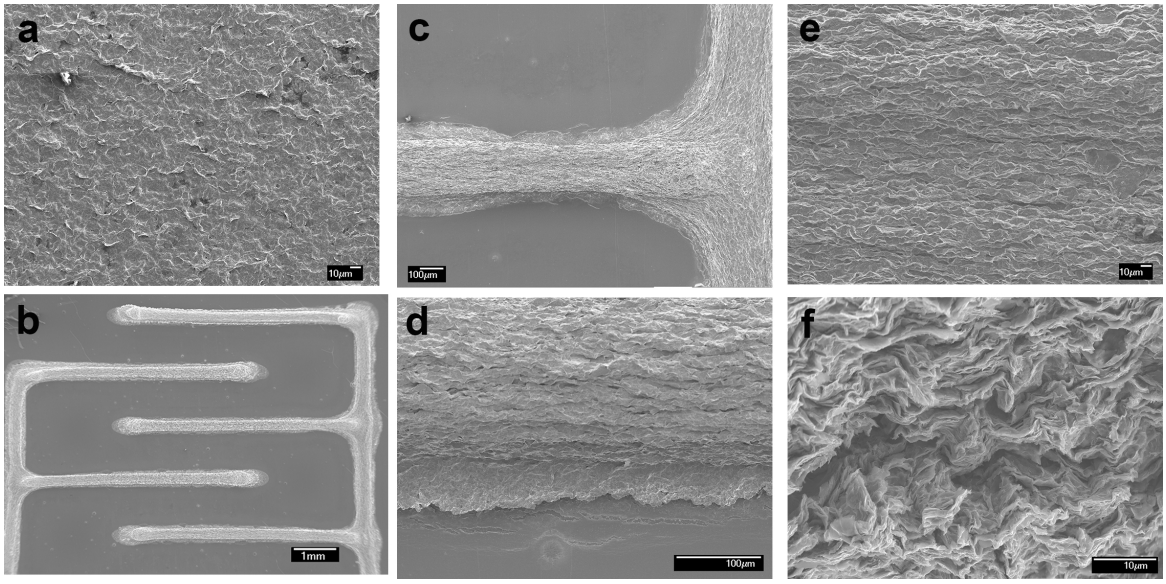

Figure 3.7. SEM images of 3D MSCF devices with different thicknesses printed on polymer substrates. (a) Top view SEM images of MSCF-1 device showing the formation of continues film after drying (scale bar is 10 μm). (b) Low (scale bar is 1 mm) and (c) high (scale bar is 100 μm) magnification SEM images of MSCF-5 device printed on a polymer substrate. For the polymer substrate, the first printed layer (current collector) was not as wide as the first printed layer on the glass substrate due to the higher contact angle of ink on the polymer substrate. (d) Low and (e) high magnification (scale bars are 100 μm and 10 μm, respectively) side view SEM images of MSCF-5, showing long rang horizontal orientation of MXene flakes in the direction of nozzle movement. (f) High magnification cross-sectional SEM images of an electrode in MSCF-5 device (scale bar is 10 μm). Reproduced with permission [121] Copyright 2020, Elsevier Ltd.

As expected, for all devices, the specific capacitance decreases with increasing the scan rate, and the rate of decrease is dependent on the number of printed layers. To better understand the electrochemical properties of the printed devices, we followed the method demonstrated by Zhang *et al.*[217] considering a capacitor in series with a resistor, to fit the specific capacitance data to the following equation

$$C/A = C_A\left[1 - \frac{\upsilon\tau}{\Delta V}\left(1 - e^{-\frac{\Delta V}{\upsilon\tau}}\right)\right] \quad (2)$$

where C/A, C_A, υ, τ, and ΔV are calculated areal specific capacitance, ideal areal specific capacitance, scan rate, time constant, and voltage window (0.6 V in this experiment), respectively. Although this equation is a simplification of the complex electrochemical response of the electrodes, it is useful for understanding the electrochemical behavior of the fabricated devices.[217]

For an ideal capacitor, the capacitance is not limited by the electrode conductivity and/or the accessibility and diffusion electrolyte. Thus, the areal capacitance is the slope of the line described by the equation $i = C_A \upsilon$ where i is the current density, C_A is the ideal areal capacitance, and ν is the scan rate.[218] Plotting the i *vs.* υ should lead to a linear relationship. However, in the presence of electronic and ionic resistivity, the above equation should be modified to $i = C_A\upsilon - C_A\upsilon e^{\frac{-t}{\tau}}$ where τ is the time constant and t is the discharge time.

As it is presented in **Figure 3-8 f**, *i vs.* υ at 0.3 V for various printed devices and clearly shows that deviation from the ideal performance is highly depend on the number of printed layers. Interestingly, at high scan rates the capacitance seems to be inversely proportional to the scan rate (υ^{-1}) which is incompatible with the Cottrell equation regarding the diffusion limited reactions ($\upsilon^{\frac{-1}{2}}$).[219,220] Zheng *et al.*[3] further modify the same equation to calculate the electrolyte conductivity and out of plane conductivity of their fabricated devices. They claimed that at high rates, the

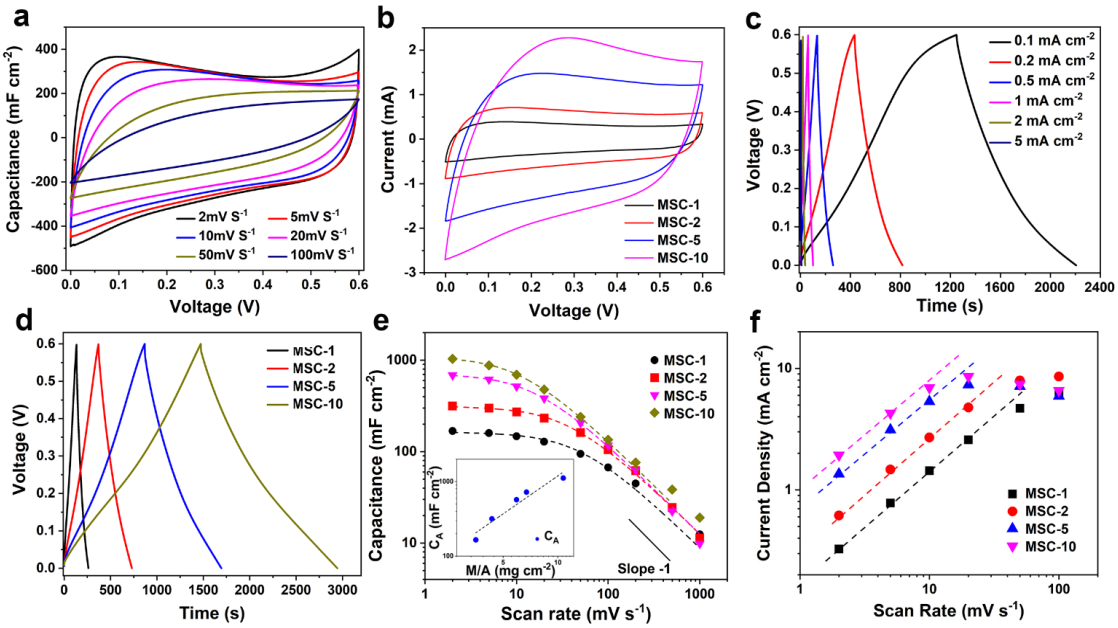

Figure 3.8. Electrochemical performance of all-MXene MSCs. (a) CV curves of MSC-1 at various scan rates. (b) CV curves at 5 mV s^{-1} for different MSCs. (c) Voltage *versus* time curves for MSC-1 at various current densities. (d) Voltage *versus* time curves at 0.5 mA cm^{-2} for different MSCs. (e) Areal capacitance as a function of scan rate for various fabricated MSCs. The inset graph shows the C_A derived from fitting data to Equation 2 as a function of mass loading of printed electrodes. The dashed curves represent data fitted to Equation 1. (f) Current density *versus* scan rate (at V= 0.3 V) for different MSCs. Reproduced with permission [121] Copyright 2020, Elsevier Ltd.

capacity retention is inversely proportional to τ. This further highlights the importance of conductivity, its effect on τ and in turn, its effect on devices performance, particularly at high rates.[3] For more insights regarding the derivation of the equation used in this paper the readers are referred to the papers by Higgins *et al.* [221] and Zhang *et al.*[217]

The changes in calculated C/A with increasing the scan rate were fit to Equation 2, and C_A and τ were calculated (dash lines in **Figure 3-8 e**). C_A *versus* electrode weight shows the specific capacitance almost linearly increases with increasing the mass loading of the electrodes for the printed MSCs (**Figure 3-8 e** inset). Also, the rate capability of the MSCs decreases with increasing the electrode height (number of printed layers). The series resistance of the devices, and the

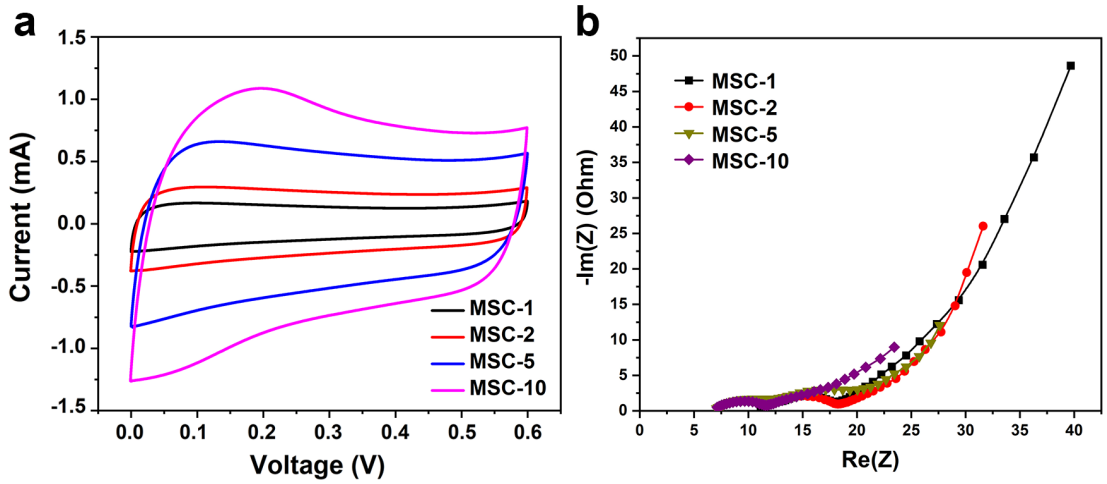

Figure 3.9. Electrochemical performance of fabricated MSC. (a) CV curve of MSC-1, MSC-2, MSC-5, and MSC-10 at 2mV s^{-1}. (b) EIS test for MCS1-10. Reproduced with permission [121] Copyright 2020, Elsevier Ltd.

resulting τ, significantly increase as the height of the electrodes increases (τ_{MSC-1}= 5.5 s, and τ_{MSC-10}= 24.3 s). An increase in τ result in a sluggish charge/discharge process and limits the capacitive performance and rate capability of the device, particularly at high rates. This is not surprising since the horizontal MXene flake alignment results in low out-of-plane electrical conductivity and the dependence of resistance on the electrode height (**Figure 3-8 f**).[220,222–224]

These results indicate that for the devices with thicker electrodes, the electrical properties of the electrodes limits their electrochemical performance, particularly at higher charging/discharging rates.[220] For example, the specific capacitance of the MSC-10 drops from ~695 mF cm^{-2} at 10 mV s^{-1} to ~20 mF cm^{-2} at 1000 mV s^{-1}. Furthermore, the cycling stability of the fabricated MSC devices were tested and over 90% capacity retention was achieved over 1200 cycles (**Figure 3-10**). We expect that the performance of these devices can be improved further by engineering the electrode structures and ink properties to increase their out-of-plane conductivity. It is worth mentioning that the rate performance of the fabricated devices is also dependent on their ion transport properties. Previous studies have shown that ion transport properties of MSCs can be

significantly improved by reducing the ionic diffusion path between the electrodes.[218] Therefore, we expect that regardless of the height of the electrodes, the rate capability and power density of the 3D printed MSCs can be improved by reducing the gap distance between the interdigital electrodes in modified device architectures.[165,180]

Table 3-1. MXene based MSCs electrochemical response comparison.

Material	Feature	Electrolyte	Scan Rate/ Current Density	Capacitance ($mFcm^{-2}$)	Energy density ($\mu Wh\ cm^{-2}$)	Ref.
$Ti_3C_2T_x$/Ppy	Freestanding film	0.5M H_2SO_4	30 mV s^{-1}	203	-	[217]
$Ti_3C_2T_x$/rGO	Composite aerogel	PVA/H_2SO_4	1 mV s^{-1}	34.6	2.2	[159]
$Ti_3C_2T_x$/MnO_2	Hybrid film	PVA/LiCl	1 A cm^{-3}	205	-	[225]
$Ti_3C_2T_x$	Spray coated, laser cut	PVA/H_2SO_4	20 mV s^{-1}	27.3	-	[206]
$Ti_3C_2T_x$	Laser cut	PVA/H_2SO_4	25 μA cm^{-2}	340	43500	[226]
$Ti_3C_2T_x$	Writing with Pen	PVA/H_2SO_4	-	5	-	[227]
$Ti_3C_2T_x$	Planar MSC	PVA/H_2SO_4	25 μA cm^{-2}	27.3	-	[228]
$Ti_3C_2T_x$	HF etched	PVA/H_2SO_4	-	10.5	0.21	[229]
$Ti_3C_2T_x$	Clay-like MXene laser scribing	PVA/H_2SO_4	-	25	0.77	[229]
$Ti_3C_2T_x$	Stamped film	PVA/H_2SO_4	25 μA cm^{-2}	61	0.76	[208]
$Ti_3C_2T_x$	Transparent film	PVA/H_2SO_4	4 μA cm^{-2}	1.4	0.05	[230]
$Ti_3C_2T_x$/Graphene	Spray coated film	PVA/H_3PO_4	5 mV s^{-1}	3.26	-	[132]
$Ti_3C_2T_x$	MSC	PVA/H_3PO_4	10 μA cm^{-2}	23	1.1	[231]
$Ti_3C_2T_x$	Ink jet print	PVA/H_2SO_4	4 μA cm^{-2}	12	-	[165]
$Ti_3C_2T_x$	Extrusion print	PVA/H_2SO_4	5 μA cm^{-2}	43	0.32	[165]
$Ti_3C_2T_x$/bacterial cellulose	Freestanding film	PVA/H_2SO_4	0.5 mA cm^{-2}	112.2	-	[125]
$Ti_3C_2T_x$/CNT	Freestanding film	1M KOH	2 mV s^{-1}	220	-	[59]
$Ti_3C_2T_x$/CNT	Printed	PVA/H_3PO_4	25 μA cm^{-2}	30.76	8.37	[172]
$Ti_3C_2T_x$/CNT	Spray coated layer by layer	1M H_2SO_4	10 mV s^{-1}	80	-	[153]

$Ti_3C_2T_x$	Extrusion print	PVA/H_2SO_4	1.7 mA cm^{-2}	2100 (per electrode)	24.4	[163]
$Ti_3C_2T_x$	Extrusion print MSC-1	PVA/H_2SO_4	2 mV s^{-1}	168.1	8.4	This work
$Ti_3C_2T_x$	Extrusion print MSC-10	PVA/H_2SO_4	2 mV s^{-1}	1035	51.7	This work

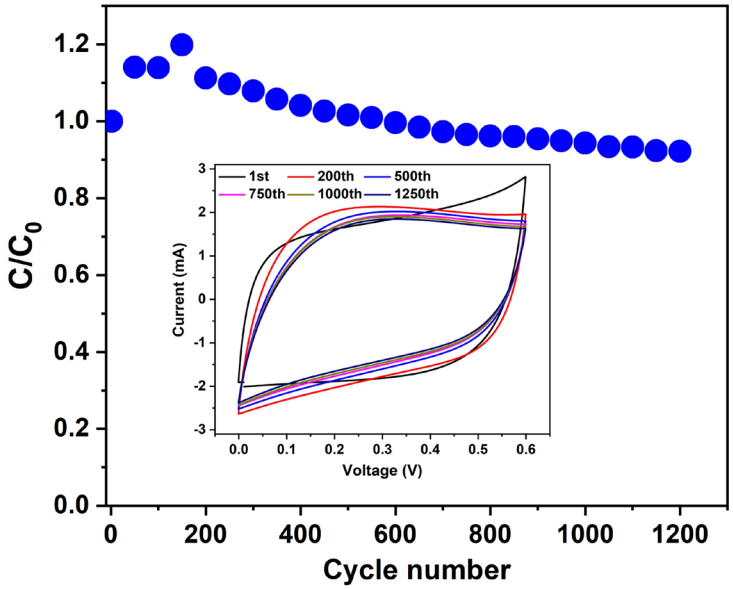

Figure 3.10. Electrochemical test results for MSC-2 device. Over 90% capacity retention of the printed device after 1200 cycles at 20 mV s^{-1}. Inset presents the CV curve of different cycles. Reproduced with permission [121] Copyright 2020, Elsevier Ltd.

One of the important advantages of room temperature printing using a water-based MXene ink is that it allows the fabrication of devices on a variety of substrates. Here, we demonstrate 3D printing of MSCs on polymer substrates (flexible polyester films), which enables their application in flexible electronics. MSCs printed on polymer substrates were subjected to bending and twisting at different angles and directions but showed no sign of crack or detachment from the substrate after the tests (**Figure 3-11 a**). The printed flexible devices were labeled as MSCF-n, where n denotes the number of printed electrode layers, and their electrochemical performance was evaluated. **Figure 3-11 b** shows the CV curves of the MSCF-1 at different scan rates and **Figure 3-11 c** compares the CV curves of MSCF-1, MSCF-2, MSCF-5, and MSCF-10 at 5 mV s^{-1} scan

rate. Fitting the calculated specific areal capacitances at various scan rates to Equation 2 showed the increased areal capacitance of the devices with increasing the height of the electrodes (**Figure 3-11 d** inset).

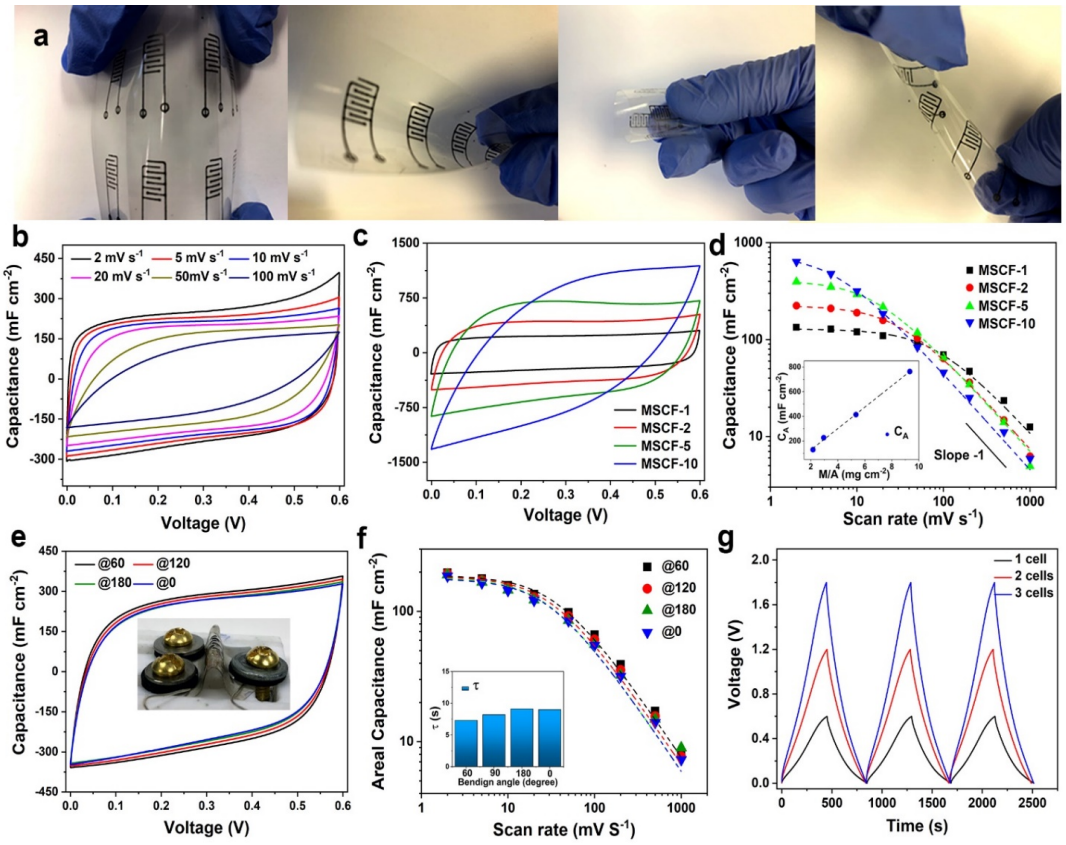

Figure 3-11. Electrochemical performance all-MXene MSCs printed on polymer substrates. (a) The printed devices showed excellent adhesion to the substrate during repeated bending and twisting. (b) CV curves of MSCF-1 at various scan rates. (c) CV curves at 5 mV s^{-1} for different MSCFs. (d) Areal capacitance *versus* scan rate for various flexible MSCFs. The inset graph shows C_A derived from fitting the experimental data to Equation 2 as a function of mass loading of the electrodes in MSCFs. (e) Electrochemical performance of MSCF-1 at a 10 mV s^{-1} scan rate under various bending angles (starting with 60° followed by 120°, 180°, and 0°). (f) Areal capacitance *versus* scan rate for MSCF-1 device at different bending angles. The inset graph shows the τ calculated based on Equation 2 for MSCF-1 device under different bending angles. (g) Voltage profile of fabricated MSCs at 0.2 mA cm^{-2} for different number of cells connected in series. In (d), (f), the dashed lines show the Equation 2 fits. Reproduced with permission [121] Copyright 2020, Elsevier Ltd.

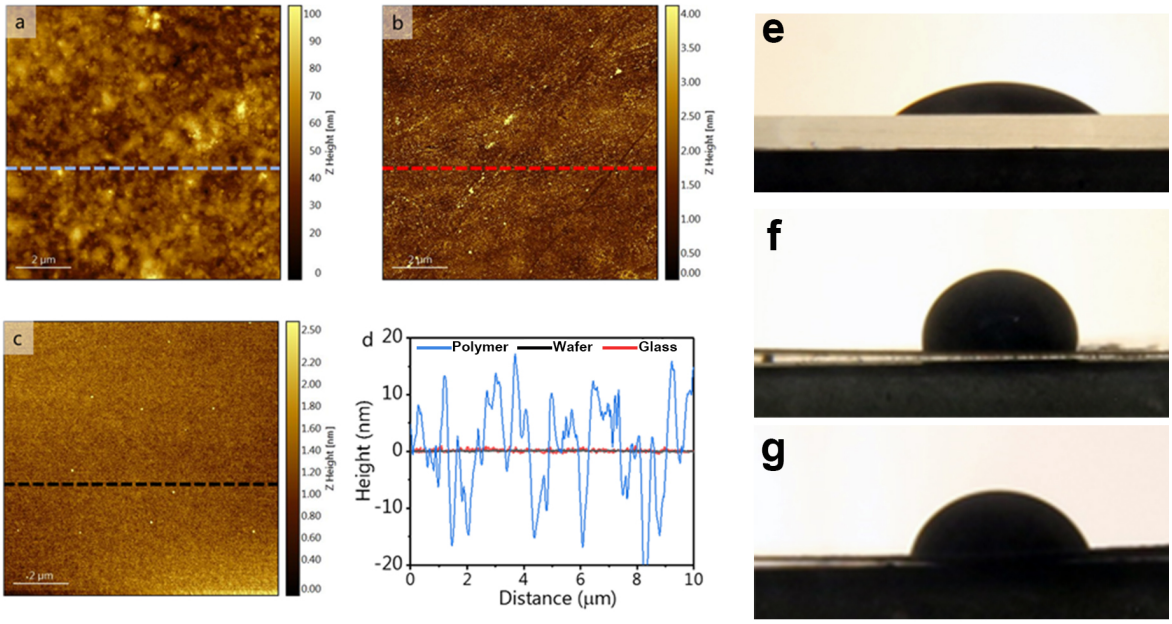

Figure 3.12. (a-c) AFM images of polymer, Si/SiO_2 wafer, and glass substrate used for printing in this study, respectively. (d) Height profile of different substrates showing different roughness. (e-g) MXene ink contact angle with glass, polymer, and paper substrates, respectively. Differences in surface properties of substrates resulted in wider printed layers on glass and Si/SiO_2 wafer substrates. Reproduced with permission [121] Copyright 2020, Elsevier Ltd.

However, the effect of electrode height on the rate capability and time constant of the devices was more pronounced compared to the devices printed on glass substrates. For example, the calculated τ for the MSCF-10 was 50.2 s, which is almost twice the calculated τ for the MSC-10 (24.3 s). We attribute this effect to the substrate wetting and roughness properties affecting the final shape and size of the printed electrodes. Although the dimensions of the designed interdigital electrodes and the size of the nozzle used for printing the MSCs on glass and polymer substrates were similar, the lower contact angle of the MXene ink on the glass substrate (**Figure 3-12**) produced wider printed electrode patterns compared to those printed on polymer substrates. Therefore, for the devices printed on glass substrate the contact between the electrodes and current collectors was more intimate, and the gaps between the electrodes were narrower; both contributed

to the higher device rate capability. This observation shows that the surface properties of the substrate play an important role in the properties of printing MSCs and should be further studied in our future work.

To test the flexibility of the MSCF devices, the effect of bending on their electrochemical performance was investigated. CV curves at 10 mV s^{-1} and rate capabilities of MSCFs at different bending angles are presented in **Figure 3-11 e and f**, respectively. The flexibility of the printed devices is demonstrated by the specific capacitance, rate capability, and the time constant of the MSCF not changing significantly with changing the bending angle.

The adaptability of the printing process for fabrication of MSCs on various substrates was further demonstrated by fabricating devices on paper using the MXene ink to print all the current collectors and electrodes. The printed devices showed very good adhesion to the paper substrate even after bending and twisting. The analysis of the electrochemical performance of MSCs printed on the paper substrate is presented in the **Figure 3-13**.

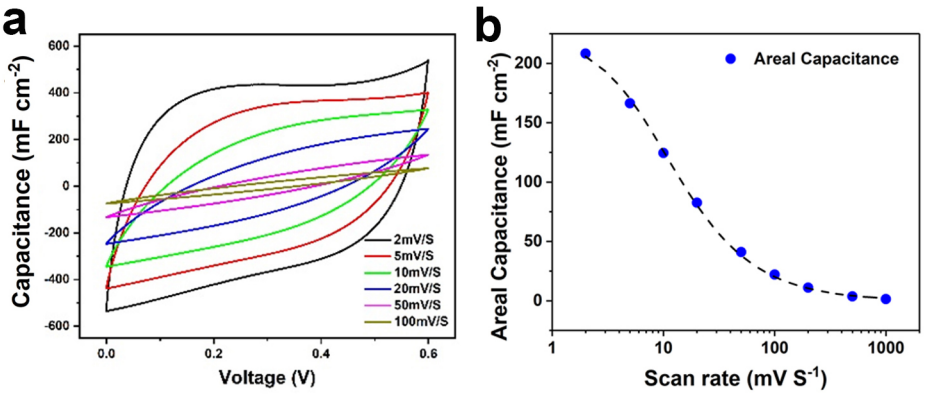

Figure 3.13. Electrochemical results for 3D printed interdigital device on paper substrate. (a, b) CV curve and calculated areal capacitance, respectively. The dash line represents the fitting of calculated capacitance to Equation 2 in the main article. Reproduced with permission [121] Copyright 2020, Elsevier Ltd.

To achieve higher power and energy densities, several MSCs connected in series or parallel can be printed on the same substrate. **Figure 3-11 g** compares the GCD profile of a single MSC-1 device with those of two and three devices connected in series. As expected, the operating voltage window increases for the devices connected in series.

The areal and volumetric energy and power densities of 3D printed MSCs were calculated and compared to some of the other reported devices in Ragone plots shown in **Figure 3-14.** The devices with one layer of printed interdigital electrodes (MSC-1 and MSCF-1) both show very high energy and power densities. For MSC-1, the calculated areal energy and power densities are 8.4 μWh cm^{-2} and 3.7 mW cm^{-2}, respectively, while volumetric energy and power densities are about 56 mWh cm^{-3} and 24.9 W cm^{-3}, respectively. As shown in the Ragone plots, these values are significantly higher than those reported for other MXene-based MSCs. MSC-1 also shows significantly improved volumetric energy density compared to some of the best performing and previously reported MSCs based on other materials. The highest measured areal energy and power densities for MSC-10 device were 51.7 μWh cm^{-2} and 5.7 mW cm^{-2}, respectively. As explained above, MSC-10 has a higher time constant compared to MSC-1, thus its power density rapidly declined with increasing the scan rate (**Figure 3-14 a**).

The results presented in this report on 3D printing of MXenes clearly show the advantages of extrusion printing for the fabrication of high performance MSCs. While the fabricated devices already show superior performance compared to previously reported MSCs, we believe that future research on the ink properties and printing process can lead to the fabrication of 3D MSCs with considerably higher energy and power densities. For example, the higher electrical resistance and time constant of devices with thicker electrodes can be addressed by using MXenes flakes with

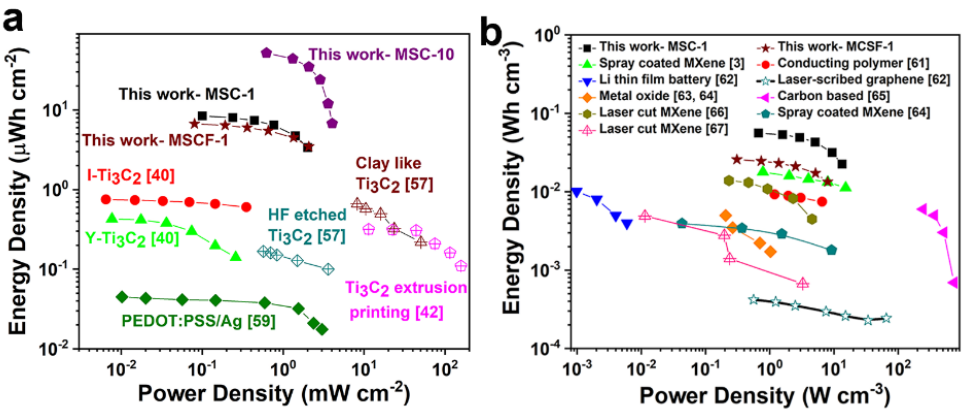

Figure 3.14. Ragone plots showing (a) areal and (b) volumetric energy and power densities of fabricated devices compared to previously reported data. [165,206,208,226,229,232–240]

Reproduced with permission [121] Copyright 2020, Elsevier Ltd.

larger average sizes to improve the electrical properties. Also, controlling the orientation of MXene flakes in the structure of the printed electrodes by modifying the printing process and controlling the ink properties is another possible avenue for improving the electrical and ionic transport properties of the 3D printed MXene electrodes.

3.4 Conclusions

We have demonstrated a method for preparation of an additive-free, water-based, printable MXene ink with rheological properties suitable for extrusion-based 3D printing. The prepared ink was used for printing of 3D MSCs with interdigital electrode architectures. The rheological properties of the ink, including low yield stress, shear-thinning behavior, and higher elastic modulus than viscous modulus allowed room temperature printing of devices that could be fabricated on a variety of substrates including flexible polymer and paper. The 3D printed MSCs showed outstanding areal capacitances that were improved by increasing the number of deposited layers and increased electrode height (1035 mF cm^{-2} at 2 mV s^{-1} for MSC-10). Furthermore, the maximum energy density of MSCs that we report here (51.7 μWh cm^{-2}) is significantly higher than

previously reported MXene-based devices. 3D printing of additive-free MXene inks also has importance beyond energy storage applications and can be implemented in electronic devices, electromagnetic shielding, sensors, antennas, and biomedical applications.

Chapter 4

MXene Aerogels with Ordered Microstructure as Electrodes in Li-ion Capacitors

This chapter presents the results of my research on a simple, efficient, and scalable process based on unidirectional freeze casting to fabricate ordered and porous 3D aerogels from 2D $Ti_3C_2T_x$ MXene flakes. The fabricated aerogels show excellent mechanical, electrical, and electrochemical properties. Our studies show that the processing conditions significantly affect the properties of MXene aerogels. The electrical conductivity and mechanical properties of fabricated aerogels directly correlate with their structural features. The mechanical test results showed that MXene aerogels with ordered structures could withstand almost 50% of strain before recovering to their original shape and maintain their electrical conductivities during continuous compressive cycling. As electrode materials for lithium-ion capacitors, the fabricated aerogels delivered a significantly high specific capacity (~1210 mAh g^{-1} at 0.05 A g^{-1}), excellent rate capability (~200 mAh g^{-1} at 10 A g^{-1}), and outstanding cycling performance. We believe that the MXene aerogels with ordered structures have promising properties for a broad range of applications, including energy storage devices and strain sensors.

4.1 Introduction

Assembling 2D materials into functional 3D structures can enable applications of these materials in various fields. 3D aerogels, hydrogels, and foams fabricated by the assembly 2D materials show interesting physical properties, such as high specific surface area, large porosity, low density, and interconnected conductive network [160,241,242]. Therefore, materials with 3D structures, such as aerogels, have shown promising performances for a range of applications including catalysis [243], stretchable electronics [156,244], supercapacitors [44,91,129], hydrogen storage [245], and environmental protection [74]. However, further implementation of aerogels based on 2D materials for functional applications is dependent on addressing various challenges specific to each application. For energy storage devices, such as batteries and electrochemical capacitors, one of the main challenges is engineering the structure of aerogels to enhance their ionic and electronic transport and mechanical properties to meet the requirements of practical usage. Another important challenge is the fabrication of aerogels using materials with intrinsically higher electronic conductivities and electrochemical performances.

In the past few years, much research has been dedicated to improving the properties of electrodes used in batteries and supercapacitors by understanding their structure-property relationships [4,246]. For aerogel electrodes based on 2D materials, controlling the porosity and the density of the electrodes to improve ionic and electronic properties have been a major theme of research as these properties can be readily controlled by changing processing conditions [247]. Further improvement of these properties can be achieved by controlling the orientation and the interconnected network of 2D sheets in the structure of aerogels, which is significantly more challenging. Herein, we report a general strategy based on unidirectional freeze casting to fabricate 3D freestanding MXene aerogels with excellent mechanical, electrical, and electrochemical

properties. The developed process is free of cross-linker or functionalization agents and offers control over the alignment of the 2D flakes in the fabricated 3D aerogels structure.

MXenes were first discovered by Naguib *et al*. [248] in 2011 and since then various members of this compositionally diverse family of 2D materials have shown excellent properties for applications such as energy storage and conversion, membrane separation, sensors, electromagnetic interference shielding, and many other applications [4,41,42,121,249–251]. MXenes are recognized with a general formula of $M_{n+1}X_nT_x$ where 'M' is a transition metal (such as Ti, V, Cr, etc.), X is C and N, T_x represents surface functional groups (O^-, OH^-, and F^- which are randomly distributed), and *n* is an integer between 1-3. MXenes are synthesized by selectively etching A-layer atoms (where A is a group 13 or 14 elements such as Al, Si, Ga, etc.) from the structure of layered MAX phases with the general formula of M_nAX_{n-1}, where M, X, A, and n are the same as described above [249]. The functionalized transition metal layer at the surfaces of MXene show oxide/hydroxide like properties and are redox-active, while the metal carbide inner layers of MXene show high conductivities and facilitate electron transport to electrochemically active sites [249]. The 2D layered structure of MXenes can be intercalated with water, organic molecules, and inorganic/organic ions, which often results in increased interlayer spacings of MXenes and improved ionic transport properties [249,252].

$Ti_3C_2T_x$, the first discovered MXene, has been extensively studied for electrochemical energy storage applications and has shown the potential to intercalate cations of different sizes and charges [4,10,37,73,109,248,252–254]. Several previous studies have explored strategies to improve the performance of $Ti_3C_2T_x$ electrodes tested in batteries and electrochemical capacitors by the design and synthesis of materials and electrode structures with enhanced ionic and electronic conductivities These include hybridization of $Ti_3C_2T_x$ with other nanomaterials such as carbon

nanotubes (CNTs) [129,255] and various polymers [31,41,140, 257], or synthesizing porous $Ti_3C_2T_x$ flakes [258]. Also, electrodes with 3D structures such as aerosgel films and structures formed by crumpled MXene flakes have been fabricated, and their improved ion accessibility has been reported [12]. However, the vast majority of studies on the electrical, mechanical, and electrochemical properties of various MXenes have been limited to freestanding films or thin films deposited on a substrate [42,44,249,251,255,258–262].

In this paper, the effect of process parameters such as freezing temperature and dispersion concentration on microstructure of MXene aerogels and their mechanical, electrical, and electrochemical properties are reported. A unidirectional freeze casting process was employed to control the alignment of the MXene flakes in the aerogel structure. It was found that aerogels fabricated by freeze casting at -70 °C using a colloidal dispersion of $Ti_3C_2T_x$ with a concentration of 9 mg mL^{-1} can be fully recovered from 50% of compressive strain. The current-voltage curves of the fabricated aerogels showed that their electrical conductivities follow the Ohm's law. The measurements of electrical resistance under cyclic loading confirmed the excellent electro-mechanical properties of MXene aerogels and their significantly robust structures. To examine their electrochemical properties, we studied the performance of MXene aerogels as electrodes of Li-ion capacitors and found that the microstructure of aerogel electrodes has an immense impact on their specific capacity, rate capability, and cycling performance. The properties of MXene aerogels with aligned MXene flakes demonstrate their high potential for a range of applications, including energy storage devices and strain sensors.

4.2 Materials and methods

4.2.1 Preparation of $Ti_3C_2T_x$ colloidal dispersions

The dispersions of $Ti_3C_2T_x$ in water were prepared based on a previously reported method [71]. Briefly, concentrated hydrochloric acid (HCl, ACS Grade, BDH) solution was diluted with DI water to obtain 20 mL of 9 M HCl solution. About 1g lithium fluoride (LiF, 98+% purity, Alfa Aesar) was added to the solution and stirred for 10 minutes using Teflon coated magnetic stir bars at room temperature. Then, 1g of Ti_3AlC_2 powder was slowly added to the solution (to prevent overheating). The mixture was transferred to a hot bath and kept at 35 °C for 24 hours while stirring. The mixture was then washed several times with DI water and centrifuged at 3500 rpm until the pH of the supernatant reached ~6. The MXene powder was collected, re-dispersed in water, and sonicated for 1 hour. The resulting dispersion was centrifuged at 3500 rpm for 1 hour, and the supernatant was collected and used as the base material.

4.2.2 Unidirectional Freeze Casting

The $Ti_3C_2T_x$ aerogels were prepared in collaboration with Dr. Lin group in the Industrial and Manufacturing Systems Engineering at Kansas State University by a unidirectional freeze casting process. This technique generally consists of freezing the liquid dispersion on a cold plate and then freeze-drying. Three $Ti_3C_2T_x$ dispersions with concentrations of 9 mg mL^{-1}, 7mg mL^{-1}, and 5mg mL^{-1} were prepared. Each dispersion (1.4 mL) was poured in a cylindrical aluminum foil mold with a diameter of 15mm, placed on a cold plate, and was kept there at the desired freezing temperature for 30 minutes for sufficient freezing. Then, the frozen samples were transferred to a -70 °C freezer and kept there for 24 hours. Repeating the same procedure, the temperature of the cold plate was adjusted to -50 °C and -30 °C to prepare the second and third batches, respectively.

Finally, all the frozen samples were transferred to a -35 °C freeze-dryer connected to a running vacuum pump (0.2 Pa) to prepare the $Ti_3C_2T_x$ aerogels.

4.2.3 Material Characterization

The images for investigating the microstructures of the aerogels were obtained using a SEM (HELIOS nanolab 600i, FEI). XRD was carried out on a Rigaku Smart Lab (Tokyo, Japan) diffractometer using Cu Kα radiation (40 kV and 44 mA) and step scan 0.02°, 3°–20° 2 theta range, and step time of 0.5s. A digital material testing device was used for performing the compression tests (Shimadzu Universal Testing Machine). All the compression tests were performed with a constant compression rate of 1 mm min^{-1}. The *V-I* plots for obtaining the electrical conductivity properties of the MXene aerogels were measured using a CHI 760D electrochemical workstation (CH Instruments, Austin, TX). The electrochemical properties of samples were tested in standard coin-type cells (CR-2032, MTI, Richmond, CA, USA). The $Ti_3C_2T_x$ freestanding films (punched), or $Ti_3C_2T_x$ aerogels (cut and pressed with 150 g weight) were placed on copper current collectors and tested as working electrodes. The reference and counter electrodes were Lithium metal foil. A polypropylene membrane (Celgard, Inc., Charlotte, NC) was used as the separator. The electrolyte was 1 molar Lithium hexafluorophosphate solution in ethylene carbonate and diethylcarbonate (1.0 M $LiPF_6$ in EC/DEC:50/50 (v/v)). Cyclic voltammetry was conducted at scan rates of 0.2 mV s^{-1} using a potentiostat (Biologic VMP3). The coin cells were tested in a galvanostatic mode within the voltage range of 0.01-3.01 V with respect to Li, using a battery tester (LANDT, China). Galvanostatic cycling was performed at current densities from 0.05 to 10 A g^{-1}. The mass loading of the working electrodes was 0.7-2 mg cm^{-2}.

4.3 Results and discussion

The process used for the fabrication of 3D MXene aerogels is schematically demonstrated in **Figure 4-1 a** MXene dispersions with known concentrations were poured into aluminum foil molds and were frozen by placing the molds on a cold plate with a precisely controlled temperature. Different freeze casting parameters, including casting temperature and dispersion concentration, were studied to find the optimal condition for $Ti_3C_2T_x$ aerogel synthesis. In unidirectional freeze casting, the temperature gradient between the cold plate and MXene dispersion is the driving force for the nucleation and directional growth of ice crystals from the bottom of the mold to its top [263]. During their growth along the temperature gradient, the ice crystals are ordered in submillimeter lamellar domains (shown in **Figure4-1 b and c**).

The MXene sheets are expelled from the freezing dispersion to the spaces between the ice crystals [264]. After the completion of the freezing step, MXene aerogels were fabricated by sublimation of the ice by a freeze-drying process and the pores replicate the lamellar pattern of the ice. The microstructure of the aerogels fabricated through this process showed that MXene flakes are well aligned along the temperature gradient during the freezing process (**Figure4-1 c**). The density of the fabricated MXene aerogels were in the range of 5.5 mg cm^{-3} to 11.3 mg cm^{-3}, depending on the concentration of the dispersion used in the process. The fabricated aerogels were ultra-light; they could be placed on a flower without any deformation of the plant fibers (**Figure4-1 d)**. **Figure4-1 e** shows a TEM image of a representative single-layer $Ti_3C_2T_x$ flake used in the aerogel fabrication. In addition, XRD patterns and AFM image of synthesized $Ti_3C_2T_x$ is presented in **Figure 4-2**.

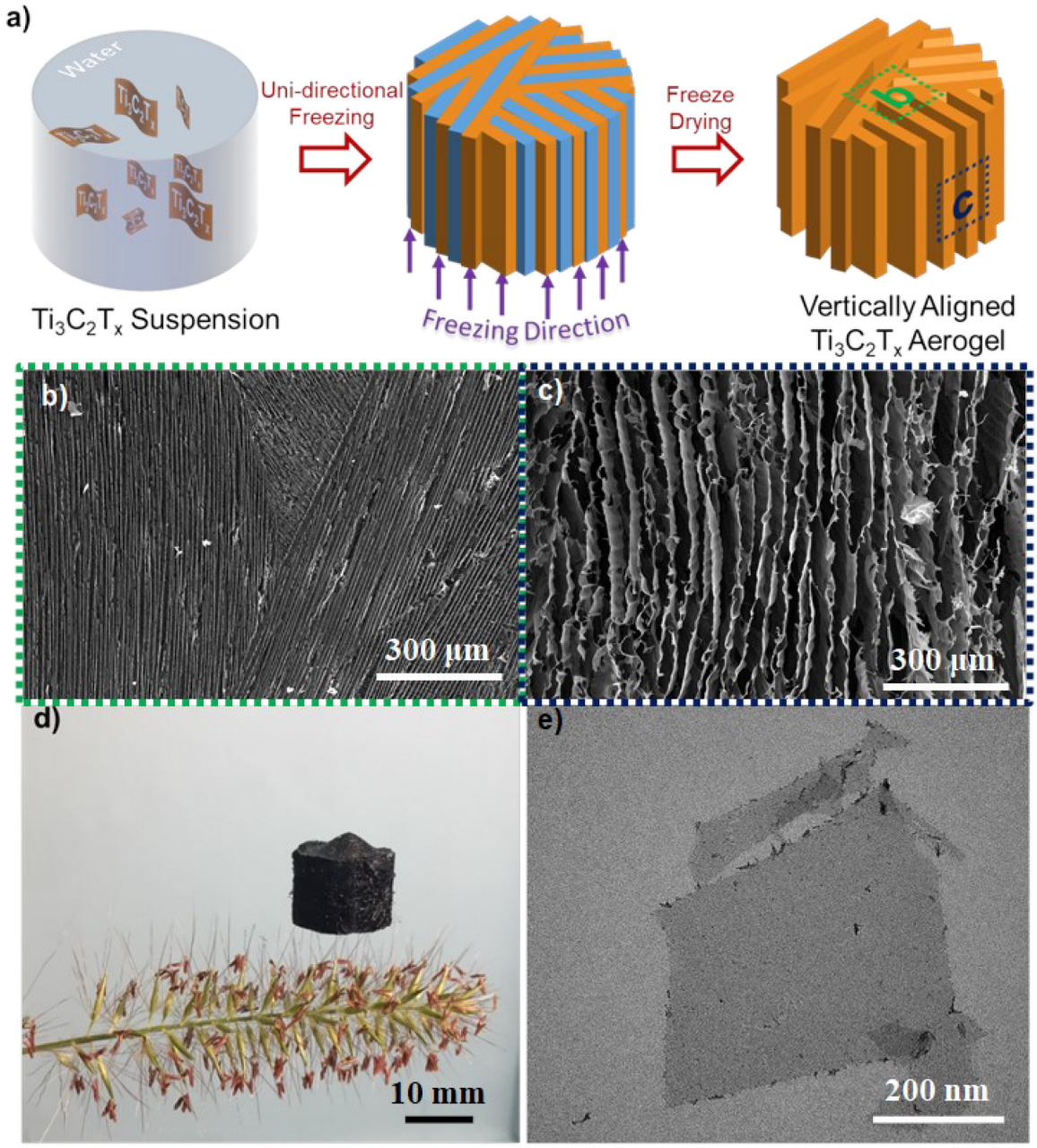

Figure 4.1. Schematic demonstration of the aerogel fabrication process. (b-c) Top view and cross-sectional view SEM image of MXene aerogels. (d) An ultra-light $Ti_3C_2T_x$ aerogel placed on a flower. (e) TEM image of a single-layer $Ti_3C_2T_x$ flake. In collaboration with Dr. Lin group from the Industrial and Manufacturing Systems Engineering department at Kansas State University.

The effects of fabrication conditions on the MXene aerogels microstructure were studied by comparing the top and cross-sectional SEM images of various aerogels fabricated using 5, 7, and 9 mg.mL^{-1} dispersions with freezing temperatures of -30 °C, -50 °C, and -70 °C. The SEM images comparing the effects of fabrication conditions are summarized in **Figure 4-3**. A more comprehensive presentation of SEM images of various samples can be found in **Figure 4-4**. The top-view SEM images of aerogels, shown in **Figure 4-3 a, c**, **and e** as well as **Figure 4-4**, showed that the MXene sheets are ordered in individual domains and cross-sectional SEM images of the microstructures shown in **Figure 4-3 b**, **d**, **and f** confirmed the alignment of the MXene sheets along the temperature gradient (from bottom to top).

The SEM images also showed the dependence of the microstructure of aerogels on the concentration of the dispersions used in their fabrication and the freezing temperature. For a fixed concentration, the aerogels prepared at lower freezing temperatures showed a morphology that consists of submillimeter domains with well-aligned MXene sheets inside each domain, while the

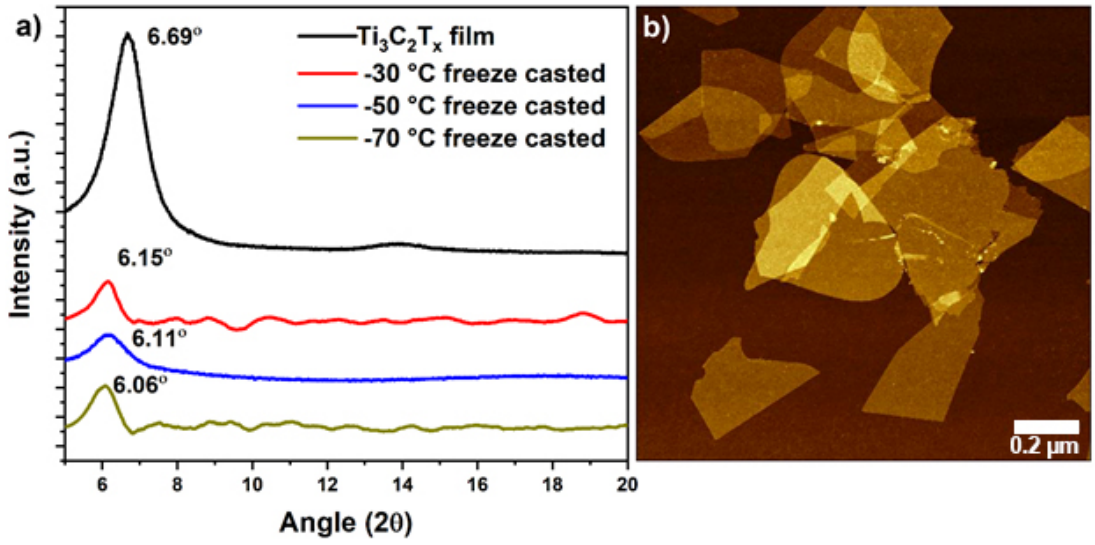

Figure 4.2. Characterization of fabricated aerogels. (a) XRD of the aerogels at different freeze casting temperatures. (b) AFM image of the synthesized $Ti_3C_2T_x$ flakes.

samples prepared at higher freezing temperatures showed less ordered structures (**Figure 4-3 c and e**). The difference in the microstructure can be related to the fact that at a lower freezing temperature, the ice crystals grow faster with smaller initial crystal nucleates, leading to the formation of thinner crystals in the MXene dispersion [104]. The thinner ice crystals also resulted in finer pores, as shown in **Figure 4-3 e and f**. The SEM images showed that the aerogel fabricated using the most concentrated MXene dispersion (9 mg mL^{-1}) and lowest freezing temperature (-70 °C) has a more uniform structure with distinguishable aligned MXene walls. However, the aerogel structures showed less uniformity and alignment when the concentration of dispersion was decreased, or freezing temperature was increased. The observed differences in the microstructures suggested that the aerogels fabricated using dispersions with higher concentrations and at lower freezing temperatures show better structural integrity, more aligned flakes, and finer pore structures, which can positively impact the mechanical, electrical, and electrochemical properties of the aerogels.

Understanding the mechanical properties of fabricated aerogels can help to evaluate their potential for various applications, where good mechanical properties are required. Fabrication of structures that combine the strength and stiffness of ceramics with high ductility usually requires advanced processing techniques [265–267]. Ti_3AlC_2, the parent MAX phase of $Ti_3C_2T_x$, is a stiff and relatively lightweight ceramic, which is also machinable and electrically conductive. Previously, the experimental characterization of MXene mechanical properties has been performed on cylindrical samples made by rolling MXene films (prepared by vacuum-assisted filtration) by Zhao *et al.*[44], demonstrating that a MXene film with a thickness of 5 μm can support ~4000 times its weight. The mechanical properties of MXene aerogels in this study were characterized by

conducting monotonic uniaxial compression tests and measuring the compressive stress (σ) as a function of strain (ε) [266,268–270].

The uniaxial compression tests were performed on aerogel samples prepared at different freezing temperatures using dispersion with different concentrations as mentioned previously. The results of in-plane compression tests of samples are summarized in **Figure 4-5.** The stress-strain curves contain five stepped compression cycles with strain magnitude of 10%, 20%, 30%, 40%, and 50% in sequence. The starting compression point of each cycle was the same and equaled the original height of the sample [271]. Interestingly, the stress-strain curves show that some of the fabricated aerogels can withstand almost 50% of strain and then recover to their original shape, demonstrating that for some processing conditions, the $Ti_3C_2T_x$ aerogels have a good compression capability and strain memory effect.

Reducing the freezing temperature at fix dispersion concentration significantly enhanced the structural integrity (**Figure 4-5 a and b**). Regardless of the freezing temperature, the aerogels prepared using a dispersion of lower concentrations of MXene did not show a good response to the compression force. Aerogels prepared using dispersions with a higher concentration (9 mg mL^{-1}) demonstrated a higher compressive stress tolerance and better structural integrity for all freeze casting temperatures (**Figure 4-5 c and d**). For the same dispersion concentration, the aerogels fabricated at lower temperatures showed higher compressive strengths. The samples prepared using a dispersion concentration of 9 mg mL^{-1} and freeze casting temperature of -70 °C demonstrated the highest compressive strength and the highest compression recovery capability under 50% of compression (**Figure 4-5 d**). The loading curves in **Figure 4-5 d** show the three distinct regions that are typically observed in mechanical testing of cellular materials, namely the initial Hookean region at $5\%<\varepsilon<10\%$, plateau region at $12\%<\varepsilon<26\%$, and densification region for

ε>30% with a sharp increase in stress [268,271]. The initial increase of stress for ε<5% is caused by the increase in the contact area between the sample and compression plate [271].

The observed hysteresis loops in the loading-unloading curves indicate the high energy dissipation capability of all the fabricated aerogels [271,272]. The energy dissipation can be attributed

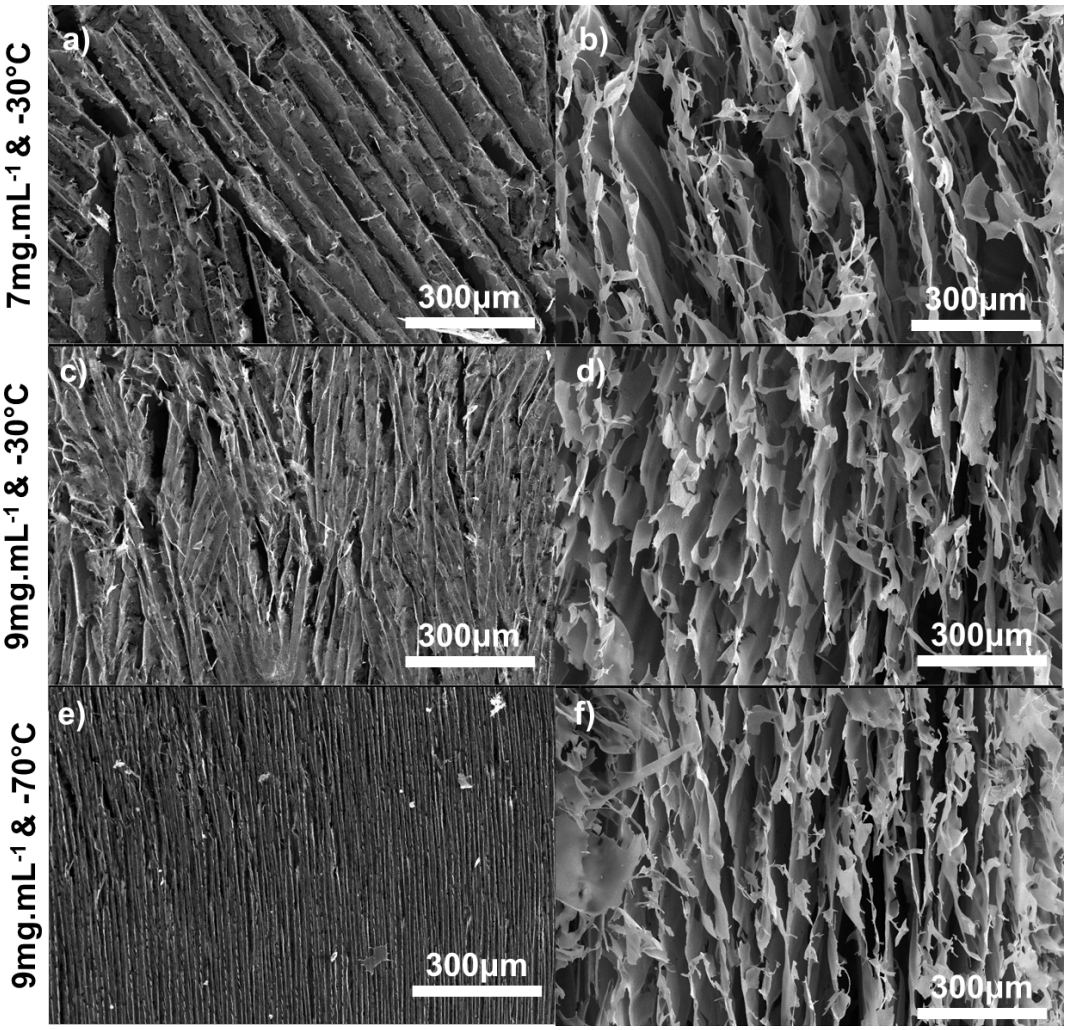

Figure 4.3. SEM images of the $Ti_3C_2T_x$ aerogels fabricated with different conditions. Top surface and cross sectional view of the $Ti_3C_2T_x$ aerogels prepared using (a-b) 7 mg.mL^{-1} dispersion with a freezing temperature of -30 °C, (c-d) 9 mg.mL^{-1} dispersion with a freezing temperature of -30 °C, and (e-f) 9 mg.mL^{-1} dispersion with a freezing temperature of -70 °C. SEM was preformed in collaboration with Dr. Lin group from the Industrial and Manufacturing Systems Engineering department at Kansas State University

to the buckling of 2D $Ti_3C_2T_x$ sheets, the adhesion forces between sheets that cause friction between them, and the formation of cracks under large compressive strains [271]. The linear elastic bending mode deformation of MXene sheets is primarily responsible for the Hookean region [271]. The plateau region that follows the Hookean region is primarily governed by the buckling deformation of MXene sheets [271].

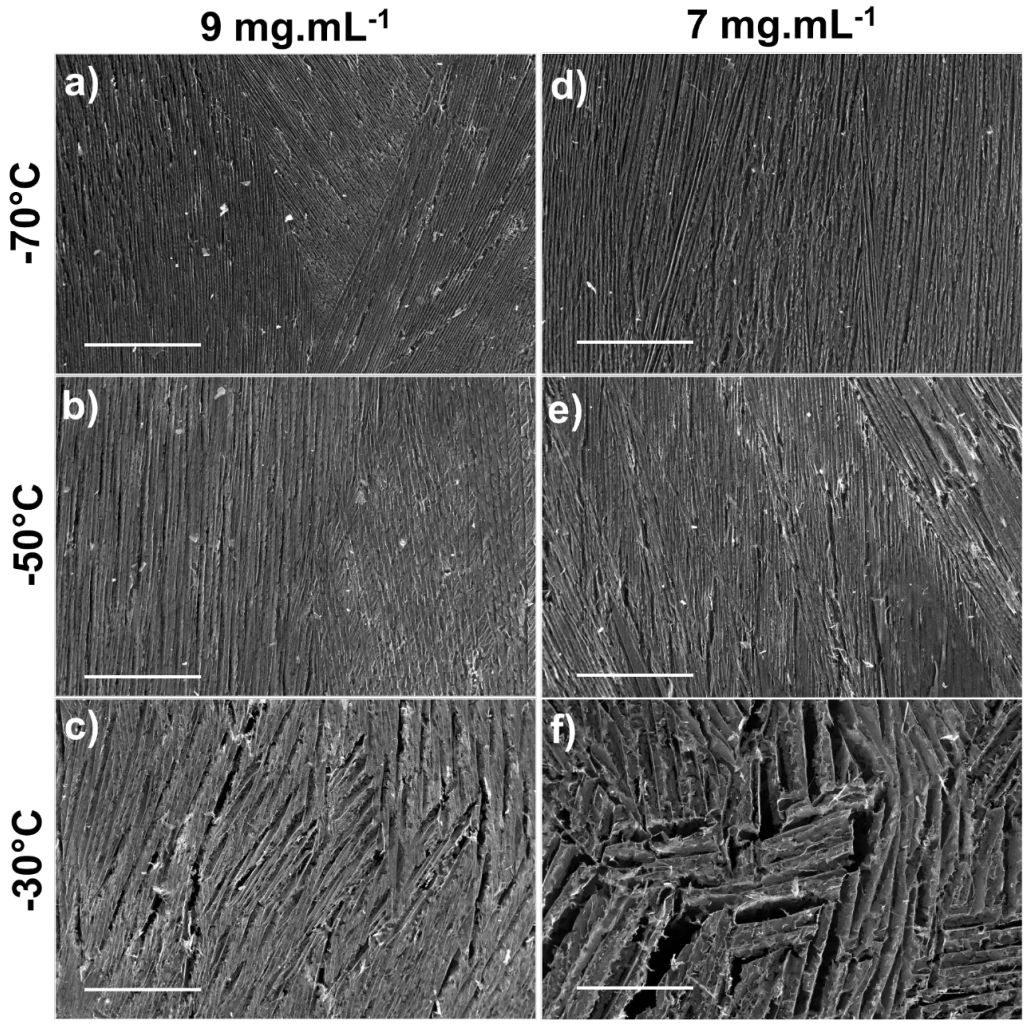

Figure 4.4. SEM images of the $Ti_3C_2T_x$ aerogels fabricated using dispersions with different concentrations and at various temperatures. (a-c) Top-view of MXene aerogels fabricated using a dispersion with concentration of 9 mg mL^{-1} at freezing temperatures of -70°C, -50°C, and -30°C. (d-f) Top-view of MXene aerogels fabricated using a dispersion with concentration of 7mg mL^{-1} at freezing temperatures of -70°C, -50°C, and -30°C. Scale bars are 500 µm.

To further determine the stability of the aerogels under cyclic loading, compression up to 10 % strain was applied for 100 cycles (**Figure 4-5 e**). The second loading-unloading curve exhibits a 5.2 % degradation of stress achieved in the first cycle, meaning that the $Ti_3C_2T_x$ aerogels maintain its original elasticity and structural robustness. It is worth noting that MXene aerogels have similar compression modulus values compared to other reported aerogels with similar relative densities (**Figure 4-5 f**) [273,274]. Overall, all the specimens demonstrated high compressive recovery capability, presenting unidirectional freeze casting as a feasible and reliable methodology to fabricate freestanding MXene aerogels for possible structural applications.

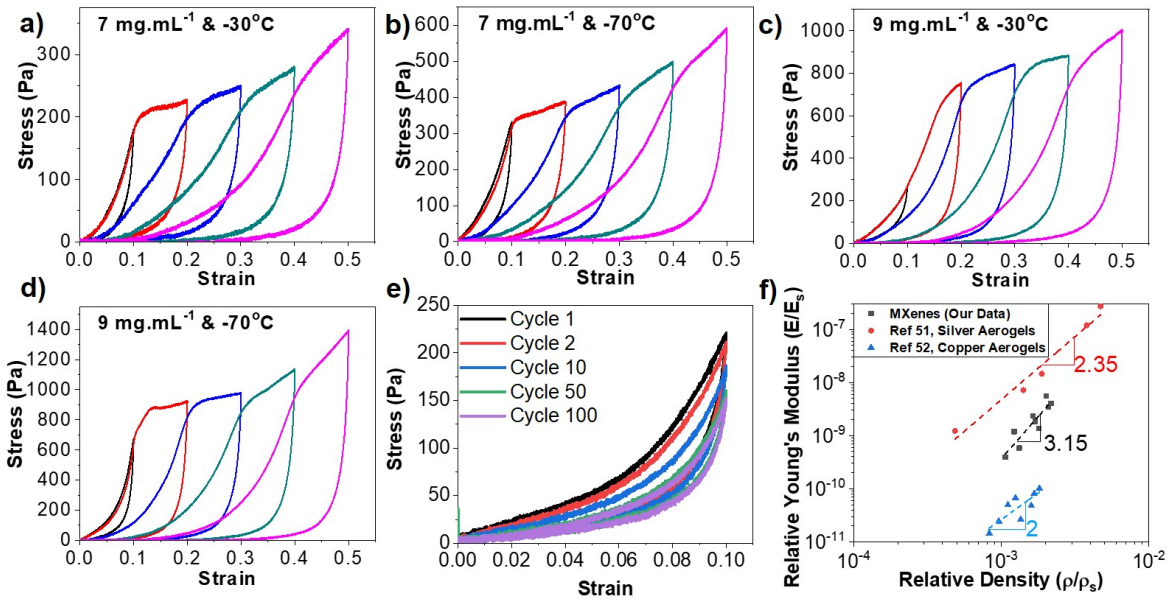

Figure 4.5. Mechanical properties of fabricated aerogels evaluated in collaboration with Dr. Lin group from the Industrial and Manufacturing Systems Engineering department at Kansas State University. (a-d) Stress–strain curve during loading–unloading cycles by increasing strain amplitude for MXene aerogels fabricated using 7 mg mL^{-1}, and 9 mg mL^{-1} dispersions with the freezing temperature of -30 °C, and -70 °C. (e) The 100 cyclic loading-unloading compression for $Ti_3C_2T_x$ aerogel fabricated from 9 mg mL^{-1} dispersion with a freezing temperature of -50 °C. e) Compression modulus vs. relative density of the fabricated aerogels and similar aerogels from the literature.

We further investigated the effect of MXene dispersion concentration and the freezing temperature on the electrical and electrochemical properties of the fabricated aerogel. **Figure 4-6 a** shows the current-voltage (I-V) curves of samples with different densities ranging from 5.5 to 11.3 mg cm^{-3}. The insert picture in **Figure 4-6 a** shows a demonstration of the high electrical conductivity of a MXene aerogel. The current responses of all aerogels followed Ohm's law, presenting a typical linear relationship with applied voltage [268,269]. For the same freezing temperature, an aerogel prepared using a dispersion with a higher concentration than 7 mg mL^{-1} demonstrates a higher current under the same applied voltage, which means it has a lower electrical resistance. Interestingly, the aerogels prepared at the freezing temperature of -50 °C show the

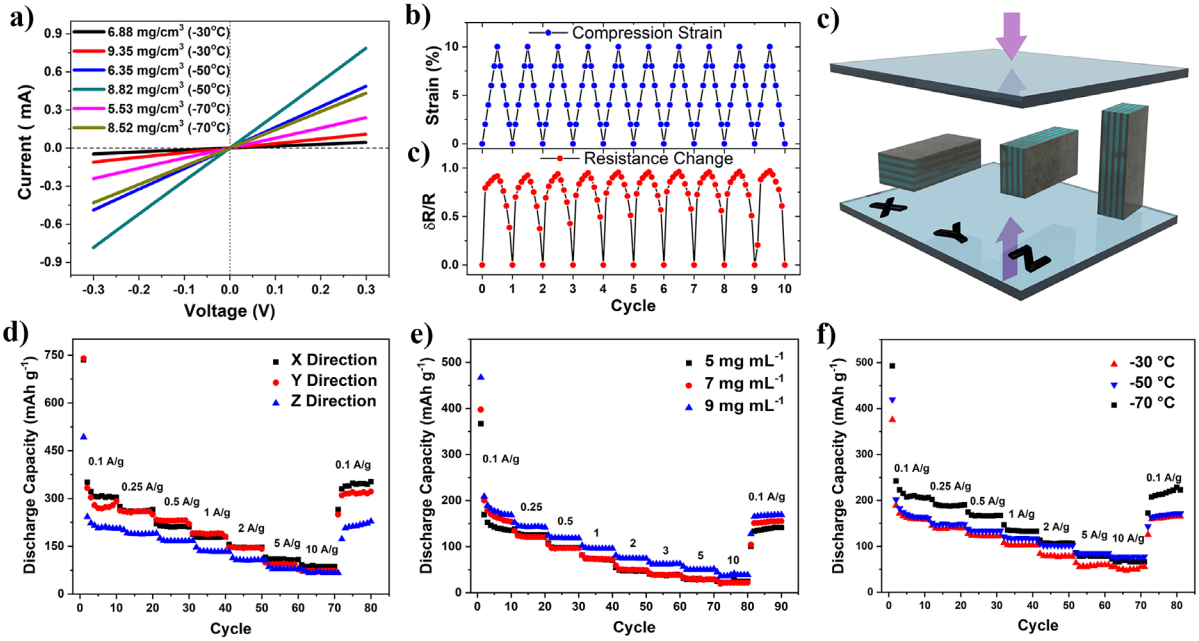

Figure 4.6. Electrical and electrochemical properties of MXene aerogels fabricated at different conditions. (a) I-V curves of MXene aerogels. The insert shows electrical conductivity of MXene aerogels. (b) Resistivity change against compressive cycles. (c) Pressing directions defined based on the direction of the domains. (d, e, f) Electrochemical performance of MXene aerogels based on pressing direction (9 mg mL^{-1} dispersion freeze casted at -70 °C), dispersion concentration (freeze casted at -30 °C), and freezing temperature (7 mg mL^{-1} solution). In collaboration with Dr. Lin group in the Industrial and Manufacturing Systems Engineering at Kansas State University.

lowest electrical resistance. The samples produced at -30 °C, -50 °C, and -70 °C freezing temperatures with 7mg mL^{-1} dispersion concentration showed electrical resistances of ~49.27×10^3 Ω mm, ~6.05×10^3 Ω mm, and ~12.53×10^3 Ω mm, respectively. The measured data suggests that electrical resistance increases rapidly as the density decreases as a result of the increased porosity and less inter-sheet junctions in the aerogels with lower densities [269]. As shown in **Figure 4-6 b**, the electrical resistance of the freeze-casted MXene aerogel is highly consistent over multiple compression cycles (10 cycles are shown in **Figure 4-6 b**), indicating the significant structural resilience of aerogels under cyclic loading [272].

The freeze-dried aerogels showed different domains and directions in their microstructures (**Figure 4-1**). Thus, the freeze casted samples were tested as electrode material for Li-ion storage in various directions (the aerogel was pressed between to glass slides before assembling a coin cell, as shown in **Figure 4-6 c**). The electrochemical studies indicated that pressing in the X direction (**Figure 4-6 c and d**) with minimum change in dimensions delivered the best electrochemical response compared with the other pressing directions, probably due to the minimal structural damage. The $Ti_3C_2T_x$ aerogel electrode delivered the initial discharge and charge capacities of 755 and 435 mAh g^{-1} respectively. The irreversible capacity loss in the first cycle is primarily attributed to the solid electrolyte interphase (SEI) formation, electrolyte decomposition, or irreversible reactions of various surface functional groups (O^-, OH^-, and F^-) [43,124,275–277].

The as-fabricated $Ti_3C_2T_x$ aerogel electrodes showed a gravimetric capacity of ~330 mAh g^{-1} at a 0.1 A g^{-1} current density (**Figure 4-6 d**). However, as explained below, the specific capacity of the MXene aerogels significantly increased after their continuous cycling. Nevertheless, the as-fabricated aerogel electrodes showed higher specific capacities compared to previously reported freestanding $Ti_3C_2T_x$ films.[4] They also exhibited a good rate capability due to their open pore

structures, which facilitates electrolyte transport while preserving their high electrical conductivity. Specific capacities of up to ~100 mAh g^{-1} and ~75 mAh g^{-1} were obtained at high rates of 5 A g^{-1} and 10 A g^{-1}, respectively. During the cyclic tests, for all samples, the coulombic efficiency rapidly reached ~100% after the second cycle and was constant during the remaining cycles. The electrochemical tests suggest that aerogels fabricated using dispersions with higher concentrations and at lower freeze casting temperature showed a better electrochemical response in terms of specific capacity and rate handling capability (**Figure 4-6 e and f**). It is worth mentioning that at high current densities, the aerogels freeze casted at -50 °C showed better electrochemical performance, which is in line with the higher electrical conductivity of these samples.

The cyclic tests of the aerogel electrodes showed that their capacities gradually increased during the first few hundred cycles. **Figure 4-7 a** shows the cyclic performance of a MXene aerogel electrode (fabricated using a 9 mg mL^{-1} dispersion with a freeze casting temperature of -70 °C) tested at a constant charge/discharge current density of 0.5 A g^{-1}. The specific capacity of the electrode dropped in the first ~15 cycles and then continuously increased over the next ~900 cycles followed by a steady performance for the remaining cycles. This continuous increase in capacity suggests that the accessibility of Li ions to the active sites between MXene layers improves over cycling [12,31]. The as-fabricated aerogels have porous structures, and the walls consist of several MXene layers. The interlayer spacing of these layers is not readily accessible to Li ions. During each cycle, the intercalation of Li ions, which may be completely or partially dissolved, increases the interlayer spacing and more ions can intercalate between the layers in the subsequent cycles. Therefore, the specific capacity of the aerogel electrodes continuously increases until the maximum expansion in the interlayer spacing is achieved. The porous structure of aerogels allows

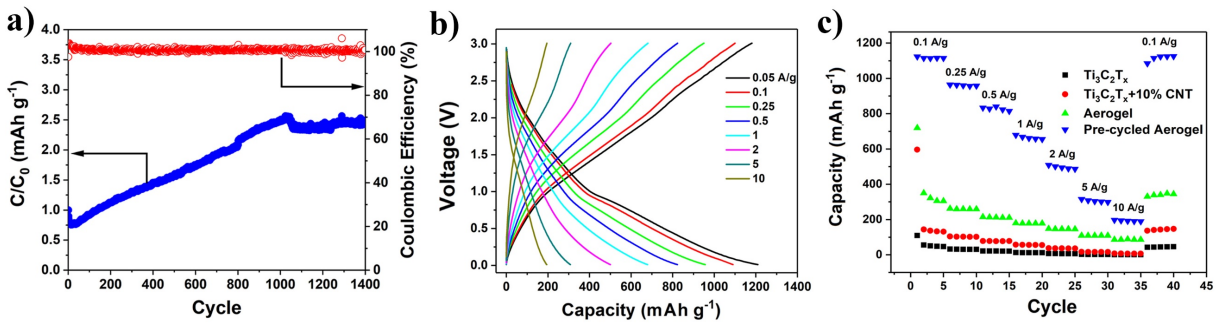

Figure 4.7. Li ion storage performance of $Ti_3C_2T_x$ aerogels electrodes. (a) Capacity retention, cycling stability, and Coulombic efficiency of $Ti_3C_2T_x$ aerogel electrodes test at a current density of 0.5 A g^{-1}. (b) Voltage profiles of pre-cycled aerogel at various current densities (A g^{-1}); (c) Discharge capacities at different current densities for $Ti_3C_2T_x$ aerogels, films and $Ti_3C_2T_x$-CNT composite film**.**

the expansion of the interlayer spacing while preserving the structure of the electrodes and electrical connectivity of MXene flakes. Also, the ordering of the flakes in the structure facilitates the uniform expansion of their interlayer spacing. Therefore, we believe that the porous structure of the as-fabricated aerogels has an immense impact on this electrochemical activation phenomenon (i. e., the improved performance of the electrodes during each cycle). As shown in **Figure 4-8 a**, when a freestanding MXene electrode fabricated by vacuum-assisted filtration was tested under the same conditions, it showed much lower initial capacity (14 mAh g^{-1} at 0.5 A g^{-1}) with a slight increase of capacity over cycling.

The cycled aerogel electrodes were tested at different current densities to understand the effects of the electrochemical activation on the performance of the electrodes (**Figure 4-8 a**). The CV test result of the first few cycles showed a pseudo-rectangular shape with very broad lithiation and de-lithiation peaks, representing the capacitive performance of the electrodes (**Figure 4-8 b**), which is in line with previous reports of the MXene electrodes for Li-ion capacitors. The CV tests were also performed on electrodes after 700 charge-discharge cycles at 0.5 A g^{-1} and showed similar pseudo-rectangular shape with the substantially increased area due to the improved

capacity of the electrodes after cycling **(Figure 4-8 b)**. Therefore, the CV and voltage profiles of the aerogel electrodes showed that they are excellent electrodes for Li-ion capacitors.

The cycled electrodes (cycled for a few hundred cycles) were tested at various current rates, which showed their excellent cyclability and rate handling capability. A high specific capacity of ~1210 mAh g^{-1} was achieved at 0.05 A g^{-1}, which gradually decreases to ~200 mAh g^{-1} at a very high current density of 10 A g^{-1} (**Figure 4-7 b and c**). As explained above, we attribute the significant improvement in the electrochemical performance of the electrodes to the improved ionic transport properties of the aerogels due to the increase in the interlayer spacing. It is worth noting that the measured specific capacities of the cycled electrode at all current densities significantly exceed those previously reported for MXene Li-ion capacitors tested at the same current densities.[4] The performance of the MXene aerogel electrodes was compared with two of the most commonly tested electrode structures for MXenes, freestanding films of MXene or MXene/CNT hybrids, fabricated by vacuum-assisted filtration. The cycled aerogel electrodes

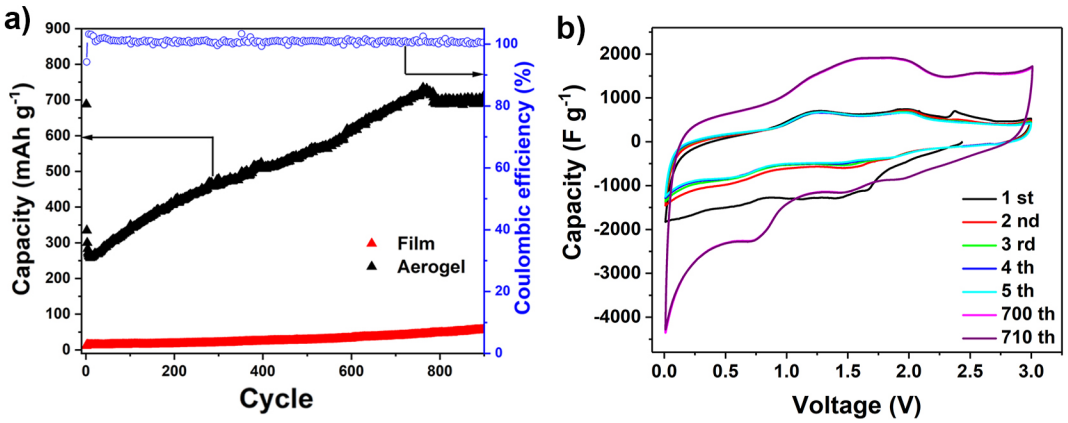

Figure 4.8. Electrochemical properties of MXene-based aerogels. (a) Cycling stability and Coulombic efficiency of pristine $Ti_3C_2T_x$ film and aerogel electrodes tested at current density of 0.5 A g^{-1}. (b) CV curve of MXene aerogle fabricated with 9 mg mL^{-1} dispersion at -70 °C at 0.2 mV s^{-1}. The first 5 cyclys and after 700 cycles at current density of 0.5 A g^{-1}.

showed significantly higher specific capacities compared to these electrodes at all tested current densities.

4.4 Conclusion

In summary, freestanding, binder and additive-free, and ultralight weight (density below 11.3 mg cm^{-3}) MXene aerogels with ordered structures were fabricated through unidirectional freeze casting. It was demonstrated that the processing conditions, such as freezing temperature and dispersion concentration, can control the structural, mechanical, electrical, and electrochemical properties of fabricated aerogels. Our studies of the morphology of MXene aerogels showed the alignment of MXene flakes in submillimeter domains along the temperature gradient. The compression tests showed that MXene aerogels could withstand and recover from compressive strains up to 50%. The MXene aerogels showed superior electrochemical response with excellent cyclic stability, high specific capacity, and excellent rate performance. The electrochemical studies of the aerogels, as electrodes for Li-ion capacitors, showed that the capacity of the electrodes gradually increases during the cycling. After activation with cycling, the MXene aerogel electrode showed outstanding performance, surpassing the performance of previously reported $Ti_3C_2T_x$ electrodes tested as electrodes for Li-ion capacitors. We believe that employing strategies to prevent restacking of the MXene flakes during aerogel fabrication would eliminate the need for electrochemical cycling to achieve maximum capacity. Also, we believe that the electrical and mechanical properties of the MXene aerogels make them a promising candidate for a range of other applications. For example, the excellent electro-mechanical properties of MXene aerogels under cyclic loading can be exploited to fabricate high performance strain sensors.

Chapter 5

Electrochemical properties of MXene-based 3D printed Li-ion microbattery

This chapter presents my research results on a simple, straightforward, and cost-effective printing process to print Li-ion microbattery. The printing parameter effect on printing outcome and the electrochemical performance of the fabricated microbatteries are studied. In a broad range of applications, including energy storage, flexible electronics, and sensors, additive manufacturing is considered a promising device fabrication technique due to its potential for developing complex architectures and using a variety of materials. Extrusion-based 3D printing is a low-cost and straightforward method that offers rapid and precise fabrication of "on-chip" batteries and supercapacitors with 3D architectures. This study reports developing functional nanocomposite inks based on 2D MXenes, with the application in lithium-ion storage. The developed nanocomposite inks are incorporated with 2D MXene flakes as a conductive additive that can provide the rheological properties required for the extrusion-based 3D printing without any other additive or binder. The inks were prepared by mixing lithium iron phosphate and lithium titanate nanoparticles with a highly concentrated water-based MXene ink and were directly used to print the cathode and the anode electrodes of a Li-ion microbattery, respectively. A programmable printing machine was used in the fabrication process that follows the layer-by-layer deposition of

the nanocomposite ink. The developed inks and printing methodologies facilitate the rapid fabrication of microbatteries, while the number of deposited layers can control the loading of active material per area of the device. Printing parameters such as applied pressure and nozzle speed effects on printing outcomes are studied, and their relations are discussed. The fabricated Li-ion batteries showed a high areal capacity of 4.7 mAh cm^{-2} at the current density of 0.1 mA cm^{-2} due to the enhanced ionic diffusion enabled by cell geometry and good electrical conductivity. The developed inks have the potential to be used in various applications and fields, including sensors and wearable electronics.

5.1 Introduction

Micronized energy storage devices gain more and more attention due to the high demands for power sources in various applications such as portable and wearable electronics and electric vehicles.[1,4,206,278] Mircosized lithium-ion batteries (LIBs) with 2D planar structure and slime shapes (i.e., coin, cylinder, and punch cells) are the prime examples of such energy storage devices. Most of these LIBs adopted thin film configuration (thin electrodes, polymer or ceramic separators, and current collector foil) does not meet the requirements to power miniaturized electronics. Thus, LIBs with enhanced electrochemical performances such as higher areal capacity and faster charge-discharge rates are desirable.[1] Researchers have been trying to develop new battery materials, architectures, and fabrication methods to improve the mentioned properties. For example, electrode materials such as MXene/Si composite reported to improve Si-based electrode's electrochemical performances, such as cycling stability and rate capability.[279] 2D MXene flakes provide a 3D conductive network to enhance the electronic conductivity and shorten the Li-ion diffusion pathway, while Si particles offer a high capacity.[279] Developing composite materials may

result in the synergistic effects that can enhance the electrochemical and mechanical properties of fabricated electrodes.[4]

On the other hand, electrode fabrication methods such as magnetron sputtering, chemical vapor deposition, and hard template method have been employed to fabricate thick electrodes to improve areal capacity by increasing the load of active material per area.[280–284] However, the longer Li-ion diffusion pathways, lack of control over electrode geometry, complex processes, and high cost limits their application. Extrusion-based 3D printing, as a noble fabrication method, has been employed to fabricate complex 3D electrode architectures for LIBs with high accuracy.[191,192,197,285,286] The 3D structure can enhance the ions transfer kinetic by providing a shorter diffusion path and lower resistivity in a porous structure, resulting in the increased energy density in a limited footprint area compared with conventional 2D planar structures.[1,121,190,286,287]

Extrusion-based 3D printing, also known as direct ink writing, due to its broad range of materials selection, simple procedure, and low cost of the fabrication process, gain attention.[4,285,286,164,7,288] To facilitate 3D printing, developing an ink with favorable rheological properties (high viscosity and shear-thinning behavior) is necessary.[4,121,168,288] Recently, MXene dispersion has shown unique viscoelastic properties, and remarkable printing capabilities as an aqueous dispersion to fabricated energy storage devices wherein its rheological behavior varies noticeably with the MXene sheet size and concentration.[121,164,168,289,165] At low MXene concentrations, the dispersions exhibit liquid-like behavior, which is not suitable for 3D printing. With increasing the MXene dispersions concentration, the MXene-based ink shows a gel-like behavior with high viscosity and elastic modulus, which can be employed to print desired shapes and geometries such as fine filaments or complex 3D architectures.[121,164,168,289,165] The developed MXene-based inks were used to directly printed fine filaments and increase the load of active

material per area in a layer-by-layer deposition strategy to develop diverse architectures with improved properties (e.g., high surface area, high electrical conductivity, enhanced electrochemical performances, and good structural stability).[7,121,163–166] It is anticipated that diverse applications of MXenes combined with their unique viscoelastic properties will create a new class of printable MXene-based inks with various functional components that can be employed to engineer advanced 3D-printed structures, architectures, and systems. Thus, extended applications of 3D-printed MXene-based composite inks are awaiting exploitations, especially in miniature energy storage devices and sensors.

The research on 3D printed LIBs was pioneered by Lewis and co-workers that formulated printable inks compose of active materials (lithium iron phosphate (LFP) and lithium titanate (LTO)) and cellulose-based polymer additives to control viscosity without conductive additives.[192] The fabricated electrodes showed low electrical conductivity, which adversely affected the electrochemical performance. To enhance the LIB performance, Fu et al. employed graphene oxide as the conductive additive to design a high viscosity printable ink having LTO and LFP as the active material.[197] The fabricated 3D-printed full cell delivers initial charge and discharge capacities of 117 and 91 mAh g^{-1} with a high load of active material per area (18 mg cm^{-2}).[197] Employing graphene oxide necessitates the use of an annealing process to transform graphene oxide to reduced graphene oxide. To the best of our knowledge, while 2D MXene-based inks showed promising properties, including good viscoelastic properties and electrical conductivity, they have not been employed to fabricate 3D-printed LIBs.

In this chapter, we report the development of $Ti_3C_2T_z$-based multifunctional composite inks to design, fabricated, and test the electrochemical performance of 3D-printed LIBs. Using water as the solvent in MXene-based composite inks enabled safe processing and drying steps while

being inexpensive. The highly concentrated $Ti_3C_2T_z$-based ink enables the 3D printing process, bind the electrode materials together, and form a conductive network. LFP and LTO were selected due to their low volume change during cycling and their thermal stability. The load of active material per unit area is controlled by the number of deposited layers (in a layer-by-layer fashion) on desired parts of the interdigital electrode configuration using a preprogrammed printing routine. The effect of various printing parameters are studied, and their relations are discussed. The MXene flakes were aligned in the extrusion direction due to the shear force induced by the nozzle, enhancing electrical conductivity. The fabricated LIB cells showed outstanding electrochemical performances, demonstrating MXene-based composite inks combined with 3D printing technology possesses a potential to be further investigated in various fields, including energy storage and sensors. We believe that other active materials such as Si and transition metal oxides can be used in the ink formulation as they showed enhanced performance when mixed with 2D MXene.[4,98,117,141,142,279,290,291]

5.2 Materials and methods

5.2.1 MXene Synthesis

The $Ti_3C_2T_z$ suspension was prepared based on a previously reported method.[69] Briefly, concentrated hydrochloric acid (HCl, ACS Grade, BDH) solution was diluted with DI water to obtain 20 mL of 9 M HCl solution. 1.6 g lithium fluoride (LiF, 98+% purity, Alfa Aesar) was added to the solution and stirred for 10 minutes using a Teflon coated magnetic stir bar at room temperature. The solution was then moved to an ice bath, and 1g of Ti_3AlC_2 powder was slowly added to the solution. The resulting mixture was transferred to a hot bath (35 °C) and kept for 24 hours (stirring at 550 rpm). The mixture was then washed several times with DI water and

centrifuged at 3500 rpm until the supernatant pH was >5. The supernatant was then collected without further sonication. The washing step continued, and the supernatant was collected and used as the initial solution.

5.2.2 Ink Preparation

The printable MXene ink was produced without any additives or high-temperature drying based on our previously published work.[121] The MXene dispersion collected in the washing steps was directly used in this step. The dispersion's concentration was increased by adding super absorbing polymers (SAP) beads to the dispersion to absorb water. To speed up the absorption process and prevent possible concentration gradient, the solution was stirred continuously at 400 rpm. After saturation, the SAP beads were collected from the dispersion, and new SAP beads were replaced to adjust the dispersion concentration. A highly concentrated and homogeneous MXene dispersion was achieved by repeating this step. The SAP beads are reusable after the absorbed water is evaporated.

5.2.3 3D printing

The 3D printing of MXene-based inks was performed using a benchtop robotic dispenser (Fisnar F4200n). AutoCAD (Autodesk Inc) software was used to design different patterns. Desired patterns were transferred to the robotic dispenser and printed using control software. A pneumatic fluid dispenser was used to adjust the pressure (DSP501N, Fisnar). To increase the load of active material per area, MXene-based inks were deposited in a layer-by-layer fashion on the finger part of the interdigital electrodes.

5.2.4 Material Characterization

The structure and morphology of the synthesized MAX powders, printed electrodes, and devices were studied using a scanning electron microscope (JEOL JSM-7000F) equipped with an energy dispersive spectrometer (EDS detector). Electrical conductive was conducted by using a four-point probe method to measure the 3D printed electrodes.

5.2.5 Atomic force microscope (AFM)

AFM (Park Systems, NX10) was used to measure the size and thickness of the synthesized $Ti_3C_2T_z$ flakes. To prepare the AFM samples, a small amount of the solution was diluted with DI water and drop-casted on the pieces of thermally oxidized silicon wafers.

5.2.6 Rheology

Rheological properties of the prepared MXene inks were studied in collaboration with Dr. Davis group from the Chemical Engineering deparmetn at Auburn University using a strain-controlled rotational rheometer (Physica MCR301, Anton Paar). Fixture geometries (made of stainless steel) used for testing were parallel-plates (25 mm diameter) and cone and plate (25 mm diameter, cone angle = 0.03 rad) to ensure there are no artifacts in the data due to testing geometry. After loading the rheometer with MXene ink at 25°C, subsequent test procedure was followed. For MXene ink, (1) wait 1 hour, (2) pre-shear at 0.01 s^{-1} for 1 hour, (3) wait 2 hours, (4) amplitude sweep (AS), (5) frequency sweep (FS) from 100 to 0.01 rad s^{-1}, (6, 7) repeated AS and FS one time each, (8) step rate at 0.01 s^{-1} for about 1 hour, (9) wait 20 min, (10) flow curve ~4 hours from 0.01 s^{-1} to 100 s^{-1}. For MXene+LFP ink, (1) wait 20 minutes, (2) pre-shear at 0.1 s^{-1} for 20 minutes, (3) wait 2 hours, (4) amplitude sweep, (5) frequency sweep from 100 to 0.1 rad s^{-1}, (6,7) repeated AS and FS one time each, (8) step rate at 0.1 s^{-1} for about 1 hour, (9) wait 20 min, (10) flow curve ~4 hours from 0.1 s^{-1} to 100 s^{-1}.

5.2.7 Electrochemical measurements

The fabricated LIBs electrochemical performances were tested using a LAND-CT and VMP3 potentiostat (Biologic, France). The galvanostatic charge-discharge tests were conducted in a voltage range of 3.8 V to 2.5 V versus Li/Li^+ for the cathode (MXene+LFP), and 2.5 V to 1 V versus Li/Li^+ for the anode (MXene+LTO). Lithium was used as the counter and reference electrode. The liquid electrolyte was 1 M LiPF6 in EC/DEC (1:1 by volume). The full cells were tested in a voltage range of 2.5 V to 1 V. All the cells were assembled in a high-purity argon-filled glovebox.

5.3 Results and Discussion

Figure 5-1 a-c shows the ink development and fabrication process used in this work. Briefly, $Ti_3C_2T_z$ dispersion was prepared by selectively removing the Al atoms layer from the parent MAX phase, Ti_3AlC_2, in HCl and LiF aqueous mixture for 24 h, as reported previously.[69] The mixture was then washed with DI water for several times (pH>5). The supernatant contained 2D MXene flakes with an average size of ~0.8 μm was collected and used to prepare the MXene-based inks (**Figure 5-1 d**). The MXene ink was prepared similarly to our previously published work.[121] Superabsorbent polymer (SAP) beads were used to remove water from the dispersion to achieve the desired concentrations. The prepared MXene ink was mixed with LFP and LTO nanoparticles to prepare the cathode and anode inks. As shown by SEM and energy dispersive analysis (EDS) in **Figure 5-1 c-f**, the MXene flakes and nanoparticles are uniformly mixed. Besides, the XRD data showed the MXene characteristic peak and a perfect fit with the standard orthorhombic LFP (JCPDS #40-1499) and cubic spinel LTO (JCPDS #49-0207), indicating the mixture did not affect the crystal structure of nanoparticles (**Figure 5-1 i**).

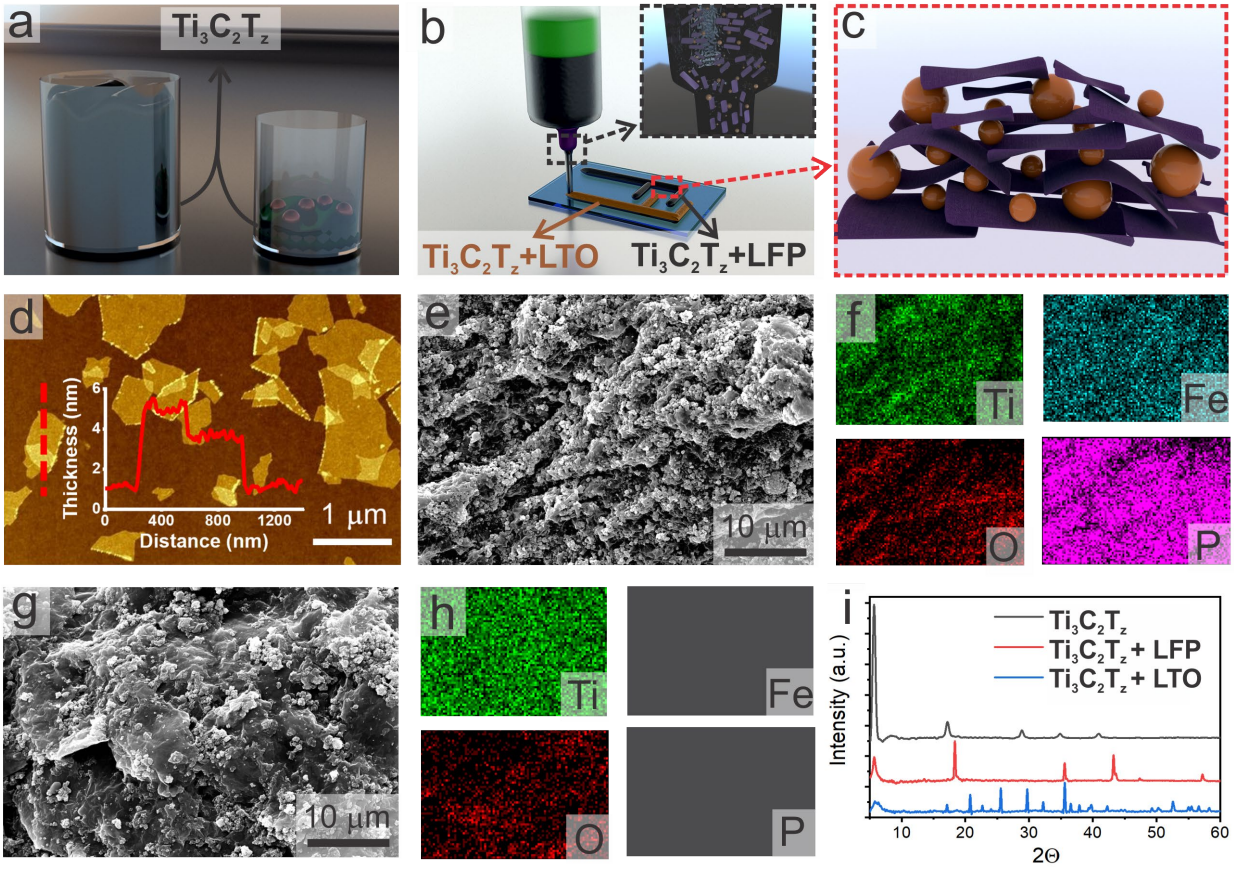

Figure 5.1. Mxene-based inks preparation and characterization. (a-c) schematic of ink development, printing and electrode structure, respectively. (d) AFM image of $Ti_3C_2T_z$ flakes showing the MXene dispersion consist of single layer flakes. (e, f) SEM images and EDS analysis of $Ti_3C_2T_z$+LFP ink showing the nanoparticles are uniformly mixed in the MXene dispersion. (g, h) SEM images and EDS analysis of $Ti_3C_2T_z$+LTO ink. (i) XRD of developed inks confirming there is no phase change after mixing.

We tried to develop an understanding on the effects of MXene sheet size, content, and nanoparticle addition on viscoelastic properties for 3D printable ink. The materials utilized in this work are ~0.8 µm long and 1.6 nm thickness 2D MXene sheets (aspect ratio L/D = 500), 200 nm spherical lithium iron phosphate (LFP), and sodium alginate (SA). Rheology was performed on MXene alone as well as multi-components MXene+LFP and MXene+LFP+SA to study the effects of size and shape on the final properties. This work is also compared with our previously published work[1] on MXene with small sheet sizes with dimensions of ~0.3 µm long and 1.6 nm thickness

(aspect ratio L/D = 187). **Figure 5-2** below shows an overlay of the rheology data. The steady shear viscosity curves in Figure 2a demonstrate shear-thinning behavior for all the dispersions, where higher viscosities are observed for the dispersions with large MX sheets. In the lower shear rate region for MXene+LFP+SA, the SA behavior dominates and represents what may be considered a transition region, which has also been observed in the literature with other multi-component dispersions composed of SA. **Figure 5-2 b** shows the oscillatory behavior for the materials, where the moduli G' (storage modulus) and G" (loss modulus). For all the dispersions, G' is relatively constant and G' >> G" across the entire frequency range is observed indicating more solid like than liquid like behavior. This in beneficial for the structure shape retention of the printed geometries. The G"/G' ratio indicates the developed ink has required liquid like behavior to encourage and allow interlayer adhesion. This observation is desirable for enabling interlayer adhesion to successfully 3D print multiple layers. However, the dispersion with SA illustrates an order of magnitude lower moduli than the other dispersions, which has been found to lack structural integrity when printing and decreases electrochemical performance. These results provide insight into the fundamental interactions at the nanoscale for further fabricating MXene-based lithium-ion battery electrodes, which serve as conductive alternatives to carbon-based materials that typically require additives for achieving enhanced electrochemical performance.

Precise deposition of MXene-based inks is of significance as the cell structure (architecture, line gap distancing, and electrode width) can considerably affect the ionic transport and, in turn, the electrochemical properties such as the power density and energy density of the fabricated device.[3,180,292] It is clear that studying the printability and the parameters that affect it will help designing more efficient architectures. To the best of our knowledge, there is no report on the effect of various printing parameters on the printing outcome and discussing the relationship

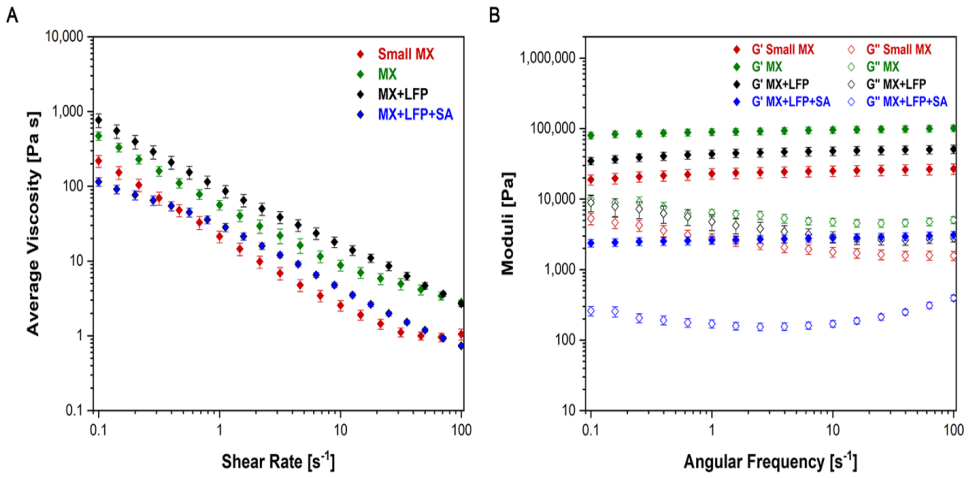

Figure 2. Rheology studies performed in collaboration with Dr. Davis group from the Chemical Engineering deparmetn at Auburn University on MX, MX+LFP, and MX+LFP+SA compared with small MX. a) Steady shear rheology indicates shear-thinning behavior and higher viscosities for the larger MX sheet dispersions. b) Oscillatory behavior illustrates larger G' than G" across entire frequency sweep for all the dispersions. Error bars are standard deviation.

for developed inks with application in energy storage. Most studies focus on the rheological properties and ink consistency. In addition to rheological properties, parameters such as printing pressure (P), printing speed (S_N), and the distance between the nozzle tip to the substrate (H) should be considered as they can significantly affect the printing outcome and resolution.

The applied pressure, P, can be considered the most important factor as it guarantees the inks' flow through the nozzle and significantly affects the printed line width (**Figure 5-3 a**). Mainly, the viscosity of the ink determines the threshold P (P_0) requires for printing. Higher P values than P_0 will result in higher ink volume extruded throughout the nozzle. Over high P would result in unstable extrusions, like jetting, resulting in difficulty controlling the extruded ink and low-quality print. To print high-quality geometries, increasing the pressure will eventually result

in increasing the printing speed. The printed lines are wider than the nozzle diameter due to the substrate properties and the ink expansion after extrusion.

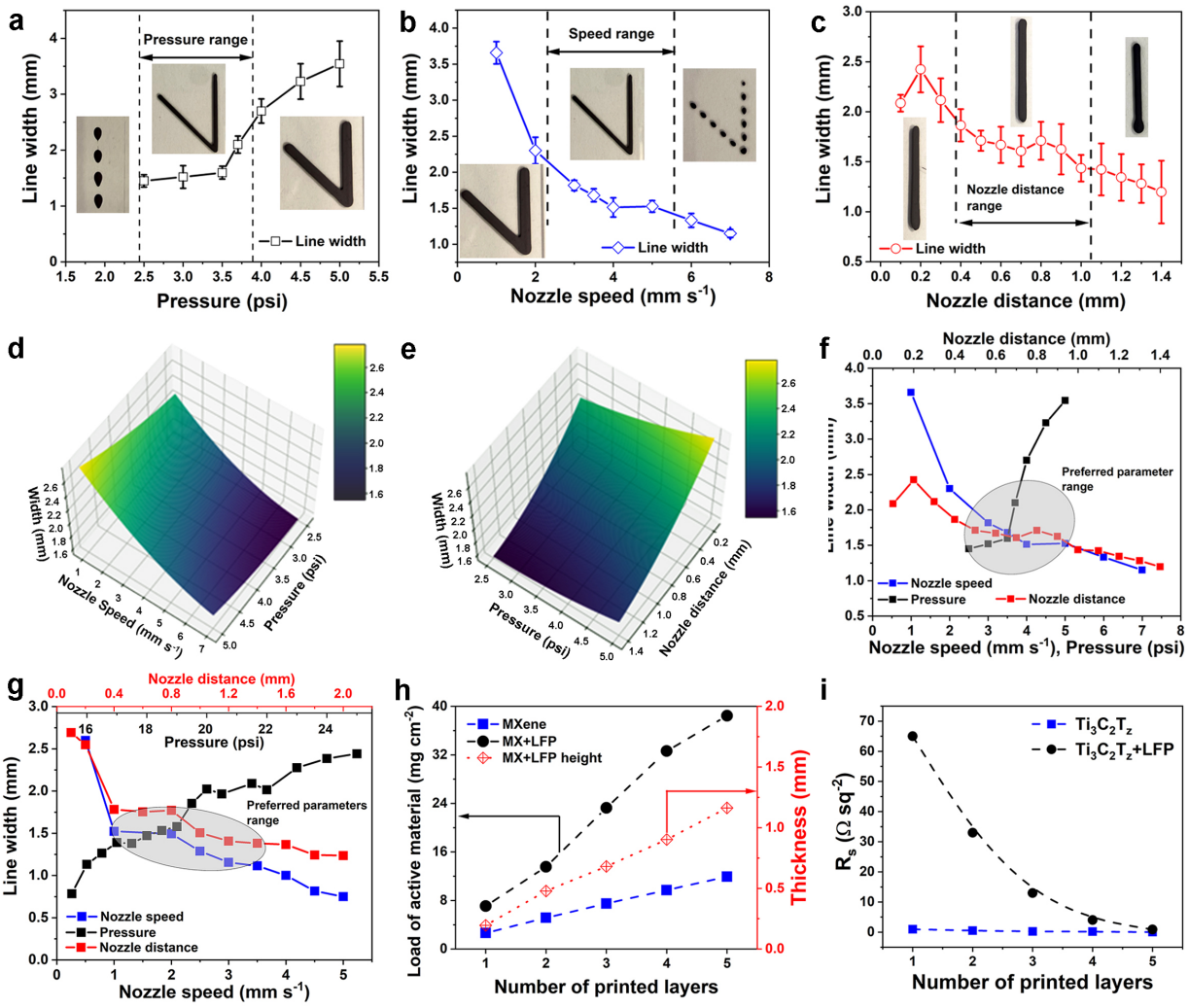

Figure 5-3. Effect of printing parameters on MXene-based inks printability. (a, b, c) effect of changing P (at constant S_N, H), S_N (at constant P, H), and H (at constant P, S_N) on pure MXene ink printed line width (gage 25). (d) Printability graph of MXene ink showing the preferred printing range. (e) Printability graph of MXene-LFP ink showing the preferred printing range. (f, g) Three-dimensional surface plots showing the relationship between the 3D printed pattern width with P-SN and P-H, respectively. (h) Load of active material and height of printed features as a function of the number of printed layers for MXene and MXene-LFP inks. (i) The sheet resistance, Rs, plotted as a function of the number of printed layers for MXene and MXene LFP inks.

To study the effect of P on printed line width, W, lines were printed at constant S_N, H, and nozzle size. **Figure 5-3 a** shows that increasing P would result in printing wider lines as higher ink volume is extruded through the nozzle. At low P, the extruded volume is not enough to form a continuous filament, while at high P significant increase in line width is observed (inset images in Figure 3a). After several experiments, for the pure MXene ink and the MXene composite inks used in this study, the P range was selected as 2.5-5 psi and 16-25 psi, respectively. The effect of S_N on W was further studied, as shown in Figure 3b.W decreases as S_N increases while other variables are kept constant (P= 3.5 psi, nozzle diameter= gage 25). Increasing the nozzle speed will lead to printing narrower lines until the lines become discontinued. Although P and S_N can be adjusted separately, it is essential to understand their relationship and match them to achieve high-quality prints.

H is another factor affecting the printing outcome. In addition to W, line length should be considered as another factor. If the distance is large, the ink tends to from droplet at the nozzle tip and in turn to have contact with the substrate, resulting in a shorter line than designed values. The

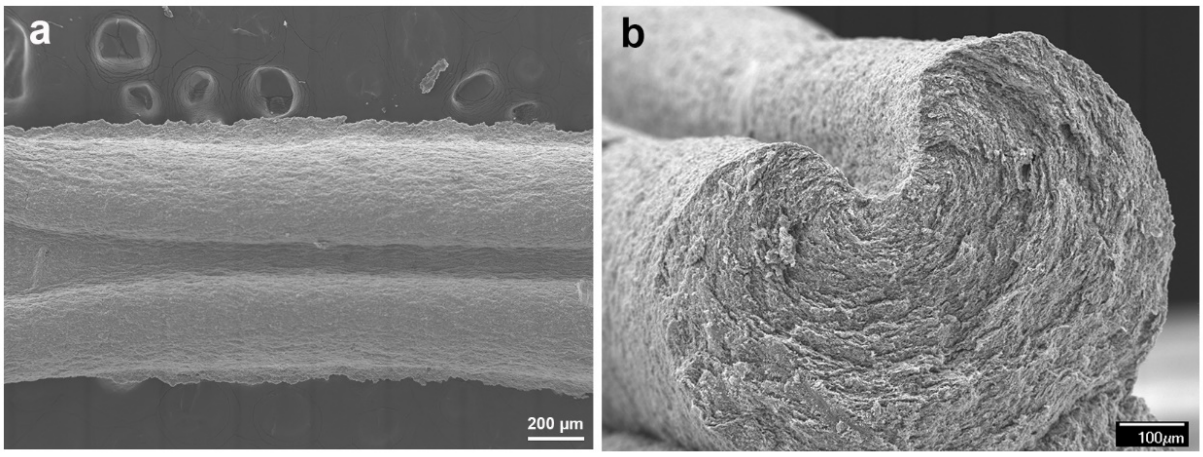

Figure 5-4. SEM images of printed MXene+LFP ink showing the effect of small H. (a) Top view image, (b) cross-section image.

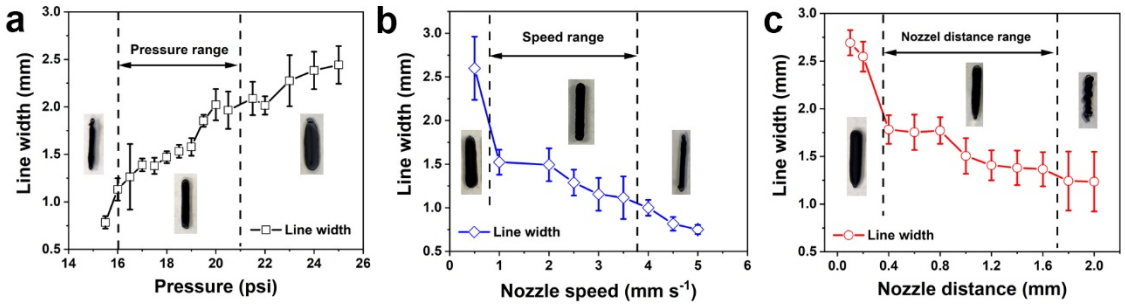

Figure 5-5. Effect of printing parameters on the line width. (a – c) Effect of P (at constant S_N=3.0 mm s^{-1}, H=0.8 mm), S_N (at constant P=19 psi, H=0.8 mm), and H (at constant P=19 psi, S_N=2.0 mm s^{-1}) on pure MXene ink printed line width (nozzle gauge 21).

ink accumulation on the nozzle tip causes over deposition at the beginning of the print, indicating the nozzle tip should be closer to the substrate. Small H would result in a U shape cross-section, as presented in **Figure 5-4**. The shorter the distance from the nozzle tip to the substrate, and the larger the nozzle diameter, the U shape cross-section is more noticeable. We believe that this is related to the fact that the extruded ink is pushed back by the substrate and the ink would eventually flow to the nozzle sides due to high surface tension of the developed ink. Similar test procedures were applied for MXene+LFP ink to study the effect of various parameters on printing outcome (**Figure 5-5**). The results showed similar behavior for both inks.

Finding the relationship between printing parameters and printed pattern is important to reproducibility and versatility.[293]. Machine learning methods can help understand important design parameters such as speed, nozzle distance, and pressure on 3D printed pattern specification. The developed model by machine learning allows a comprehensive understanding of complex behaviors among inter-related parameters, which are otherwise difficult to study experimentally [294,295]. In this study, different models such as polynomial, random forest, and artificial neural network were trained using 31 training samples, and 6 separate samples were used as test sets.

The testing samples were selected randomly to cover the entire range of input variables. To avoid the overfitting problem in the polynomial method, 5-fold cross-validation has been applied. Mean-square error (MSE) was used for the evaluation of model accuracy and validation.[296] There are many parameters in complicated methods which should be tuned by training data. The random forest and artificial neural network encountered the problem of overfitting due to a small training set. The following formula was used to evaluate MSE.

$$MSE = \frac{1}{m}\sum_{i=1}^{m}(y_i - \hat{y}_i)^2$$

The quadratic model was selected as the most accurate model (**Figure 5-6**). The validation and training set error for the quadratic model is close together, while with polynomial degree increase, the validation set accuracy decreases that prove the overfitting problem. 3D surface plots were used to identify the relationship between the 3D printed pattern width and the most determining parameters (**Figure 5-3 d and e**, and **Figure 5-7**). The presented 3D surface plots show that increasing the P and decreasing S_N or H would result in printing wider lines. S_N and H showed similar behavior, and increasing these parameters resulted in a decrease in W. Similar methodology were employed to study the relationship between different parameters and printing outcome for MXene+LFP ink (**Figure 5-7**). The developed quadratic model for MXene+LFP ink can predict the line width with over 90% accuracy for both tests and trained data (**Figure 5-6**).

Figure 3 e and f presents the effect of all the studied variables (P, S_N, and H) on W, in a single graph, for the MXene and the MXene+LFP inks, respectively. Similar to the 3D surface plots, S_N and H show a similar trend, while P shows a reverse relationship. Also, it can be concluded that H is as important as S_N, when W is the desired outcome. In addition, employing such a graph could be practical to define proper P, S_N, and H range and find a suitable printing condition. Further optimization of the parameters, printing sequence, and design can be employed to enhance the printing outcome.

It is important to define a window of printability employing rheological properties such as viscosity of the inks and printing parameters such as applied pressure. This window can be used to develop ink systems as it connects rheological properties to ink processability. The viscosity data can be employed to calculate the yield stress of the MXene-based inks. For a given nozzle diameter, the required pressure to trigger the ink extrusion process can be calculated with the yield

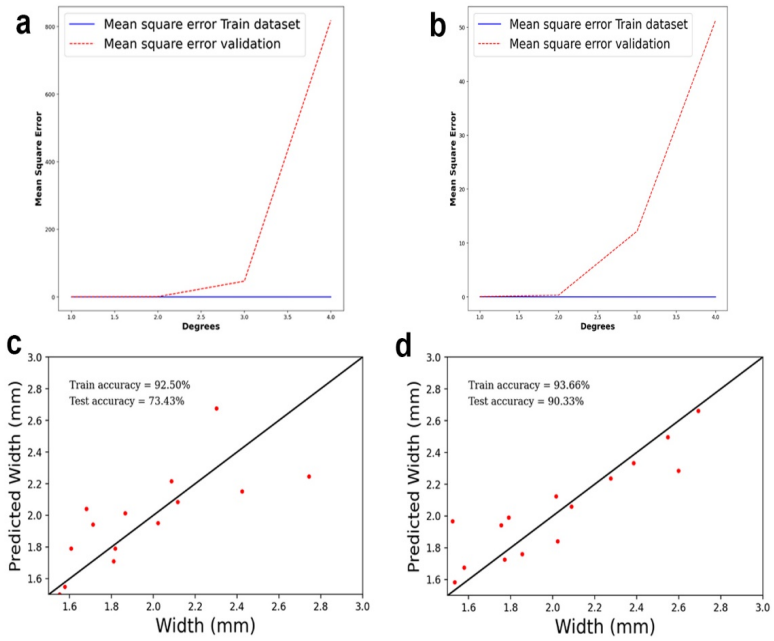

Figure 5-6. (a, b) show that quadratic model can provide the most accurate model for both inks. (c, d) Presents the parity plot for training data. The parity plot as well as test and train accuracies demonstrate the developed model can predict the width reasonably well.

stress. The yield stress supports the weight of the printed object. Simultaneously, the capillary forces lean the extremities of the printed structure in the direction of the center to minimize surface energy and turn the printed shape into a drop. Thus, the capillary forces which are related to dispersions surface tension should be considered in the formulation. It should be noted that the capillary forces should be strong enough to merge the printed layers to form a defect-free and space-filling structure.[210]

The next step to define printability is developing an image processing technique. This technique should measure different printing outputs, such as line width or area of the printed structure.[297] In the case of line width, the wettability of the developed inks and their substrate properties are essential. Employing a goniometer device to measure the contact angle and the width

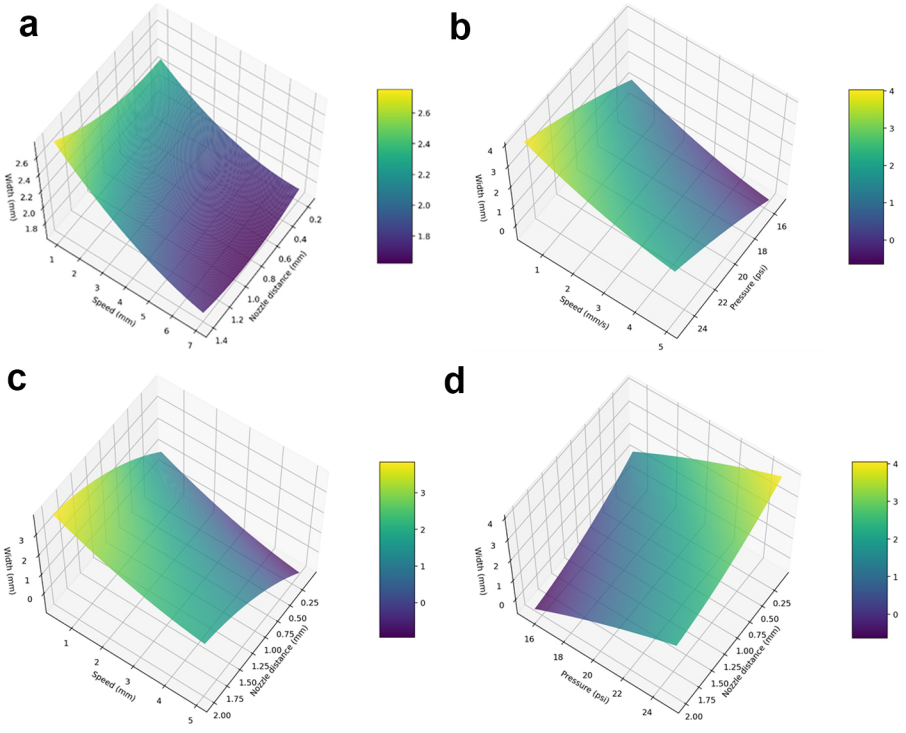

Figure 5-7. 3D surface plots showing the relation of different printing parameters. (a) Effect of SN and H on the line width printed with pure MXene ink while other parameters are kept constant. (b -d) Effect of P – SN, SN -H, and P-H on the printed line width using MXene+LFP ink.

of the deposited droplet in both static and dynamic methods.[210] These measurements would help to define the baseline of the printed structure line width. In the next step, lines and geometries can be printed at different printing conditions, followed by an image processing step to measure the printing outcome. Developing mathematical models using collected data and rheological properties would enable scientists to predict the printability of MXene-based dispersion based on their rheological properties.

The MXene-based composite inks were loaded in different syringes and used to print different shapes and geometries, including LIBs, with interdigital architecture by a robotic dispenser. The $Ti_3C_2T_z$-based composite inks viscoelastic properties resulted in a mechanically robust print. Multiple layers were printed in a layer-by-layer- fashion to achieve a high load of active material per area without collapse **(Figure 5-8**). To understand the relationship between the number of printed layers with line thickness, the load of active materials per area, and electron transfer properties of electrodes with 1-5 layers were evaluated (printed in a layer-by-layer fashion without drying time). The printed lines were functioning as current collectors and active material. Figure 3h shows the relationship between the number of printed layers and line thickness, and materials load. The results indicate a linear relationship between the thickness and load of material per area, with the number of printed layers contributing to the good viscoelastic properties of the MXene-based inks. The first printed filament showed exceptional shape retention upon subsequent printing layers on top of it and did not show buckling (**Figure 5-8**). The shear forces induced in the nozzle lead to the MXene flakes' alignment in the extrusion direction, similar to previously published works (**Figure 5-8**).[121] Printed MXene and MXene-LFP electrodes exhibit low sheet

resistance values (**Figure 5-3 i**). By increasing the electrodes' thickness, controlled by the number of the printed layers, the sheet resistance decreases similar to previous studies.[165]

The electrochemical properties of printed $Ti_3C_2T_z$-LFP and $Ti_3C_2T_z$-LTO half cells and full cells are presented in **Figure 5-9**. The electrochemical tests were performed in a house-made cell (**Figure 5-10**). The tested electrodes were connected to the electrochemical test station by applying a silver paste to the electrode tails, and 1M LiPF6 ethylene carbonate and diethyl carbonate was used as the electrolyte. The electrodes were dried at room temperature overnight, followed by 120°C drying for 48 hours to remove the remaining water in the structure. Lithium metal was used as the counter and reference electrode in half cells. The cells were rested for 24 hours before running the tests.

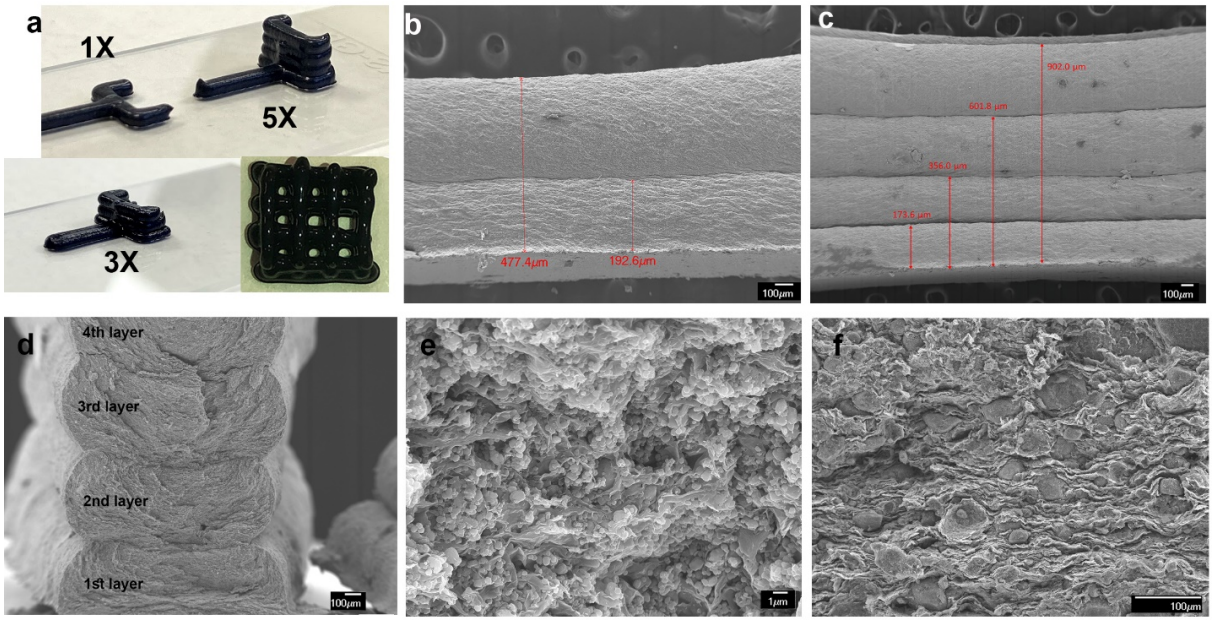

Figure 5-8. Optical and SEM images of printed lines and architectures using MX+LFP ink. (a) Optical image of 1,3, and 5 times printed electrode structures. (b, c) Side-view SEM images of 2 times and 4 times printed lines, respectively. (d) Cross-section SEM image of 4 layers of printed ink showing good mechanical stability of printed lines. (e, f) Cross-section SEM images of MXene+LFP and MXene+LTO composite electrodes at different magnifications.

Figure 5-9 a and b shows the charge and discharge curve of $Ti_3C_2T_z$-LFP and $Ti_3C_2T_z$-LTO electrodes at different current densities, respectively. The voltage hysteresis between the charge and discharge plateaus are ~ 0.1 V, similar to reported values for graphene oxide composite inks with LFP and LTO.[197] The voltage hysteresis stayed stable over cycling for $Ti_3C_2T_z$-LFP and $Ti_3C_2T_z$-LTO electrodes, indicating good electrical conductivity.[197] The $Ti_3C_2T_z$-LFP electrode showed the areal specific capacities of 5.05, 4.7, 3.9, 2.4, and 1.5 mAh cm^{-2} at specific current densities of 0.2, 0.3, 0.5, 1, and 2 mA cm^{-2}, respectively. Slightly higher capacities at charge were reported previously and could be related to increased length of the diffusion path and hosting of Li^+ ions in the MXene matrix, which increases the ionic diffusion resistivity.[197,298,299] The $Ti_3C_2T_z$-LTO electrode showed areal capacities of 5.8, 5.4, 5.0, 4.5, 3.6, and 2.1 mAh cm^{-2} at the at specific

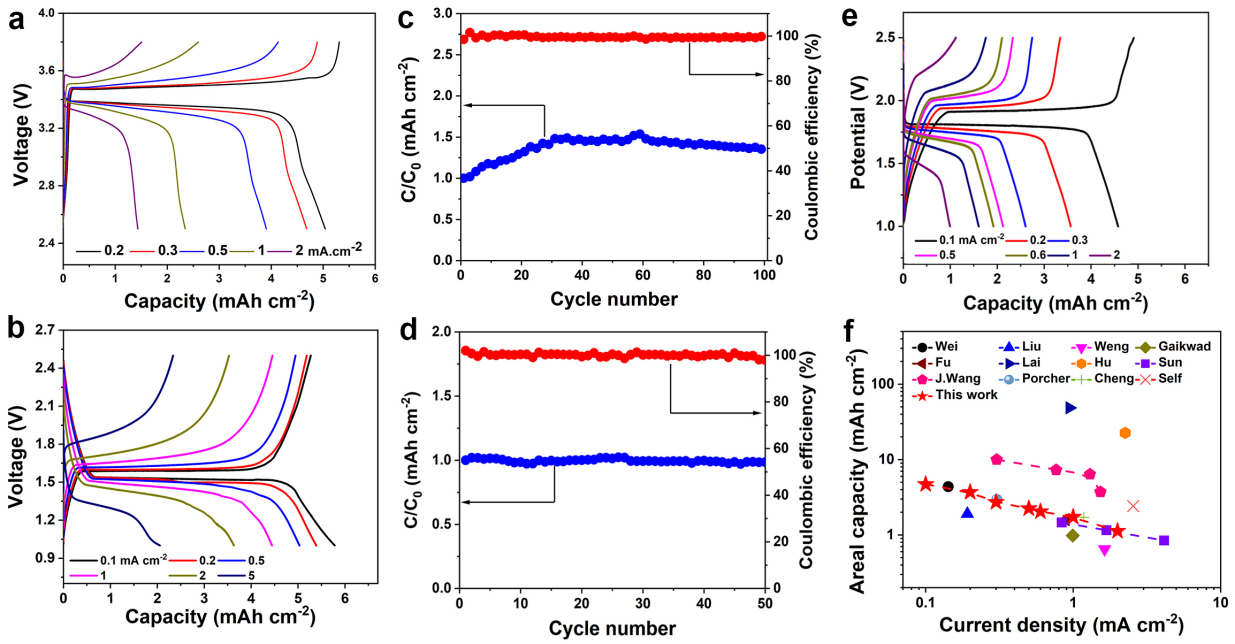

Figure 5-9. Electrochemical performance of 3D printed MXene-based electrodes. (a, b) Rate capability and voltage profile of $Ti_3C_2T_z$-LFP and $Ti_3C_2T_z$-LTO, respectively. (c, d) Cycling performance of 3D printed $Ti_3C_2T_z$-LFP and $Ti_3C_2T_z$-LTO electrodes. (e) voltage profile of 3D printed $Ti_3C_2T_z$-LFP and $Ti_3C_2T_z$-LTO full cell at different scan rates. (f) Ragone plot comparing areal capacity versus current density for the MXene-based 3D printed cell compared with previously reported values.

current densities of 0.1, 0.2, 0.5, 1, 2, and 5 mA cm^{-2}, respectively. The $Ti_3C_2T_z$-LTO half cells showed a plateau at ~1.55 V with stable performance over cycling (**Figure 5-9 c**). The MXene-based electrodes showed good cycling stability, as presented in Figure 4 c and d. The increase in capacity over cycling can be related to improved ionic accessibility and activation of the electrode over cycling (**Figure 5-9 c**). Both $Ti_3C_2T_z$-LFP and $Ti_3C_2T_z$-LTO half cells showed Coulombic efficiency of ~100% (**Figure 5-9 c and d right axes**).

Figure 5-9 e shows the electrochemical performance of a $Ti_3C_2T_z$-LFP cathode and $Ti_3C_2T_z$-LTO anode full cell at different scan rates. The $Ti_3C_2T_z$-LFP//$Ti_3C_2T_z$-LTO full cells showed the areal specific capacities of 4.7, 3.7, 2.7, 2.25, 2, 1.7, and 1.1 mAh cm^{-2} at specific current densities of 0.1, 0.2, 0.3, 0.5, 0.6, 1, and 2 mA cm^{-2}, respectively. The excellent electrochemical performance of fabricated devices can be attributed to the electrodes' porous structure, reduced agglomeration of both phases, and the 3D structure of the cell.[4] It worth mentioning that 3D printed full cells showed good cycling stability and Coulombic efficiency close to 100% (**Figure 5-10**). **Figure 5-9 f** compares the 3D printed MXene-based LIBs electrochemical

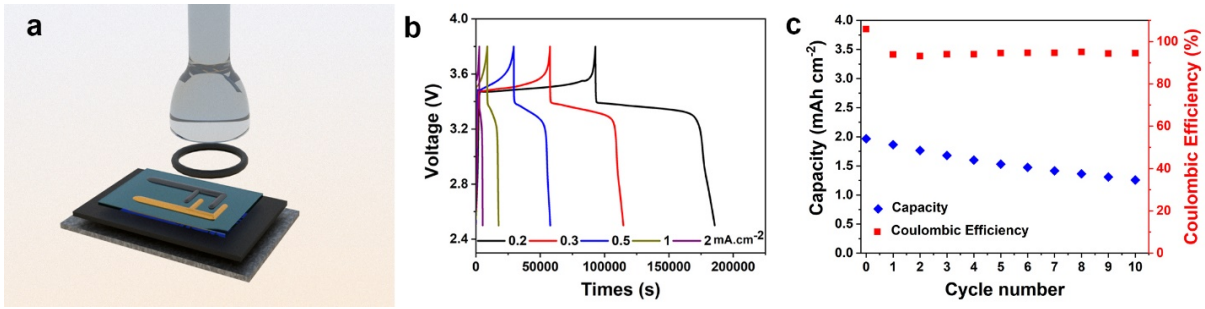

Figure 5-10. The electrochemical performance of 3D printed full cell. (a) Schematic of the glass cell used to evaluate the electrochemical performance of the fabricated 3D printed Li-ion microbatteries. (b) Voltage profile the tested full cell at different scan rates. (c) Cycling stability and Coulombic efficiency of fabricated 3D printed devices.

performance compared with some of the best-reposted values in the literature. Optimization in the ink formulation and cell geometry is required to further improve the capacity and rate capability of the 3D-printed cells to utilize their full potential.

In summary, the viscoelastic properties of MXene-based functional inks with favorable rheological properties to enable 3D print of the developed composite ink is demonstrated. MXene-based inks possess excellent viscoelastic properties and adjusting the printing parameters such as applied pressure and printing speed will lead to printing various geometries with high accuracy and high resolution, helping to assemble complex conductive 3D structures without post-processing. The effects of different printing parameters, their relation, and statistical models were studied and developed to better understand and predict the printing outcome. MXene-based inks are multifunctional materials with the potential to be employed as the conductive additive to 3D print LIBs with desired geometry. The 3D printed LIBs showed high areal capacitances of 4.7 mAh cm^{-2} at 0.1 mA cm^{-2} with excellent rate capability. The developed inks have the potential to be used in various applications and fields, including sensors and wearable electronics.

Chapter 6

Remaining challenges and future outlooks

Since their discovery in 2011, 2D MXenes have showing some exceptional physical and chemical properties in various applications such as energy storage and conversion, water treatment, electromagnetic interface shielding and many more. However, for each application, assembling the 2D MXene flakes in a structure which can deliver the specific properties is the key to taking full advantage of the properties of these materials. As explained above, for energy storage applications, preventing the restacking of 2D MXene flakes is a critical parameter to utilize the full electrochemical properties of these materials. The restacking of MXenes or other 2D materials can significantly reduce the active surface area and hinder electrolyte transport, diminishing the electrochemical reactions.[2,31,41,42,146,150,300] Therefore, developing fabrication methods that hinder restacking while providing the opportunity to engineering the structure of the fabricated electrodes to achieve a network of interconnected flakes with an abundance of porosity and an accessible interlayer spacing is crucial. As more research is performed on MXene-based dispersion and electrodes, our understanding on the properties of these materials is increasing which eventually will lead to the application of MXenes in various fields including energy storage and conversion.

During the course of my PhD, I developed additive-free MXene-based inks and showed that the MXene is a multifunctional material which can be served as the active materials or the conductive additive in various energy storage systems. Extrusion-based 3D printing and unidirectional freeze-casting methods was employed as simple, cost-effective, and straight forward fabrication methods to engineer electrode structures. Employing these fabrication methods and study parameters affecting fabrication condition could eventually result in better understanding on the structure – electrochemical property relationship. The research results presented in my dissertation and my published articles can be used by other researchers with interest in the application of 2D materials in different fields to develop the understanding on the fundamental properties of structure – property relationship and in turn engineering electrode structures to improve desire properties.

Based on my experience from working with MXene dispersions and formulating printable ink, I propose following research directions to push the boundaries of our understanding on MXene-based dispersion and their potential applications.

- Develop an understanding on MXene dispersion properties. For example, the effect of MXene flake size and concentration on the rheological properties of MXene-based dispersions.
- Develop mathematical models that connect rheological properties to printing condition and define a window of printability.
- Developing MXene-polymer composite inks and study their application in various fields such as energy storage and communication.
- Hybridizing MXenes with other electrochemically active nanomaterials to fabricate high-performance electrode materials. For example, heterostructures of MXene and 2D TMOs

can exploit the high specific capacitance of TMOs and the high electronic conductivity of MXenes.

References

(1) Beidaghi, M.; Gogotsi, Y. Capacitive Energy Storage in Micro-Scale Devices: Recent Advances in Design and Fabrication of Micro-Supercapacitors. *Energy & Environmental Science* **2014**, *7* (3), 867–884.

(2) Anasori, B.; Lukatskaya, M. R.; Gogotsi, Y. 2D Metal Carbides and Nitrides (MXenes) for Energy Storage. *Nature Reviews Materials* **2017**, *2* (2), 16098.

(3) Xiong, G.; Meng, C.; Reifenberger, R. G.; Irazoqui, P. P.; Fisher, T. S. A Review of Graphene-Based Electrochemical Microsupercapacitors. *Electroanalysis* **2014**, *26* (1), 30–51.

(4) Orangi, J.; Beidaghi, M. A Review of the Effects of Electrode Fabrication and Assembly Processes on the Structure and Electrochemical Performance of 2D MXenes. *Advanced Functional Materials* **2020**, 2005305.

(5) Novoselov, K. S.; Mishchenko, A.; Carvalho, A.; Neto, A. C. 2D Materials and van Der Waals Heterostructures. *Science* **2016**, *353* (6298), aac9439.

(6) Anasori, B.; Lukatskaya, M. R.; Gogotsi, Y. 2D Metal Carbides and Nitrides (MXenes) for Energy Storage. *Nature Reviews Materials* **2017**, *2* (2), 16098.

(7) Li, K.; Liang, M.; Wang, H.; Wang, X.; Huang, Y.; Coelho, J.; Pinilla, S.; Zhang, Y.; Qi, F.; Nicolosi, V. 3D MXene Architectures for Efficient Energy Storage and Conversion. *Advanced Functional Materials* **2020**, 2000842.

(8) Liu, C.; Li, F.; Ma, L.-P.; Cheng, H.-M. Advanced Materials for Energy Storage. *Advanced materials* **2010**, *22* (8), E28–E62.

(9) Aïssa, B.; Ali, A.; Mahmoud, K. A.; Haddad, T.; Nedil, M. Transport Properties of a Highly Conductive 2D Ti3C2Tx MXene/Graphene Composite. *Applied Physics Letters* **2016**, *109* (4), 043109.

(10) Naguib, M.; Mashtalir, O.; Carle, J.; Presser, V.; Lu, J.; Hultman, L.; Gogotsi, Y.; Barsoum, M. W. Two-Dimensional Transition Metal Carbides. *ACS nano* **2012**, *6* (2), 1322–1331.

(11) Podsiadlo, P.; Kaushik, A. K.; Arruda, E. M.; Waas, A. M.; Shim, B. S.; Xu, J.; Nandivada, H.; Pumplin, B. G.; Lahann, J.; Ramamoorthy, A. Ultrastrong and Stiff Layered Polymer Nanocomposites. *Science* **2007**, *318* (5847), 80–83.

(12) Lukatskaya, M. R.; Kota, S.; Lin, Z.; Zhao, M.-Q.; Shpigel, N.; Levi, M. D.; Halim, J.; Taberna, P.-L.; Barsoum, M. W.; Simon, P. Ultra-High-Rate Pseudocapacitive Energy Storage in Two-Dimensional Transition Metal Carbides. *Nature Energy* **2017**, *2* (8), 17105.

(13) Urbankowski, P.; Anasori, B.; Makaryan, T.; Er, D.; Kota, S.; Walsh, P. L.; Zhao, M.; Shenoy, V. B.; Barsoum, M. W.; Gogotsi, Y. Synthesis of Two-Dimensional Titanium Nitride Ti 4 N 3 (MXene). *Nanoscale* **2016**, *8* (22), 11385–11391.

(14) Kurtoglu, M.; Naguib, M.; Gogotsi, Y.; Barsoum, M. W. First Principles Study of Two-Dimensional Early Transition Metal Carbides. *Mrs Communications* **2012**, *2* (4), 133–137.

(15) Du, Y.-T.; Kan, X.; Yang, F.; Gan, L.-Y.; Schwingenschlögl, U. MXene/Graphene Heterostructures as High-Performance Electrodes for Li-Ion Batteries. *ACS Applied Materials & Interfaces* **2018**, *10* (38), 32867–32873. https://doi.org/10.1021/acsami.8b10729.

(16) Xie, X.; Zhao, M.-Q.; Anasori, B.; Maleski, K.; Ren, C. E.; Li, J.; Byles, B. W.; Pomerantseva, E.; Wang, G.; Gogotsi, Y. Porous Heterostructured MXene/Carbon Nanotube Composite Paper with High Volumetric Capacity for Sodium-Based Energy Storage Devices. *Nano Energy* **2016**, *26*, 513–523. https://doi.org/10.1016/j.nanoen.2016.06.005.

(17) Das, P.; Fu, Q.; Bao, X.; Wu, Z.-S. Recent Advances in the Preparation, Characterization, and Applications of Two-Dimensional Heterostructures for Energy Storage and Conversion. *Journal of Materials Chemistry A* **2018**, *6* (44), 21747–21784. https://doi.org/10.1039/C8TA04618B.

(18) Tan, C.; Cao, X.; Wu, X.-J.; He, Q.; Yang, J.; Zhang, X.; Chen, J.; Zhao, W.; Han, S.; Nam, G.-H. Recent Advances in Ultrathin Two-Dimensional Nanomaterials. *Chemical reviews* **2017**, *117* (9), 6225–6331.

(19) Butler, S. Z.; Hollen, S. M.; Cao, L.; Cui, Y.; Gupta, J. A.; Gutiérrez, H. R.; Heinz, T. F.; Hong, S. S.; Huang, J.; Ismach, A. F. Progress, Challenges, and Opportunities in Two-Dimensional Materials beyond Graphene. *ACS nano* **2013**, *7* (4), 2898–2926.

(20) Jung, S. M.; Jung, H. Y.; Dresselhaus, M. S.; Jung, Y. J.; Kong, J. A Facile Route for 3D Aerogels from Nanostructured 1D and 2D Materials. *Scientific reports* **2012**, *2*, 849.

(21) Mas-Balleste, R.; Gomez-Navarro, C.; Gomez-Herrero, J.; Zamora, F. 2D Materials: To Graphene and Beyond. *Nanoscale* **2011**, *3* (1), 20–30.

(22) Chang, J.; Jin, M.; Yao, F.; Kim, T. H.; Le, V. T.; Yue, H.; Gunes, F.; Li, B.; Ghosh, A.; Xie, S. Asymmetric Supercapacitors Based on Graphene/MnO2 Nanospheres and Graphene/MoO3 Nanosheets with High Energy Density. *Advanced Functional Materials* **2013**, *23* (40), 5074–5083.

(23) Hwang, C.; Chung, T.-L.; Sanders, E. A. Attitudes and Purchase Intentions for Smart Clothing: Examining US Consumers' Functional, Expressive, and Aesthetic Needs for Solar-Powered Clothing. *Clothing and Textiles Research Journal* **2016**, *34* (3), 207–222.

(24) Huang, Q.; Wang, D.; Zheng, Z. Textile-Based Electrochemical Energy Storage Devices. *Advanced Energy Materials* **2016**, *6* (22), 1600783.

(25) Eike, R. J.; Bakhshian, S. Review of Fashion, Technology and Health: Future Directions for the Apparel Industry. *Trends in Textile Engineering and Fashion Technology* **2018**, *4*, 1–4.

(26) Schubert, M. B.; Werner, J. H. Flexible Solar Cells for Clothing. *Materials today* **2006**, *9* (6), 42–50.

(27) Li, L.; Wu, Z.; Yuan, S.; Zhang, X.-B. Advances and Challenges for Flexible Energy Storage and Conversion Devices and Systems. *Energy & Environmental Science* **2014**, *7* (7), 2101–2122.

(28) Rakhi, R. B.; Chen, W.; Cha, D.; Alshareef, H. N. Nanostructured Ternary Electrodes for Energy-Storage Applications. *Advanced Energy Materials* **2012**, *2* (3), 381–389.

(29) Hu, Y.; Guan, C.; Feng, G.; Ke, Q.; Huang, X.; Wang, J. Flexible Asymmetric Supercapacitor Based on Structure-Optimized Mn3O4/Reduced Graphene Oxide Nanohybrid Paper with High Energy and Power Density. *Advanced Functional Materials* **2015**, *25* (47), 7291–7299.

(30) Lu, X.; Zhu, J.; Wu, W.; Zhang, B. Hierarchical Architecture of PANI@TiO2/Ti3C2Tx Ternary Composite Electrode for Enhanced Electrochemical Performance. *Electrochimica Acta* **2017**, *228*, 282–289. https://doi.org/10.1016/j.electacta.2017.01.025.

(31) Tian, W.; VahidMohammadi, A.; Wang, Z.; Ouyang, L.; Beidaghi, M.; Hamedi, M. M. Layer-by-Layer Self-Assembly of Pillared Two-Dimensional Multilayers. *Nature Communications* **2019**, *10* (1), 2558. https://doi.org/10.1038/s41467-019-10631-0.
(32) VahidMohammadi, A.; Hadjikhani, A.; Shahbazmohamadi, S.; Beidaghi, M. Two-Dimensional Vanadium Carbide (MXene) as a High-Capacity Cathode Material for Rechargeable Aluminum Batteries. *ACS nano* **2017**, *11* (11), 11135–11144.
(33) Mendoza-Sánchez, B.; Gogotsi, Y. Synthesis of Two-Dimensional Materials for Capacitive Energy Storage. *Advanced Materials* **2016**, *28* (29), 6104–6135.
(34) Coleman, J. N.; Lotya, M.; O'Neill, A.; Bergin, S. D.; King, P. J.; Khan, U.; Young, K.; Gaucher, A.; De, S.; Smith, R. J. Two-Dimensional Nanosheets Produced by Liquid Exfoliation of Layered Materials. *Science* **2011**, *331* (6017), 568–571.
(35) Min, Y.; Im, E.; Hwang, G.-T.; Kim, J.-W.; Ahn, C.-W.; Choi, J.-J.; Hahn, B.-D.; Choi, J.-H.; Yoon, W.-H.; Park, D.-S.; Hyun, D. C.; Moon, G. D. Heterostructures in Two-Dimensional Colloidal Metal Chalcogenides: Synthetic Fundamentals and Applications. *Nano Research* **2019**, 1–20.
(36) Wang, Q. H.; Kalantar-Zadeh, K.; Kis, A.; Coleman, J. N.; Strano, M. S. Electronics and Optoelectronics of Two-Dimensional Transition Metal Dichalcogenides. *Nature nanotechnology* **2012**, *7* (11), 699.
(37) Lukatskaya, M. R.; Mashtalir, O.; Ren, C. E.; Dall'Agnese, Y.; Rozier, P.; Taberna, P. L.; Naguib, M.; Simon, P.; Barsoum, M. W.; Gogotsi, Y. Cation Intercalation and High Volumetric Capacitance of Two-Dimensional Titanium Carbide. *Science* **2013**, *341* (6153), 1502–1505.
(38) Gao, G.; O'Mullane, A. P.; Du, A. 2D MXenes: A New Family of Promising Catalysts for the Hydrogen Evolution Reaction. *ACS Catalysis* **2016**, *7* (1), 494–500.
(39) Geng, D.; Zhao, X.; Chen, Z.; Sun, W.; Fu, W.; Chen, J.; Liu, W.; Zhou, W.; Loh, K. P. Direct Synthesis of Large-Area 2D Mo2C on in Situ Grown Graphene. *Advanced Materials* **2017**, *29* (35), 1700072.
(40) Guo, Z.; Zhou, J.; Zhu, L.; Sun, Z. MXene: A Promising Photocatalyst for Water Splitting. *Journal of Materials Chemistry A* **2016**, *4* (29), 11446–11452.
(41) VahidMohammadi, A.; Moncada, J.; Chen, H.; Kayali, E.; Orangi, J.; Carrero, C. A.; Beidaghi, M. Thick and Freestanding MXene/PANI Pseudocapacitive Electrodes with Ultrahigh Specific Capacitance. *Journal of Materials Chemistry A* **2018**, *6* (44), 22123–22133.
(42) Kayali, E.; VahidMohammadi, A.; Orangi, J.; Beidaghi, M. Controlling the Dimensions of 2D MXenes for Ultra-High-Rate Pseudocapacitive Energy Storage. *ACS applied materials & interfaces* **2018**, *10* (31), 25949–25954.
(43) Xie, Y.; Naguib, M.; Mochalin, V. N.; Barsoum, M. W.; Gogotsi, Y.; Yu, X.; Nam, K.-W.; Yang, X.-Q.; Kolesnikov, A. I.; Kent, P. R. Role of Surface Structure on Li-Ion Energy Storage Capacity of Two-Dimensional Transition-Metal Carbides. *Journal of the American Chemical Society* **2014**, *136* (17), 6385–6394.
(44) Ling, Z.; Ren, C. E.; Zhao, M.-Q.; Yang, J.; Giammarco, J. M.; Qiu, J.; Barsoum, M. W.; Gogotsi, Y. Flexible and Conductive MXene Films and Nanocomposites with High Capacitance. *Proceedings of the National Academy of Sciences* **2014**, *111* (47), 16676–16681.

(45) Zhan, C.; Naguib, M.; Lukatskaya, M.; Kent, P. R.; Gogotsi, Y.; Jiang, D. Understanding the MXene Pseudocapacitance. *The journal of physical chemistry letters* **2018**, *9* (6), 1223–1228.
(46) Lipatov, A.; Alhabeb, M.; Lukatskaya, M. R.; Boson, A.; Gogotsi, Y.; Sinitskii, A. Effect of Synthesis on Quality, Electronic Properties and Environmental Stability of Individual Monolayer Ti3C2 MXene Flakes. *Advanced Electronic Materials* **2016**, *2* (12), 1600255.
(47) Mu, X.; Wang, D.; Du, F.; Chen, G.; Wang, C.; Wei, Y.; Gogotsi, Y.; Gao, Y.; Dall'Agnese, Y. Revealing the Pseudo-Intercalation Charge Storage Mechanism of MXenes in Acidic Electrolyte. *Advanced Functional Materials* **2019**, *29* (29), 1902953.
(48) Hu, M.; Li, Z.; Hu, T.; Zhu, S.; Zhang, C.; Wang, X. High-Capacitance Mechanism for Ti3C2 T x MXene by in Situ Electrochemical Raman Spectroscopy Investigation. *ACS nano* **2016**, *10* (12), 11344–11350.
(49) Lin, Z.; Rozier, P.; Duployer, B.; Taberna, P.-L.; Anasori, B.; Gogotsi, Y.; Simon, P. Electrochemical and In-Situ X-Ray Diffraction Studies of Ti3C2Tx MXene in Ionic Liquid Electrolyte. *Electrochemistry Communications* **2016**, *72*, 50–53.
(50) Wang, X.; Mathis, T. S.; Li, K.; Lin, Z.; Vlcek, L.; Torita, T.; Osti, N. C.; Hatter, C.; Urbankowski, P.; Sarycheva, A. Influences from Solvents on Charge Storage in Titanium Carbide MXenes. *Nature Energy* **2019**, *4* (3), 241–248.
(51) Cheng, R.; Hu, T.; Zhang, H.; Wang, C.; Hu, M.; Yang, J.; Cui, C.; Guang, T.; Li, C.; Shi, C. Understanding the Lithium Storage Mechanism of Ti3C2T x MXene. *The Journal of Physical Chemistry C* **2018**, *123* (2), 1099–1109.
(52) Pomerantseva, E.; Gogotsi, Y. Two-Dimensional Heterostructures for Energy Storage. *Nature Energy* **2017**, *2* (7).
(53) Liu, Y.; Weiss, N. O.; Duan, X.; Cheng, H.-C.; Huang, Y.; Duan, X. Van Der Waals Heterostructures and Devices. *Nature Reviews Materials* **2016**, *1* (9), 1–17.
(54) Shen, J.; Zhu, Y.; Jiang, H.; Li, C. 2D Nanosheets-Based Novel Architectures: Synthesis, Assembly and Applications. *Nano Today* **2016**, *11* (4), 483–520. https://doi.org/10.1016/j.nantod.2016.07.005.
(55) Tan, C.; Chen, J.; Wu, X.-J.; Zhang, H. Epitaxial Growth of Hybrid Nanostructures. *Nature Reviews Materials* **2018**, *3* (2), 17089.
(56) Byeon, A.; Glushenkov, A. M.; Anasori, B.; Urbankowski, P.; Li, J.; Byles, B. W.; Blake, B.; Van Aken, K. L.; Kota, S.; Pomerantseva, E.; Lee, J. W.; Chen, Y.; Gogotsi, Y. Lithium-Ion Capacitors with 2D Nb 2 CT x (MXene) – Carbon Nanotube Electrodes. *Journal of Power Sources* **2016**, *326*, 686–694. https://doi.org/10.1016/j.jpowsour.2016.03.066.
(57) Navarro-Suárez, A. M.; Maleski, K.; Makaryan, T.; Yan, J.; Anasori, B.; Gogotsi, Y. 2D Titanium Carbide/Reduced Graphene Oxide Heterostructures for Supercapacitor Applications. *Batteries & Supercaps* **2018**, *1* (1), 33–38. https://doi.org/10.1002/batt.201800014.
(58) Ahmed, B.; Anjum, D. H.; Gogotsi, Y.; Alshareef, H. N. Atomic Layer Deposition of SnO 2 on MXene for Li-Ion Battery Anodes. *Nano Energy* **2017**, *34*, 249–256. https://doi.org/10.1016/j.nanoen.2017.02.043.
(59) Fu, Q.; Wang, X.; Zhang, N.; Wen, J.; Li, L.; Gao, H.; Zhang, X. Self-Assembled Ti 3 C 2 T x /SCNT Composite Electrode with Improved Electrochemical Performance for Supercapacitor. *Journal of Colloid and Interface Science* **2018**, *511*, 128–134. https://doi.org/10.1016/j.jcis.2017.09.104.

(60) Bao, W.; Xie, X.; Xu, J.; Guo, X.; Song, J.; Wu, W.; Su, D.; Wang, G. Confined Sulfur in 3 D MXene/Reduced Graphene Oxide Hybrid Nanosheets for Lithium-Sulfur Battery. *Chemistry - A European Journal* **2017**, *23* (51), 12613–12619. https://doi.org/10.1002/chem.201702387.

(61) Couly, C.; Alhabeb, M.; Van Aken, K. L.; Kurra, N.; Gomes, L.; Navarro-Suárez, A. M.; Anasori, B.; Alshareef, H. N.; Gogotsi, Y. Asymmetric Flexible MXene-Reduced Graphene Oxide Micro-Supercapacitor. *Advanced Electronic Materials* **2018**, *4* (1), 1700339.

(62) Fan, Z.; Wang, Y.; Xie, Z.; Wang, D.; Yuan, Y.; Kang, H.; Su, B.; Cheng, Z.; Liu, Y. Modified MXene/Holey Graphene Films for Advanced Supercapacitor Electrodes with Superior Energy Storage. *Advanced Science* **2018**, *5* (10), 1800750. https://doi.org/10.1002/advs.201800750.

(63) Fu, J.; Li, L.; Yun, J. M.; Lee, D.; Ryu, B. K.; Kim, K. H. Two-Dimensional Titanium Carbide (MXene)-Wrapped Sisal-Like NiCo2S4 as Positive Electrode for High-Performance Hybrid Pouch-Type Asymmetric Supercapacitor. *Chemical Engineering Journal* **2019**, *375*, 121939. https://doi.org/10.1016/j.cej.2019.121939.

(64) Li, X.; Zhu, J.; Fang, Y.; Lv, W.; Wang, F.; Liu, Y.; Liu, H. Hydrothermal Preparation of CoO/Ti3C2 Composite Material for Lithium-Ion Batteries with Enhanced Electrochemical Performance. *Journal of Electroanalytical Chemistry* **2018**, *817*, 1–8. https://doi.org/10.1016/j.jelechem.2018.03.031.

(65) Liu, W.; Wang, Z.; Su, Y.; Li, Q.; Zhao, Z.; Geng, F. Molecularly Stacking Manganese Dioxide/Titanium Carbide Sheets to Produce Highly Flexible and Conductive Film Electrodes with Improved Pseudocapacitive Performances. *Advanced Energy Materials* **2017**, *7* (22), 1602834. https://doi.org/10.1002/aenm.201602834.

(66) Ma, Z.; Zhou, X.; Deng, W.; Lei, D.; Liu, Z. 3D Porous MXene (Ti_3C_2)/Reduced Graphene Oxide Hybrid Films for Advanced Lithium Storage. *ACS Applied Materials & Interfaces* **2018**, *10* (4), 3634–3643. https://doi.org/10.1021/acsami.7b17386.

(67) Shao, W.; Tebyetekerwa, M.; Marriam, I.; Li, W.; Wu, Y.; Peng, S.; Ramakrishna, S.; Yang, S.; Zhu, M. Polyester@MXene Nanofibers-Based Yarn Electrodes. *Journal of Power Sources* **2018**, *396*, 683–690. https://doi.org/10.1016/j.jpowsour.2018.06.084.

(68) Wang, J.; Dong, S.; Li, H.; Chen, Z.; Jiang, S.; Wu, L.; Zhang, X. Facile Synthesis of Layered Li4Ti5O12-Ti3C2Tx (MXene) Composite for High-Performance Lithium Ion Battery. *Journal of Electroanalytical Chemistry* **2018**, *810*, 27–33. https://doi.org/10.1016/j.jelechem.2017.12.079.

(69) Alhabeb, M.; Maleski, K.; Anasori, B.; Lelyukh, P.; Clark, L.; Sin, S.; Gogotsi, Y. Guidelines for Synthesis and Processing of Two-Dimensional Titanium Carbide (Ti3C2T x MXene). *Chemistry of Materials* **2017**, *29* (18), 7633–7644.

(70) Yan, J.; Wang, Q.; Wei, T.; Fan, Z. Recent Advances in Design and Fabrication of Electrochemical Supercapacitors with High Energy Densities. *Advanced Energy Materials* **2014**, *4* (4), 1300816.

(71) Ghidiu, M.; Lukatskaya, M. R.; Zhao, M.-Q.; Gogotsi, Y.; Barsoum, M. W. Conductive Two-Dimensional Titanium Carbide 'Clay'with High Volumetric Capacitance. *Nature* **2014**, *516* (7529), 78.

(72) Maleski, K.; Ren, C. E.; Zhao, M.-Q.; Anasori, B.; Gogotsi, Y. Size-Dependent Physical and Electrochemical Properties of Two-Dimensional MXene Flakes. *ACS applied materials & interfaces* **2018**, *10* (29), 24491–24498.

(73) Naguib, M.; Gogotsi, Y. Synthesis of Two-Dimensional Materials by Selective Extraction. *Accounts of Chemical Research* **2015**, *48* (1), 128–135. https://doi.org/10.1021/ar500346b.
(74) Zhang, T.; Pan, L.; Tang, H.; Du, F.; Guo, Y.; Qiu, T.; Yang, J. Synthesis of Two-Dimensional Ti3C2Tx MXene Using HCl+ LiF Etchant: Enhanced Exfoliation and Delamination. *Journal of Alloys and Compounds* **2017**, *695*, 818–826.
(75) Malaki, M.; Maleki, A.; Varma, R. S. MXenes and Ultrasonication. *Journal of Materials Chemistry A* **2019**, *7* (18), 10843–10857.
(76) Naguib, M.; Unocic, R. R.; Armstrong, B. L.; Nanda, J. Large-Scale Delamination of Multi-Layers Transition Metal Carbides and Carbonitrides "MXenes." *Dalton transactions* **2015**, *44* (20), 9353–9358.
(77) Halim, J.; Cook, K. M.; Eklund, P.; Rosen, J.; Barsoum, M. W. XPS of Cold Pressed Multilayered and Freestanding Delaminated 2D Thin Films of Mo2TiC2Tz and Mo2Ti2C3Tz (MXenes). *Applied Surface Science* **2019**, *494*, 1138–1147.
(78) Khazaei, M.; Ranjbar, A.; Arai, M.; Yunoki, S. Topological Insulators in the Ordered Double Transition Metals M 2′ M ″C 2 MXenes (M′= Mo, W; M ″= Ti, Zr, Hf). *Physical Review B* **2016**, *94* (12), 125152.
(79) Seh, Z. W.; Fredrickson, K. D.; Anasori, B.; Kibsgaard, J.; Strickler, A. L.; Lukatskaya, M. R.; Gogotsi, Y.; Jaramillo, T. F.; Vojvodic, A. Two-Dimensional Molybdenum Carbide (MXene) as an Efficient Electrocatalyst for Hydrogen Evolution. *ACS Energy Letters* **2016**, *1* (3), 589–594.
(80) Ng, V. M. H.; Huang, H.; Zhou, K.; Lee, P. S.; Que, W.; Xu, J. Z.; Kong, L. B. Recent Progress in Layered Transition Metal Carbides and/or Nitrides (MXenes) and Their Composites: Synthesis and Applications. *Journal of Materials Chemistry A* **2017**, *5* (7), 3039–3068.
(81) Li, G.; Tan, L.; zhang, Y.; Wu, B.; Li, L. Highly Efficiently Delaminated Single-Layered MXene Nanosheets with Large Lateral Size. *Langmuir* **2017**, *33* (36), 9000–9006. https://doi.org/10.1021/acs.langmuir.7b01339.
(82) Takemoto, S.; Hattori, M.; Yoshinari, M.; Kawada, E.; Oda, Y. Corrosion Behavior and Surface Characterization of Titanium in Solution Containing Fluoride and Albumin. *Biomaterials* **2005**, *26* (8), 829–837.
(83) Xie, X.; Xue, Y.; Li, L.; Chen, S.; Nie, Y.; Ding, W.; Wei, Z. Surface Al Leached Ti 3 AlC 2 as a Substitute for Carbon for Use as a Catalyst Support in a Harsh Corrosive Electrochemical System. *Nanoscale* **2014**, *6* (19), 11035–11040.
(84) Li, T.; Yao, L.; Liu, Q.; Gu, J.; Luo, R.; Li, J.; Yan, X.; Wang, W.; Liu, P.; Chen, B. Fluorine-Free Synthesis of High-Purity Ti3C2Tx (T= OH, O) via Alkali Treatment. *Angewandte Chemie International Edition* **2018**, *57* (21), 6115–6119.
(85) Mei, J.; Ayoko, G. A.; Hu, C.; Bell, J. M.; Sun, Z. Two-Dimensional Fluorine-Free Mesoporous Mo2C MXene via UV-Induced Selective Etching of Mo2Ga2C for Energy Storage. *Sustainable Materials and Technologies* **2020**, *25*, e00156.
(86) Yu, X.; Cai, X.; Cui, H.; Lee, S.-W.; Yu, X.-F.; Liu, B. Fluorine-Free Preparation of Titanium Carbide MXene Quantum Dots with High near-Infrared Photothermal Performances for Cancer Therapy. *Nanoscale* **2017**, *9* (45), 17859–17864.
(87) Yang, S.; Zhang, P.; Wang, F.; Ricciardulli, A. G.; Lohe, M. R.; Blom, P. W.; Feng, X. Fluoride-Free Synthesis of Two-Dimensional Titanium Carbide (MXene) Using A Binary Aqueous System. *Angewandte Chemie* **2018**, *130* (47), 15717–15721.

(88) Li, Y.; Shao, H.; Lin, Z.; Lu, J.; Liu, L.; Duployer, B.; Persson, P. O.; Eklund, P.; Hultman, L.; Li, M. A General Lewis Acidic Etching Route for Preparing MXenes with Enhanced Electrochemical Performance in Non-Aqueous Electrolyte. *Nature Materials* **2020**, 1–6.
(89) Pang, S.-Y.; Wong, Y.-T.; Yuan, S.; Liu, Y.; Tsang, M.-K.; Yang, Z.; Huang, H.; Wong, W.-T.; Hao, J. Universal Strategy for HF-Free Facile and Rapid Synthesis of Two-Dimensional MXenes as Multifunctional Energy Materials. *Journal of the American Chemical Society* **2019**, *141* (24), 9610–9616.
(90) Wang, J.; Tang, J.; Ding, B.; Malgras, V.; Chang, Z.; Hao, X.; Wang, Y.; Dou, H.; Zhang, X.; Yamauchi, Y. Hierarchical Porous Carbons with Layer-by-Layer Motif Architectures from Confined Soft-Template Self-Assembly in Layered Materials. *Nature Communications* **2017**, *8* (1), 15717. https://doi.org/10.1038/ncomms15717.
(91) Dall'Agnese, Y.; Lukatskaya, M. R.; Cook, K. M.; Taberna, P.-L.; Gogotsi, Y.; Simon, P. High Capacitance of Surface-Modified 2D Titanium Carbide in Acidic Electrolyte. *Electrochemistry Communications* **2014**, *48*, 118–122.
(92) Wang, H.; Wu, Y.; Zhang, J.; Li, G.; Huang, H.; Zhang, X.; Jiang, Q. Enhancement of the Electrical Properties of MXene Ti3C2 Nanosheets by Post-Treatments of Alkalization and Calcination. *Materials Letters* **2015**, *160*, 537–540.
(93) Wen, Y.; Rufford, T. E.; Chen, X.; Li, N.; Lyu, M.; Dai, L.; Wang, L. Nitrogen-Doped Ti3C2Tx MXene Electrodes for High-Performance Supercapacitors. *Nano Energy* **2017**, *38*, 368–376.
(94) Lian, P.; Dong, Y.; Wu, Z.-S.; Zheng, S.; Wang, X.; Wang, S.; Sun, C.; Qin, J.; Shi, X.; Bao, X. Alkalized Ti3C2 MXene Nanoribbons with Expanded Interlayer Spacing for High-Capacity Sodium and Potassium Ion Batteries. *Nano Energy* **2017**, *40*, 1–8.
(95) Chen, X.; Zhu, Y.; Zhang, M.; Sui, J.; Peng, W.; Li, Y.; Zhang, G.; Zhang, F.; Fan, X. N-Butyllithium-Treated Ti3C2T x MXene with Excellent Pseudocapacitor Performance. *ACS nano* **2019**, *13* (8), 9449–9456.
(96) Sun, S.; Liao, C.; Hafez, A. M.; Zhu, H.; Wu, S. Two-Dimensional MXenes for Energy Storage. *Chemical Engineering Journal* **2018**, *338*, 27–45.
(97) Jun, B.-M.; Kim, S.; Heo, J.; Park, C. M.; Her, N.; Jang, M.; Huang, Y.; Han, J.; Yoon, Y. Review of MXenes as New Nanomaterials for Energy Storage/Delivery and Selected Environmental Applications. *Nano Research* **2019**, *12* (3), 471–487.
(98) Yang, J.; Bao, W.; Jaumaux, P.; Zhang, S.; Wang, C.; Wang, G. MXene-Based Composites: Synthesis and Applications in Rechargeable Batteries and Supercapacitors. *Advanced Materials Interfaces* **2019**, *6* (8), 1802004.
(99) Dong, Y.; Shi, H.; Wu, Z.-S. Recent Advances and Promise of MXene-Based Nanostructures for High-Performance Metal Ion Batteries. *Advanced Functional Materials* **2020**, 2000706.
(100) Zheng, R.; Wu, L.; Zhao, J.; Zhu, C.; Gao, H. Ti3C2T X-Based Electrodes with Enhanced Pseudocapacitance for High-Performance Lithium-Ion Batteries. *Nano* **2020**, *15* (04), 2050051.
(101) Liu, J.; Zhang, A.; Liu, R.; Tian, J.; Huang, W. MXene-Based Nanocomposites for Electrochemical Energy Conversion and Storage Applications. *Chemistry–A European Journal* **2020**.
(102) Kötz, R.; Carlen, M. Principles and Applications of Electrochemical Capacitors. *Electrochimica acta* **2000**, *45* (15–16), 2483–2498.

(103) Zhang, L. L.; Zhou, R.; Zhao, X. S. Graphene-Based Materials as Supercapacitor Electrodes. *Journal of Materials Chemistry* **2010**, *20* (29), 5983–5992.
(104) Gao, H.-L.; Xu, L.; Long, F.; Pan, Z.; Du, Y.-X.; Lu, Y.; Ge, J.; Yu, S.-H. Macroscopic Free-Standing Hierarchical 3D Architectures Assembled from Silver Nanowires by Ice Templating. *Angewandte Chemie International Edition* **2014**, *53* (18), 4561–4566.
(105) Tian, Y.; Yang, C.; Que, W.; He, Y.; Liu, X.; Luo, Y.; Yin, X.; Kong, L. B. Ni Foam Supported Quasi-Core-Shell Structure of Ultrathin Ti 3 C 2 Nanosheets through Electrostatic Layer-by-Layer Self-Assembly as High Rate-Performance Electrodes of Supercapacitors. *Journal of Power Sources* **2017**, *369*, 78–86. https://doi.org/10.1016/j.jpowsour.2017.09.085.
(106) Tang, H.; Hu, Q.; Zheng, M.; Chi, Y.; Qin, X.; Pang, H.; Xu, Q. MXene–2D Layered Electrode Materials for Energy Storage. *Progress in Natural Science: Materials International* **2018**, *28* (2), 133–147. https://doi.org/10.1016/j.pnsc.2018.03.003.
(107) Zhao, M.-Q.; Xie, X.; Ren, C. E.; Makaryan, T.; Anasori, B.; Wang, G.; Gogotsi, Y. Hollow MXene Spheres and 3D Macroporous MXene Frameworks for Na-Ion Storage. *Advanced Materials* **2017**, *29* (37), 1702410.
(108) Xia, Y.; Mathis, T. S.; Zhao, M.-Q.; Anasori, B.; Dang, A.; Zhou, Z.; Cho, H.; Gogotsi, Y.; Yang, S. Thickness-Independent Capacitance of Vertically Aligned Liquid-Crystalline MXenes. *Nature* **2018**, *557* (7705), 409–412.
(109) Demiroglu, I.; Peeters, F. M.; Gülseren, O.; Çakır, D.; Sevik, C. Alkali Metal Intercalation in MXene/Graphene Heterostructures: A New Platform for Ion Battery Applications. *The Journal of Physical Chemistry Letters* **2019**, *10* (4), 727–734. https://doi.org/10.1021/acs.jpclett.8b03056.
(110) Wu, Y.; Nie, P.; Wu, L.; Dou, H.; Zhang, X. 2D MXene/SnS2 Composites as High-Performance Anodes for Sodium Ion Batteries. *Chemical Engineering Journal* **2018**, *334*, 932–938.
(111) Wang, L.; Qiu, H.; Song, P.; Zhang, Y.; Lu, Y.; Liang, C.; Kong, J.; Chen, L.; Gu, J. 3D Ti3C2Tx MXene/C Hybrid Foam/Epoxy Nanocomposites with Superior Electromagnetic Interference Shielding Performances and Robust Mechanical Properties. *Composites Part A: Applied Science and Manufacturing* **2019**, *123*, 293–300. https://doi.org/10.1016/j.compositesa.2019.05.030.
(112) Ogihara, N.; Ozawa, Y.; Hiruta, O. A Self-Assembled Intercalated Metal–Organic Framework Electrode with Outstanding Area Capacity for High Volumetric Energy Asymmetric Capacitors. *Journal of Materials Chemistry A* **2016**, *4* (9), 3398–3405. https://doi.org/10.1039/C5TA09559J.
(113) Zheng, J.; Diao, J.; Jin, Y.; Ding, A.; Wang, B.; Wu, L.; Weng, B.; Chen, J. An Inkjet Printed Ti3C2-GO Electrode for the Electrochemical Sensing of Hydrogen Peroxide. *Journal of The Electrochemical Society* **2018**, *165* (5), B227–B231.
(114) Sun, R.; Zhang, H.-B.; Liu, J.; Xie, X.; Yang, R.; Li, Y.; Hong, S.; Yu, Z.-Z. Highly Conductive Transition Metal Carbide/Carbonitride (MXene)@ Polystyrene Nanocomposites Fabricated by Electrostatic Assembly for Highly Efficient Electromagnetic Interference Shielding. *Advanced Functional Materials* **2017**, *27* (45), 1702807.
(115) Wang, X.; Weng, Q.; Yang, Y.; Bando, Y.; Golberg, D. Hybrid Two-Dimensional Materials in Rechargeable Battery Applications and Their Microscopic Mechanisms. *Chemical Society Reviews* **2016**, *45* (15), 4042–4073.

(116) Aierken, Y.; Sevik, C.; Gülseren, O.; Peeters, F. M.; Çakır, D. MXenes/Graphene Heterostructures for Li Battery Applications: A First Principles Study. *Journal of Materials Chemistry A* **2018**, *6* (5), 2337–2345.
(117) Chen, C.; Xie, X.; Anasori, B.; Sarycheva, A.; Makaryan, T.; Zhao, M.; Urbankowski, P.; Miao, L.; Jiang, J.; Gogotsi, Y. MoS2-on-MXene Heterostructures as Highly Reversible Anode Materials for Lithium-Ion Batteries. *Angewandte Chemie International Edition* **2018**, *57* (7), 1846–1850.
(118) Shao, Y.; Gong, P.; Pan, H.; Shi, X. H-/DT-MoS2-on-MXene Heterostructures as Promising 2D Anode Materials for Lithium-Ion Batteries: Insights from First Principles. *Advanced Theory and Simulations* **2019**, *2* (8), 1900045.
(119) Li, J.; Peng, Q.; Zhou, J.; Sun, Z. MoS2/Ti2CT2 (T= F, O) Heterostructures as Promising Flexible Anodes for Lithium/Sodium Ion Batteries. *The Journal of Physical Chemistry C* **2019**, *123* (18), 11493–11499.
(120) Jo, S.; Choo, S.; Kim, F.; Heo, S. H.; Son, J. S. Ink Processing for Thermoelectric Materials and Power-Generating Devices. *Advanced Materials* **2019**, *31* (20), 1804930.
(121) Orangi, J.; Hamade, F.; Davis, V. A.; Beidaghi, M. 3D Printing of Additive-Free 2D Ti3C2Tx (MXene) Ink for Fabrication of Micro-Supercapacitors with Ultra-High Energy Densities. *ACS nano* **2019**, *14*, 640–650.
(122) Zhao, M.-Q.; Torelli, M.; Ren, C. E.; Ghidiu, M.; Ling, Z.; Anasori, B.; Barsoum, M. W.; Gogotsi, Y. 2D Titanium Carbide and Transition Metal Oxides Hybrid Electrodes for Li-Ion Storage. *Nano Energy* **2016**, *30*, 603–613.
(123) Zhao, Q.; Zhu, Q.; Miao, J.; Zhang, P.; Wan, P.; He, L.; Xu, B. Flexible 3D Porous MXene Foam for High-Performance Lithium-Ion Batteries. *Small* **2019**, 1904293.
(124) Yu, P.; Cao, G.; Yi, S.; Zhang, X.; Li, C.; Sun, X.; Wang, K.; Ma, Y. Binder-Free 2D Titanium Carbide (MXene)/Carbon Nanotube Composites for High-Performance Lithium-Ion Capacitors. *Nanoscale* **2018**, *10* (13), 5906–5913. https://doi.org/10.1039/C8NR00380G.
(125) Jiao, S.; Zhou, A.; Wu, M.; Hu, H. Kirigami Patterning of MXene/Bacterial Cellulose Composite Paper for All-Solid-State Stretchable Micro-Supercapacitor Arrays. *Advanced Science* **2019**, *6*, 1900529.
(126) Tian, W.; VahidMohammadi, A.; Reid, M. S.; Wang, Z.; Ouyang, L.; Erlandsson, J.; Pettersson, T.; W\a agberg, L.; Beidaghi, M.; Hamedi, M. M. Multifunctional Nanocomposites with High Strength and Capacitance Using 2D MXene and 1D Nanocellulose. *Advanced Materials* **2019**, *31* (41), 1902977.
(127) Wang, Y.; Sun, J.; Qian, X.; Zhang, Y.; Yu, L.; Niu, R.; Zhao, H.; Zhu, J. 2D/2D Heterostructures of Nickel Molybdate and MXene with Strong Coupled Synergistic Effect towards Enhanced Supercapacitor Performance. *Journal of Power Sources* **2019**, *414*, 540–546.
(128) Zhou, S.; Yang, X.; Pei, W.; Liu, N.; Zhao, J. Heterostructures of MXenes and N-Doped Graphene as Highly Active Bifunctional Electrocatalysts. *Nanoscale* **2018**, *10* (23), 10876–10883.
(129) Zhao, M.-Q.; Ren, C. E.; Ling, Z.; Lukatskaya, M. R.; Zhang, C.; Van Aken, K. L.; Barsoum, M. W.; Gogotsi, Y. Flexible MXene/Carbon Nanotube Composite Paper with High Volumetric Capacitance. *Advanced Materials* **2015**, *27* (2), 339–345.

(130) Cheng, C.; Jiang, G.; Garvey, C. J.; Wang, Y.; Simon, G. P.; Liu, J. Z.; Li, D. Ion Transport in Complex Layered Graphene-Based Membranes with Tuneable Interlayer Spacing. *Science advances* **2016**, *2* (2), e1501272.
(131) Mi, B. Graphene Oxide Membranes for Ionic and Molecular Sieving. *Science* **2014**, *343* (6172), 740–742.
(132) Li, H.; Hou, Y.; Wang, F.; Lohe, M. R.; Zhuang, X.; Niu, L.; Feng, X. Flexible All-Solid-State Supercapacitors with High Volumetric Capacitances Boosted by Solution Processable MXene and Electrochemically Exfoliated Graphene. *Advanced Energy Materials* **2017**, *7* (4), 1601847.
(133) Fan, H. S.; Wang, H.; Zhao, N.; Xu, J.; Pan, F. Nano-Porous Architecture of N-Doped Carbon Nanorods Grown on Graphene to Enable Synergetic Effects of Supercapacitance. *Scientific reports* **2014**, *4*, 7426.
(134) Xu, S.; Wei, G.; Li, J.; Han, W.; Gogotsi, Y. Flexible MXene–Graphene Electrodes with High Volumetric Capacitance for Integrated Co-Cathode Energy Conversion/Storage Devices. *Journal of Materials Chemistry A* **2017**, *5* (33), 17442–17451.
(135) Zhao, C.; Wang, Q.; Zhang, H.; Passerini, S.; Qian, X. Two-Dimensional Titanium Carbide/RGO Composite for High-Performance Supercapacitors. *ACS Applied Materials & Interfaces* **2016**, *8* (24), 15661–15667. https://doi.org/10.1021/acsami.6b04767.
(136) Yan, J.; Ren, C. E.; Maleski, K.; Hatter, C. B.; Anasori, B.; Urbankowski, P.; Sarycheva, A.; Gogotsi, Y. Flexible MXene/Graphene Films for Ultrafast Supercapacitors with Outstanding Volumetric Capacitance. *Advanced Functional Materials* **2017**, *27* (30), 1701264.
(137) Zhao, M.; Trainor, N.; Ren, C. E.; Torelli, M.; Anasori, B.; Gogotsi, Y. Scalable Manufacturing of Large and Flexible Sheets of MXene/Graphene Heterostructures. *Advanced Materials Technologies* **2019**, *4* (5), 1800639. https://doi.org/10.1002/admt.201800639.
(138) Lukatskaya, M. R.; Bak, S.-M.; Yu, X.; Yang, X.-Q.; Barsoum, M. W.; Gogotsi, Y. Probing the Mechanism of High Capacitance in 2D Titanium Carbide Using in Situ X-Ray Absorption Spectroscopy. *Advanced Energy Materials* **2015**, *5* (15), 1500589.
(139) Qin, L.; Tao, Q.; El Ghazaly, A.; Fernandez-Rodriguez, J.; Persson, P. O.; Rosen, J.; Zhang, F. High-Performance Ultrathin Flexible Solid-State Supercapacitors Based on Solution Processable Mo1. 33C MXene and PEDOT: PSS. *Advanced Functional Materials* **2018**, *28* (2), 1703808.
(140) Boota, M.; Anasori, B.; Voigt, C.; Zhao, M.-Q.; Barsoum, M. W.; Gogotsi, Y. Pseudocapacitive Electrodes Produced by Oxidant-Free Polymerization of Pyrrole between the Layers of 2D Titanium Carbide (MXene). *Advanced Materials* **2016**, *28* (7), 1517–1522.
(141) Wu, Y.; Nie, P.; Wu, L.; Dou, H.; Zhang, X. 2D MXene/SnS2 Composites as High-Performance Anodes for Sodium Ion Batteries. *Chemical Engineering Journal* **2018**, *334*, 932–938. https://doi.org/10.1016/j.cej.2017.10.007.
(142) Liu, Y.-T.; Zhang, P.; Sun, N.; Anasori, B.; Zhu, Q.-Z.; Liu, H.; Gogotsi, Y.; Xu, B. Self-Assembly of Transition Metal Oxide Nanostructures on MXene Nanosheets for Fast and Stable Lithium Storage. *Advanced Materials* **2018**, *30* (23), 1707334.
(143) Fu, J.; Yun, J.; Wu, S.; Li, L.; Yu, L.; Kim, K. H. Architecturally Robust Graphene-Encapsulated MXene Ti $_2$ CT $_x$ @Polyaniline Composite for High-Performance Pouch-

Type Asymmetric Supercapacitor. *ACS Applied Materials & Interfaces* **2018**, *10* (40), 34212–34221. https://doi.org/10.1021/acsami.8b10195.

(144) Zhu, X.; Liu, B.; Hou, H.; Huang, Z.; Zeinu, K. M.; Huang, L.; Yuan, X.; Guo, D.; Hu, J.; Yang, J. Alkaline Intercalation of Ti 3 C 2 MXene for Simultaneous Electrochemical Detection of Cd(II), Pb(II), Cu(II) and Hg(II). *Electrochimica Acta* **2017**, *248*, 46–57. https://doi.org/10.1016/j.electacta.2017.07.084.

(145) Zhao, D.; Zhao, R.; Dong, S.; Miao, X.; Zhang, Z.; Wang, C.; Yin, L. Alkali-Induced 3D Crinkled Porous Ti_3C_2 MXene Architectures Coupled with NiCoP Bimetallic Phosphide Nanoparticles as Anodes for High-Performance Sodium-Ion Batteries. *Energy & Environmental Science* **2019**, *12* (8), 2422–2432.

(146) Zhao, D.; Clites, M.; Ying, G.; Kota, S.; Wang, J.; Natu, V.; Wang, X.; Pomerantseva, E.; Cao, M.; Barsoum, M. W. Alkali-Induced Crumpling of $Ti_3C_2T_x$ (MXene) to Form 3D Porous Networks for Sodium Ion Storage. *Chemical Communications* **2018**, *54* (36), 4533–4536. https://doi.org/10.1039/C8CC00649K.

(147) Ghidiu, M.; Halim, J.; Kota, S.; Bish, D.; Gogotsi, Y.; Barsoum, M. W. Ion-Exchange and Cation Solvation Reactions in Ti3C2 MXene. *Chemistry of Materials* **2016**, *28* (10), 3507–3514.

(148) Clites, M.; Byles, B. W.; Pomerantseva, E. Effect of Aging and Hydrothermal Treatment on Electrochemical Performance of Chemically Pre-Intercalated Na–V–O Nanowires for Na-Ion Batteries. *Journal of Materials Chemistry A* **2016**, *4* (20), 7754–7761.

(149) Wang, X.; Kajiyama, S.; Iinuma, H.; Hosono, E.; Oro, S.; Moriguchi, I.; Okubo, M.; Yamada, A. Pseudocapacitance of MXene Nanosheets for High-Power Sodium-Ion Hybrid Capacitors. *Nature Communications* **2015**, *6* (1), 6544.

(150) VahidMohammadi, A.; Mojtabavi, M.; Caffrey, N. M.; Wanunu, M.; Beidaghi, M. Assembling 2D MXenes into Highly Stable Pseudocapacitive Electrodes with High Power and Energy Densities. *Advanced Materials* **2019**, *31* (8), 1806931.

(151) Li, J.; Yuan, X.; Lin, C.; Yang, Y.; Xu, L.; Du, X.; Xie, J.; Lin, J.; Sun, J. Achieving High Pseudocapacitance of 2D Titanium Carbide (MXene) by Cation Intercalation and Surface Modification. *Advanced Energy Materials* **2017**, *7* (15), 1602725. https://doi.org/10.1002/aenm.201602725.

(152) Liu, D. S.; Ashcraft, J. N.; Mannarino, M. M.; Silberstein, M. N.; Argun, A. A.; Rutledge, G. C.; Boyce, M. C.; Hammond, P. T. Spray Layer-by-Layer Electrospun Composite Proton Exchange Membranes. *Advanced Functional Materials* **2013**, *23* (24), 3087–3095.

(153) Zhou, Z.; Panatdasirisuk, W.; Mathis, T. S.; Anasori, B.; Lu, C.; Zhang, X.; Liao, Z.; Gogotsi, Y.; Yang, S. Layer-by-Layer Assembly of MXene and Carbon Nanotubes on Electrospun Polymer Films for Flexible Energy Storage. *Nanoscale* **2018**, *10* (13), 6005–6013. https://doi.org/10.1039/C8NR00313K.

(154) Yang, M.; Hou, Y.; Kotov, N. A. Graphene-Based Multilayers: Critical Evaluation of Materials Assembly Techniques. *Nano Today* **2012**, *7* (5), 430–447.

(155) Zhang, C.-L.; Yu, S.-H. Nanoparticles Meet Electrospinning: Recent Advances and Future Prospects. *Chemical Society Reviews* **2014**, *43* (13), 4423–4448.

(156) An, H.; Habib, T.; Shah, S.; Gao, H.; Radovic, M.; Green, M. J.; Lutkenhaus, J. L. Surface-Agnostic Highly Stretchable and Bendable Conductive MXene Multilayers. *Science advances* **2018**, *4* (3), eaaq0118.

(157) Taberna, P. L.; Simon, P.; Fauvarque, J.-F. Electrochemical Characteristics and Impedance Spectroscopy Studies of Carbon-Carbon Supercapacitors. *Journal of The Electrochemical Society* **2003**, *150* (3), A292–A300.
(158) Weng, G.-M.; Li, J.; Alhabeb, M.; Karpovich, C.; Wang, H.; Lipton, J.; Maleski, K.; Kong, J.; Shaulsky, E.; Elimelech, M. Layer-by-Layer Assembly of Cross-Functional Semi-Transparent MXene-Carbon Nanotubes Composite Films for Next-Generation Electromagnetic Interference Shielding. *Advanced Functional Materials* **2018**, *28* (44), 1803360.
(159) Yue, Y.; Liu, N.; Ma, Y.; Wang, S.; Liu, W.; Luo, C.; Zhang, H.; Cheng, F.; Rao, J.; Hu, X. Highly Self-Healable 3D Microsupercapacitor with MXene–Graphene Composite Aerogel. *ACS nano* **2018**, *12* (5), 4224–4232.
(160) Cao, X.; Yin, Z.; Zhang, H. Three-Dimensional Graphene Materials: Preparation, Structures and Application in Supercapacitors. *Energy & Environmental Science* **2014**, *7* (6), 1850–1865.
(161) Zhang, L.; DeArmond, D.; Alvarez, N. T.; Malik, R.; Oslin, N.; McConnell, C.; Adusei, P. K.; Hsieh, Y.-Y.; Shanov, V. Flexible Micro-Supercapacitor Based on Graphene with 3D Structure. *Small* **2017**, *13* (10), 1603114.
(162) Huang, Y.; Liang, J.; Chen, Y. An Overview of the Applications of Graphene-Based Materials in Supercapacitors. *Small* **2012**, *8* (12), 1805–1834.
(163) Yang, W.; Yang, J.; Byun, J. J.; Moissinac, F. P.; Xu, J.; Haigh, S. J.; Domingos, M.; Bissett, M. A.; Dryfe, R. A.; Barg, S. 3D Printing of Freestanding MXene Architectures for Current-Collector-Free Supercapacitors. *Advanced Materials* **2019**, *31* (37), 1902725.
(164) Zhang, Y.-Z.; Wang, Y.; Jiang, Q.; El-Demellawi, J. K.; Kim, H.; Alshareef, H. N. MXene Printing and Patterned Coating for Device Applications. *Advanced Materials* **2020**.
(165) Zhang, C. J.; McKeon, L.; Kremer, M. P.; Park, S.-H.; Ronan, O.; Seral-Ascaso, A.; Barwich, S.; Coileáin, C. Ó.; McEvoy, N.; Nerl, H. C. Additive-Free MXene Inks and Direct Printing of Micro-Supercapacitors. *Nature Communications* **2019**, *10* (1), 1795.
(166) Fan, Z.; Wei, C.; Yu, L.; Xia, Z.; Cai, J.; Tian, Z.; Zou, G.; Dou, S. X.; Sun, J. 3D Printing of Porous Nitrogen-Doped Ti3C2 MXene Scaffolds for High-Performance Sodium-Ion Hybrid Capacitors. *ACS nano* **2020**, *14* (1), 867–876.
(167) Yu, L.; Fan, Z.; Shao, Y.; Tian, Z.; Sun, J.; Liu, Z. Versatile N-Doped MXene Ink for Printed Electrochemical Energy Storage Application. *Advanced Energy Materials* **2019**, *9* (34), 1901839.
(168) Akuzum, B.; Maleski, K.; Anasori, B.; Lelyukh, P.; Alvarez, N. J.; Kumbur, E. C.; Gogotsi, Y. Rheological Characteristics of 2D Titanium Carbide (MXene) Dispersions: A Guide for Processing MXenes. *ACS nano* **2018**, *12* (3), 2685–2694.
(169) Xu, S.; Dall'Agnese, Y.; Wei, G.; Zhang, C.; Gogotsi, Y.; Han, W. Screen-Printable Microscale Hybrid Device Based on MXene and Layered Double Hydroxide Electrodes for Powering Force Sensors. *Nano Energy* **2018**, *50*, 479–488. https://doi.org/10.1016/j.nanoen.2018.05.064.
(170) Li, H.; Li, X.; Liang, J.; Chen, Y. Hydrous RuO2-Decorated MXene Coordinating with Silver Nanowire Inks Enabling Fully Printed Micro-Supercapacitors with Extraordinary Volumetric Performance. *Advanced Energy Materials* **2019**, *9* (15), 1803987.
(171) Wu, C.-W.; Unnikrishnan, B.; Chen, I.-W. P.; Harroun, S. G.; Chang, H.-T.; Huang, C.-C. Excellent Oxidation Resistive MXene Aqueous Ink for Micro-Supercapacitor Application. *Energy Storage Materials* **2019**, *25*, 563–571.

(172) Zhao, J.; Zhang, Y.; Huang, Y.; Zhao, X.; Shi, Y.; Qu, J.; Yang, C.; Xie, J.; Wang, J.; Li, L. Duplex Printing of All-in-One Integrated Electronic Devices for Temperature Monitoring. *Journal of Materials Chemistry A* **2019**, *7* (3), 972–978.
(173) Li, L.; Zhang, M.; Zhang, X.; Zhang, Z. New Ti3C2 Aerogel as Promising Negative Electrode Materials for Asymmetric Supercapacitors. *Journal of Power Sources* **2017**, *364*, 234–241.
(174) Zhang, X.; Lv, R.; Wang, A.; Guo, W.; Liu, X.; Luo, J. MXene Aerogel Scaffolds for High-Rate Lithium Metal Anodes. *Angewandte Chemie* **2018**, *130* (46), 15248–15253.
(175) Bian, R.; He, G.; Zhi, W.; Xiang, S.; Wang, T.; Cai, D. Ultralight MXene-Based Aerogels with High Electromagnetic Interference Shielding Performance. *Journal of Materials Chemistry C* **2019**, *7* (3), 474–478.
(176) Liu, J.; Zhang, H.-B.; Xie, X.; Yang, R.; Liu, Z.; Liu, Y.; Yu, Z.-Z. Multifunctional, Superelastic, and Lightweight MXene/Polyimide Aerogels. *Small* **2018**, *14* (45), 1802479.
(177) Ma, Y.; Yue, Y.; Zhang, H.; Cheng, F.; Zhao, W.; Rao, J.; Luo, S.; Wang, J.; Jiang, X.; Liu, Z. 3D Synergistical MXene/Reduced Graphene Oxide Aerogel for a Piezoresistive Sensor. *ACS nano* **2018**, *12* (4), 3209–3216.
(178) Zhao, S.; Zhang, H.-B.; Luo, J.-Q.; Wang, Q.-W.; Xu, B.; Hong, S.; Yu, Z.-Z. Highly Electrically Conductive Three-Dimensional Ti3C2T x MXene/Reduced Graphene Oxide Hybrid Aerogels with Excellent Electromagnetic Interference Shielding Performances. *ACS nano* **2018**, *12* (11), 11193–11202.
(179) Kyerematen, N. A.; Brousse, T.; Pech, D. Microsupercapacitors as Miniaturized Energy-Storage Components for on-Chip Electronics. *Nature nanotechnology* **2017**, *12* (1), 7.
(180) Li, H.; Liang, J. Recent Development of Printed Micro-Supercapacitors: Printable Materials, Printing Technologies, and Perspectives. *Advanced Materials* **2019**, 1805864.
(181) Zhang, P.; Zhu, F.; Wang, F.; Wang, J.; Dong, R.; Zhuang, X.; Schmidt, O. G.; Feng, X. Stimulus-Responsive Micro-Supercapacitors with Ultrahigh Energy Density and Reversible Electrochromic Window. *Advanced Materials* **2017**, *29* (7).
(182) Zhang, C. J.; Maloney, R.; Lukatskaya, M. R.; Beidaghi, M.; Dyatkin, B.; Perre, E.; Long, D.; Qiao, W.; Dunn, B.; Gogotsi, Y. Synthesis and Electrochemical Properties of Niobium Pentoxide Deposited on Layered Carbide-Derived Carbon. *Journal of Power Sources* **2015**, *274*, 121–129.
(183) Zhang, C.; Hatzell, K. B.; Boota, M.; Dyatkin, B.; Beidaghi, M.; Long, D.; Qiao, W.; Kumbur, E. C.; Gogotsi, Y. Highly Porous Carbon Spheres for Electrochemical Capacitors and Capacitive Flowable Suspension Electrodes. *Carbon* **2014**, *77*, 155–164.
(184) Kong, L.; Zhang, C.; Wang, J.; Long, D.; Qiao, W.; Ling, L. Ultrahigh Intercalation Pseudocapacitance of Mesoporous Orthorhombic Niobium Pentoxide from a Novel Cellulose Nanocrystal Template. *Materials Chemistry and Physics* **2015**, *149*, 495–504.
(185) Xiao, X.; Song, H.; Lin, S.; Zhou, Y.; Zhan, X.; Hu, Z.; Zhang, Q.; Sun, J.; Yang, B.; Li, T. Scalable Salt-Templated Synthesis of Two-Dimensional Transition Metal Oxides. *Nature communications* **2016**, *7*, 11296.
(186) Hu, Z.; Xiao, X.; Jin, H.; Li, T.; Chen, M.; Liang, Z.; Guo, Z.; Li, J.; Wan, J.; Huang, L. Rapid Mass Production of Two-Dimensional Metal Oxides and Hydroxides via the Molten Salts Method. *Nature communications* **2017**, *8*, 15630.
(187) Kim, B. C.; Hong, J.-Y.; Wallace, G. G.; Park, H. S. Recent Progress in Flexible Electrochemical Capacitors: Electrode Materials, Device Configuration, and Functions. *Advanced Energy Materials* **2015**, *5* (22), 1500959.

(188) Gogotsi, Y.; Simon, P. True Performance Metrics in Electrochemical Energy Storage. *Science* **2011**, *334* (6058), 917–918.
(189) Shen, K.; Ding, J.; Yang, S. 3D Printing Quasi-Solid-State Asymmetric Micro-Supercapacitors with Ultrahigh Areal Energy Density. *Advanced Energy Materials* **2018**, 1800408.
(190) Chang, P.; Mei, H.; Zhou, S.; Dassios, K. G.; Cheng, L. 3D Printed Electrochemical Energy Storage Devices. *Journal of Materials Chemistry A* **2019**, *7* (9), 4230–4258.
(191) Wei, T.-S.; Ahn, B. Y.; Grotto, J.; Lewis, J. A. 3D Printing of Customized Li-Ion Batteries with Thick Electrodes. *Advanced Materials* **2018**, *8* (20), 1703027.
(192) Sun, K.; Wei, T.-S.; Ahn, B. Y.; Seo, J. Y.; Dillon, S. J.; Lewis, J. A. 3D Printing of Interdigitated Li-Ion Microbattery Architectures. *Advanced materials* **2013**, *25* (33), 4539–4543.
(193) Gross, B. C.; Erkal, J. L.; Lockwood, S. Y.; Chen, C.; Spence, D. M. Evaluation of 3D Printing and Its Potential Impact on Biotechnology and the Chemical Sciences. **2014**, 3240–3253.
(194) Compton, B. G.; Lewis, J. A. 3D-Printing of Lightweight Cellular Composites. *Advanced materials* **2014**, *26* (34), 5930–5935.
(195) Lewis, J. A. Direct Ink Writing of 3D Functional Materials. *Advanced Functional Materials* **2006**, *16* (17), 2193–2204.
(196) Lewis, J. A.; Gratson, G. M. Direct Writing in Three Dimensions. *Materials today* **2004**, *7* (7–8), 32–39.
(197) Fu, K.; Wang, Y.; Yan, C.; Yao, Y.; Chen, Y.; Dai, J.; Lacey, S.; Wang, Y.; Wan, J.; Li, T. Graphene Oxide-Based Electrode Inks for 3D-Printed Lithium-Ion Batteries. *Advanced Materials* **2016**, *28* (13), 2587–2594.
(198) Guo, Y.; Patanwala, H. S.; Bognet, B.; Ma, A. W. Inkjet and Inkjet-Based 3D Printing: Connecting Fluid Properties and Printing Performance. *Rapid Prototyping Journal* **2017**, *23* (3), 562–576.
(199) Ambrosi, A.; Pumera, M. 3D-Printing Technologies for Electrochemical Applications. *Chemical Society Reviews* **2016**, *45* (10), 2740–2755.
(200) Moyano, J. J.; Gómez-Gómez, A.; Pérez-Coll, D.; Belmonte, M.; Miranzo, P.; Osendi, M. I. Filament Printing of Graphene-Based Inks into Self-Supported 3D Architectures. *Carbon* **2019**, *151*, 94–102.
(201) Naguib, M.; Halim, J.; Lu, J.; Cook, K. M.; Hultman, L.; Gogotsi, Y.; Barsoum, M. W. New Two-Dimensional Niobium and Vanadium Carbides as Promising Materials for Li-Ion Batteries. *Journal of the American Chemical Society* **2013**, *135* (43), 15966–15969. https://doi.org/10.1021/ja405735d.
(202) Lukatskaya, Maria. R.; Mashtalir, O.; Ren, C. E.; Dall'Agnese, Y.; Rozier, P.; Taberna, P.-L.; Naguib, M.; Simon, P.; Barsoum, M. W.; Gogotsi, Y. Cation Intercalation and High Volumetric Capacitance of Two-Dimensional Titanium Carbide. *Science* **2013**, *341* (6153), 1502–1505. https://doi.org/10.1126/science.1238017.
(203) Hope, M.; Forse, A. C.; Griffith, K.; Lukatskaya, M. R.; Ghidiu, M.; Gogotsi, Y.; Grey, C. P. NMR Reveals the Surface Functionalisation of Ti_3C_2 MXene. **2016**.
(204) Mashtalir, O.; Lukatskaya, M. R.; Kolesnikov, A. I.; Raymundo-Pinero, E.; Naguib, M.; Barsoum, M. W.; Gogotsi, Y. The Effect of Hydrazine Intercalation on the Structure and Capacitance of 2D Titanium Carbide (MXene). *Nanoscale* **2016**, *8* (17), 9128–9133.

(205) Mashtalir, O.; Lukatskaya, M. R.; Zhao, M.-Q.; Barsoum, M. W.; Gogotsi, Y. Amine-Assisted Delamination of Nb $_2$ C MXene for Li-Ion Energy Storage Devices. *Advanced Materials* **2015**, *27* (23), 3501–3506. https://doi.org/10.1002/adma.201500604.
(206) Peng, Y.-Y.; Akuzum, B.; Kurra, N.; Zhao, M.-Q.; Alhabeb, M.; Anasori, B.; Kumbur, E. C.; Alshareef, H. N.; Ger, M.-D.; Gogotsi, Y. All-MXene (2D Titanium Carbide) Solid-State Microsupercapacitors for on-Chip Energy Storage. *Energy & Environmental Science* **2016**, *9* (9), 2847–2854.
(207) Shen, B.-S.; Wang, H.; Wu, L.-J.; Guo, R.-S.; Huang, Q.; Yan, X.-B. All-Solid-State Flexible Microsupercapacitor Based on Two-Dimensional Titanium Carbide. *Chinese Chemical Letters* **2016**, *27* (10), 1586–1591.
(208) Zhang, C. J.; Kremer, M. P.; Seral-Ascaso, A.; Park, S.-H.; McEvoy, N.; Anasori, B.; Gogotsi, Y.; Nicolosi, V. Stamping of Flexible, Coplanar Micro-Supercapacitors Using MXene Inks. *Advanced Functional Materials* **2018**, *28* (9), 17055506.
(209) Mashtalir, O.; Naguib, M.; Mochalin, V. N.; Dall'Agnese, Y.; Heon, M.; Barsoum, M. W.; Gogotsi, Y. Intercalation and Delamination of Layered Carbides and Carbonitrides. *Nature Communications* **2013**, *4*, 1716. https://doi.org/10.1038/ncomms2664.
(210) M'barki, A.; Bocquet, L.; Stevenson, A. Linking Rheology and Printability for Dense and Strong Ceramics by Direct Ink Writing. *Scientific reports* **2017**, *7* (1), 6017.
(211) Smay, J. E.; Cesarano, J.; Lewis, J. A. Colloidal Inks for Directed Assembly of 3-D Periodic Structures. *Langmuir* **2002**, *18* (14), 5429–5437.
(212) Naficy, S.; Jalili, R.; Aboutalebi, S. H.; Gorkin III, R. A.; Konstantinov, K.; Innis, P. C.; Spinks, G. M.; Poulin, P.; Wallace, G. G. Graphene Oxide Dispersions: Tuning Rheology to Enable Fabrication. *Materials Horizons* **2014**, *1* (3), 326–331.
(213) Lipatov, A.; Alhabeb, M.; Lukatskaya, M. R.; Boson, A.; Gogotsi, Y.; Sinitskii, A. Effect of Synthesis on Quality, Electronic Properties and Environmental Stability of Individual Monolayer Ti $_3$ C $_2$ MXene Flakes. *Advanced Electronic Materials* **2016**, *2* (12), 1600255. https://doi.org/10.1002/aelm.201600255.
(214) Zhang, C. J.; Pinilla, S.; McEvoy, N.; Cullen, C. P.; Anasori, B.; Long, E.; Park, S.-H.; Seral-Ascaso, A.; Shmeliov, A.; Krishnan, D. Oxidation Stability of Colloidal Two-Dimensional Titanium Carbides (MXenes). *Chemistry of Materials* **2017**, *29* (11), 4848–4856.
(215) Akbari, A.; Sheath, P.; Martin, S. T.; Shinde, D. B.; Shaibani, M.; Banerjee, P. C.; Tkacz, R.; Bhattacharyya, D.; Majumder, M. Large-Area Graphene-Based Nanofiltration Membranes by Shear Alignment of Discotic Nematic Liquid Crystals of Graphene Oxide. *Nature communications* **2016**, *7*, 10891.
(216) Tian, X.; Jin, J.; Yuan, S.; Chua, C. K.; Tor, S. B.; Zhou, K. Emerging 3D-Printed Electrochemical Energy Storage Devices: A Critical Review. *Advanced Energy Materials* **2017**, *7* (17), 1700127.
(217) Zhang, C. (John); Higgins, T. M.; Park, S.-H.; O'Brien, S. E.; Long, D.; Coleman, J. N.; Nicolosi, V. Highly Flexible and Transparent Solid-State Supercapacitors Based on RuO2/PEDOT:PSS Conductive Ultrathin Films. *Nano Energy* **2016**, *28*, 495–505. https://doi.org/10.1016/j.nanoen.2016.08.052.
(218) Abdelkader, A. M.; Karim, N.; Vallés, C.; Afroj, S.; Novoselov, K. S.; Yeates, S. G. Ultraflexible and Robust Graphene Supercapacitors Printed on Textiles for Wearable Electronics Applications. *2D Materials* **2017**, *4* (3), 035016.

(219) Bard, A. J.; Faulkner, L. R. Fundamentals and Applications. *Electrochemical Methods* **2001**, *2*, 482.
(220) Ling, Z.; Harvey, A.; McAteer, D.; Godwin, I. J.; Szyd\lowska, B.; Griffin, A.; Vega-Mayoral, V.; Song, Y.; Seral-Ascaso, A.; Nicolosi, V. Quantifying the Role of Nanotubes in Nano: Nano Composite Supercapacitor Electrodes. *Advanced Energy Materials* **2018**, *8* (8), 1702364.
(221) Higgins, T. M.; Coleman, J. N. Avoiding Resistance Limitations in High-Performance Transparent Supercapacitor Electrodes Based on Large-Area, High-Conductivity PEDOT: PSS Films. *ACS applied materials & interfaces* **2015**, *7* (30), 16495–16506.
(222) Cunningham, G.; Khan, U.; Backes, C.; Hanlon, D.; McCloskey, D.; Donegan, J. F.; Coleman, J. N. Photoconductivity of Solution-Processed MoS 2 Films. *Journal of Materials Chemistry C* **2013**, *1* (41), 6899–6904.
(223) Tian, X.; Itkis, M. E.; Bekyarova, E. B.; Haddon, R. C. Anisotropic Thermal and Electrical Properties of Thin Thermal Interface Layers of Graphite Nanoplatelet-Based Composites. *Scientific reports* **2013**, *3*, 1710.
(224) Li, W.; Li, Y.; Su, M.; An, B.; Liu, J.; Su, D.; Li, L.; Li, F.; Song, Y. Printing Assembly and Structural Regulation of Graphene towards Three-Dimensional Flexible Micro-Supercapacitors. *Journal of Materials Chemistry A* **2017**, *5* (31), 16281–16288.
(225) Zhou, J.; Yu, J.; Shi, L.; Wang, Z.; Liu, H.; Yang, B.; Li, C.; Zhu, C.; Xu, J. A Conductive and Highly Deformable All-Pseudocapacitive Composite Paper as Supercapacitor Electrode with Improved Areal and Volumetric Capacitance. *Small* **2018**, *14* (51), 1803786.
(226) Huang, H.; Su, H.; Zhang, H.; Xu, L.; Chu, X.; Hu, C.; Liu, H.; Chen, N.; Liu, F.; Deng, W. Extraordinary Areal and Volumetric Performance of Flexible Solid-State Micro-Supercapacitors Based on Highly Conductive Freestanding Ti3C2Tx Films. *Advanced Electronic Materials* **2018**, *4* (8), 1800179.
(227) Quain, E.; Mathis, T. S.; Kurra, N.; Maleski, K.; Van Aken, K. L.; Alhabeb, M.; Alshareef, H. N.; Gogotsi, Y. Direct Writing of Additive-Free MXene-in-Water Ink for Electronics and Energy Storage. *Advanced Materials Technologies* **2018**, *4* (1), 1800256.
(228) Hu, H.; Hua, T. An Easily Manipulated Protocol for Patterning of MXenes on Paper for Planar Micro-Supercapacitors. *Journal of Materials Chemistry A* **2017**, *5* (37), 19639–19648.
(229) Kurra, N.; Ahmed, B.; Gogotsi, Y.; Alshareef, H. N. MXene-on-Paper Coplanar Microsupercapacitors. *Advanced Energy Materials* **2016**, *6* (24), 1601372.
(230) Zhang, C. J.; Anasori, B.; Seral-Ascaso, A.; Park, S.-H.; McEvoy, N.; Shmeliov, A.; Duesberg, G. S.; Coleman, J. N.; Gogotsi, Y.; Nicolosi, V. Transparent, Flexible, and Conductive 2D Titanium Carbide (MXene) Films with High Volumetric Capacitance. *Advanced Materials* **2017**, *29* (36).
(231) Jiang, Q.; Wu, C.; Wang, Z.; Wang, A. C.; He, J.-H.; Wang, Z. L.; Alshareef, H. N. MXene Electrochemical Microsupercapacitor Integrated with Triboelectric Nanogenerator as a Wearable Self-Charging Power Unit. *Nano Energy* **2018**, *45*, 266–272.
(232) Liu, W.-W.; Feng, Y.-Q.; Yan, X.-B.; Chen, J.-T.; Xue, Q.-J. Superior Micro-Supercapacitors Based on Graphene Quantum Dots. *Advanced Functional Materials* **2013**, *23* (33), 4111–4122.
(233) Liu, W.; Lu, C.; Li, H.; Tay, R. Y.; Sun, L.; Wang, X.; Chow, W. L.; Wang, X.; Tay, B. K.; Chen, Z. Based All-Solid-State Flexible Micro-Supercapacitors with Ultra-High Rate

and Rapid Frequency Response Capabilities. *Journal of Materials Chemistry A* **2016**, *4* (10), 3754–3764.
(234) Eustache, E.; Frappier, R.; Porto, R. L.; Bouhtiyya, S.; Pierson, J.-F.; Brousse, T. Asymmetric Electrochemical Capacitor Microdevice Designed with Vanadium Nitride and Nickel Oxide Thin Film Electrodes. *Electrochemistry Communications* **2013**, *28*, 104–106.
(235) Wang, K.; Wu, H.; Meng, Y.; Wei, Z. Conducting Polymer Nanowire Arrays for High Performance Supercapacitors. *Small* **2014**, *10* (1), 14–31.
(236) El-Kady, M. F.; Kaner, R. B. Scalable Fabrication of High-Power Graphene Micro-Supercapacitors for Flexible and on-Chip Energy Storage. *Nature communications* **2013**, *4*, ncomms2446.
(237) Kurra, N.; Alhebshi, N. A.; Alshareef, H. N. Microfabricated Pseudocapacitors Using Ni (OH) 2 Electrodes Exhibit Remarkable Volumetric Capacitance and Energy Density. *Advanced Energy Materials* **2015**, *5* (2), 1401303.
(238) Si, W.; Yan, C.; Chen, Y.; Oswald, S.; Han, L.; Schmidt, O. G. On Chip, All Solid-State and Flexible Micro-Supercapacitors with High Performance Based on MnO x/Au Multilayers. *Energy & Environmental Science* **2013**, *6* (11), 3218–3223.
(239) Pech, D.; Brunet, M.; Durou, H.; Huang, P.; Mochalin, V.; Gogotsi, Y.; Taberna, P.-L.; Simon, P. Ultrahigh-Power Micrometre-Sized Supercapacitors Based on Onion-like Carbon. *Nature nanotechnology* **2010**, *5* (9), 651.
(240) Hu, H.; Bai, Z.; Niu, B.; Wu, M.; Hua, T. Binder-Free Bonding of Modularized MXene Thin Films into Thick Film Electrodes for on-Chip Micro-Supercapacitors with Enhanced Areal Performance Metrics. *Journal of Materials Chemistry A* **2018**, *6* (30), 14876–14884.
(241) Fang, Q.; Shen, Y.; Chen, B. Synthesis, Decoration and Properties of Three-Dimensional Graphene-Based Macrostructures: A Review. *Chemical Engineering Journal* **2015**, *264*, 753–771.
(242) García-Tuñon, E.; Barg, S.; Franco, J.; Bell, R.; Eslava, S.; D'Elia, E.; Maher, R. C.; Guitian, F.; Saiz, E. Printing in Three Dimensions with Graphene. *Advanced Materials* **2015**, *27* (10), 1688–1693.
(243) Zhu, J.; Ha, E.; Zhao, G.; Zhou, Y.; Huang, D.; Yue, G.; Hu, L.; Sun, N.; Wang, Y.; Lee, L. Y. S. Recent Advance in MXenes: A Promising 2D Material for Catalysis, Sensor and Chemical Adsorption. *Coordination Chemistry Reviews* **2017**, *352*, 306–327.
(244) Cai, Y.; Shen, J.; Ge, G.; Zhang, Y.; Jin, W.; Huang, W.; Shao, J.; Yang, J.; Dong, X. Stretchable Ti3C2T x MXene/Carbon Nanotube Composite Based Strain Sensor with Ultrahigh Sensitivity and Tunable Sensing Range. *ACS nano* **2017**, *12* (1), 56–62.
(245) Hu, Q.; Sun, D.; Wu, Q.; Wang, H.; Wang, L.; Liu, B.; Zhou, A.; He, J. MXene: A New Family of Promising Hydrogen Storage Medium. *The Journal of Physical Chemistry A* **2013**, *117* (51), 14253–14260.
(246) Jiang, J.; Li, Y.; Liu, J.; Huang, X.; Yuan, C.; Lou, X. W. Recent Advances in Metal Oxide-Based Electrode Architecture Design for Electrochemical Energy Storage. *Advanced materials* **2012**, *24* (38), 5166–5180.
(247) Jung, S. M.; Mafra, D. L.; Lin, C.-T.; Jung, H. Y.; Kong, J. Controlled Porous Structures of Graphene Aerogels and Their Effect on Supercapacitor Performance. *Nanoscale* **2015**, *7* (10), 4386–4393.

(248) Naguib, M.; Kurtoglu, M.; Presser, V.; Lu, J.; Niu, J.; Heon, M.; Hultman, L.; Gogotsi, Y.; Barsoum, M. W. Two-Dimensional Nanocrystals Produced by Exfoliation of Ti3AlC2. *Advanced Materials* **2011**, *23* (37), 4248–4253.
(249) Anasori, B.; Lukatskaya, M. R.; Gogotsi, Y. 2D Metal Carbides and Nitrides (MXenes) for Energy Storage. *Nature Reviews Materials* **2017**, *2* (2), 16098.
(250) Lee, E.; VahidMohammadi, A.; Prorok, B. C.; Yoon, Y. S.; Beidaghi, M.; Kim, D.-J. Room Temperature Gas Sensing of Two-Dimensional Titanium Carbide (MXene). *ACS applied materials & interfaces* **2017**, *9* (42), 37184–37190.
(251) Shpigel, N.; Levi, M. D.; Sigalov, S.; Mathis, T. S.; Gogotsi, Y.; Aurbach, D. Direct Assessment of Nano-Confined Water in 2D Ti3C2 (MXene) Electrode Interspaces by a Surface Acoustic Technique. *Journal of the American Chemical Society* **2018**.
(252) Lian, P.; Dong, Y.; Wu, Z.-S.; Zheng, S.; Wang, X.; Wang, S.; Sun, C.; Qin, J.; Shi, X.; Bao, X. Alkalized Ti3C2 MXene Nanoribbons with Expanded Interlayer Spacing for High-Capacity Sodium and Potassium Ion Batteries. *Nano Energy* **2017**, *40*, 1–8.
(253) Naguib, M.; Halim, J.; Lu, J.; Cook, K. M.; Hultman, L.; Gogotsi, Y.; Barsoum, M. W. New Two-Dimensional Niobium and Vanadium Carbides as Promising Materials for Li-Ion Batteries. *Journal of the American Chemical Society* **2013**, *135* (43), 15966–15969. https://doi.org/10.1021/ja405735d.
(254) Boota, M.; Pasini, M.; Galeotti, F.; Porzio, W.; Zhao, M.-Q.; Halim, J.; Gogotsi, Y. Interaction of Polar and Nonpolar Polyfluorenes with Layers of Two-Dimensional Titanium Carbide (MXene): Intercalation and Pseudocapacitance. *Chemistry of Materials* **2017**, *29* (7), 2731–2738. https://doi.org/10.1021/acs.chemmater.6b03933.
(255) Dall'Agnese, Y.; Rozier, P.; Taberna, P.-L.; Gogotsi, Y.; Simon, P. Capacitance of Two-Dimensional Titanium Carbide (MXene) and MXene/Carbon Nanotube Composites in Organic Electrolytes. *Journal of Power Sources* **2016**, *306*, 510–515.
(256) Boota, M.; Anasori, B.; Voigt, C.; Zhao, M.-Q.; Barsoum, M. W.; Gogotsi, Y. Pseudocapacitive Electrodes Produced by Oxidant-Free Polymerization of Pyrrole between the Layers of 2D Titanium Carbide (MXene). *Advanced Materials* **2016**, *28* (7), 1517–1522.
(257) Liu, R.; Miao, M.; Li, Y.; Zhang, J.; Cao, S.; Feng, X. Ultrathin Biomimetic Polymeric $Ti_3C_2T_x$ MXene Composite Films for Electromagnetic Interference Shielding. *ACS Applied Materials & Interfaces* **2018**, *10* (51), 44787–44795. https://doi.org/10.1021/acsami.8b18347.
(258) Ren, C. E.; Zhao, M.-Q.; Makaryan, T.; Halim, J.; Boota, M.; Kota, S.; Anasori, B.; Barsoum, M. W.; Gogotsi, Y. Porous Two-Dimensional Transition Metal Carbide (MXene) Flakes for High-Performance Li-Ion Storage. *ChemElectroChem* **2016**, *3* (5), 689–693.
(259) Wen, Y.; Rufford, T. E.; Chen, X.; Li, N.; Lyu, M.; Dai, L.; Wang, L. Nitrogen-Doped Ti3C2Tx MXene Electrodes for High-Performance Supercapacitors. *Nano energy* **2017**, *38*, 368–376.
(260) Mashtalir, O.; Cook, K. M.; Mochalin, V. N.; Crowe, M.; Barsoum, M. W.; Gogotsi, Y. Dye Adsorption and Decomposition on Two-Dimensional Titanium Carbide in Aqueous Media. *Journal of Materials Chemistry A* **2014**, *2* (35), 14334–14338.
(261) Shah, S. A.; Habib, T.; Gao, H.; Gao, P.; Sun, W.; Green, M. J.; Radovic, M. Template-Free 3D Titanium Carbide (Ti 3 C 2 T x) MXene Particles Crumpled by Capillary Forces. *Chemical Communications* **2017**, *53* (2), 400–403.

(262) VahidMohammadi, A.; Hadjikhani, A.; Shahbazmohamadi, S.; Beidaghi, M. Two-Dimensional Vanadium Carbide (MXene) as a High-Capacity Cathode Material for Rechargeable Aluminum Batteries. *ACS nano* **2017**, *11* (11), 11135–11144.
(263) Deville, S. Freeze-Casting of Porous Ceramics: A Review of Current Achievements and Issues. *Advanced Engineering Materials* **2008**, *10* (3), 155–169.
(264) Bai, H.; Chen, Y.; Delattre, B.; Tomsia, A. P.; Ritchie, R. O. Bioinspired Large-Scale Aligned Porous Materials Assembled with Dual Temperature Gradients. *Science advances* **2015**, *1* (11), e1500849.
(265) Meza, L. R.; Das, S.; Greer, J. R. Strong, Lightweight, and Recoverable Three-Dimensional Ceramic Nanolattices. *Science* **2014**, *345* (6202), 1322–1326.
(266) Zhang, Q.; Lin, D.; Deng, B.; Xu, X.; Nian, Q.; Jin, S.; Leedy, K. D.; Li, H.; Cheng, G. J. Flyweight, Superelastic, Electrically Conductive, and Flame-Retardant 3D Multi-Nanolayer Graphene/Ceramic Metamaterial. *Advanced Materials* **2017**, *29* (28).
(267) Wang, H.; Zhang, X.; Wang, N.; Li, Y.; Feng, X.; Huang, Y.; Zhao, C.; Liu, Z.; Fang, M.; Ou, G. Ultralight, Scalable, and High-Temperature–Resilient Ceramic Nanofiber Sponges. *Science advances* **2017**, *3* (6), e1603170.
(268) Zhang, Q.; Zhang, F.; Medarametla, S. P.; Li, H.; Zhou, C.; Lin, D. 3D Printing of Graphene Aerogels. *Small* **2016**, *12* (13), 1702–1708.
(269) Yan, P.; Brown, E.; Su, Q.; Li, J.; Wang, J.; Xu, C.; Zhou, C.; Lin, D. 3D Printing Hierarchical Silver Nanowire Aerogel With Highly Compressive Resilience and Tensile Elongation Through Tunable Poisson's Ratio. *small* **2017**, *13* (38).
(270) Zhang, Q.; Xu, X.; Lin, D.; Chen, W.; Xiong, G.; Yu, Y.; Fisher, T. S.; Li, H. Hyperbolically Patterned 3D Graphene Metamaterial with Negative Poisson's Ratio and Superelasticity. *Advanced materials* **2016**, *28* (11), 2229–2237.
(271) Zhu, C.; Han, T. Y.-J.; Duoss, E. B.; Golobic, A. M.; Kuntz, J. D.; Spadaccini, C. M.; Worsley, M. A. Highly Compressible 3D Periodic Graphene Aerogel Microlattices. *Nature communications* **2015**, *6*, 6962.
(272) Qiu, L.; Liu, J. Z.; Chang, S. L.; Wu, Y.; Li, D. Biomimetic Superelastic Graphene-Based Cellular Monoliths. *Nature communications* **2012**, *3*, 1241.
(273) Qian, F.; Lan, P. C.; Freyman, M. C.; Chen, W.; Kou, T.; Olson, T. Y.; Zhu, C.; Worsley, M. A.; Duoss, E. B.; Spadaccini, C. M. Ultralight Conductive Silver Nanowire Aerogels. *Nano letters* **2017**, *17* (12), 7171–7176.
(274) Tang, Y.; Yeo, K. L.; Chen, Y.; Yap, L. W.; Xiong, W.; Cheng, W. Ultralow-Density Copper Nanowire Aerogel Monoliths with Tunable Mechanical and Electrical Properties. *Journal of Materials Chemistry A* **2013**, *1* (23), 6723–6726.
(275) Hui, X.; Zhao, R.; Zhang, P.; Li, C.; Wang, C.; Yin, L. Low-Temperature Reduction Strategy Synthesized Si/Ti3C2 MXene Composite Anodes for High-Performance Li-Ion Batteries. *Advanced Energy Materials* **2019**, *9* (33), 1901065.
(276) Zhao, S.; Meng, X.; Zhu, K.; Du, F.; Chen, G.; Wei, Y.; Gogotsi, Y.; Gao, Y. Li-Ion Uptake and Increase in Interlayer Spacing of Nb4C3 MXene. *Energy Storage Materials* **2017**, *8*, 42–48.
(277) Liu, Y.; Wang, W.; Ying, Y.; Wang, Y.; Peng, X. Binder-Free Layered Ti 3 C 2/CNTs Nanocomposite Anodes with Enhanced Capacity and Long-Cycle Life for Lithium-Ion Batteries. *Dalton transactions* **2015**, *44* (16), 7123–7126.

(278) Dong, X.; Guo, Z.; Song, Y.; Hou, M.; Wang, J.; Wang, Y.; Xia, Y. Flexible and Wire-Shaped Micro-Supercapacitor Based on Ni (OH) 2-Nanowire and Ordered Mesoporous Carbon Electrodes. *Advanced Functional Materials* **2014**, *24* (22), 3405–3412.
(279) Zhang, C. J.; Park, S.-H.; Seral-Ascaso, A.; Barwich, S.; McEvoy, N.; Boland, C. S.; Coleman, J. N.; Gogotsi, Y.; Nicolosi, V. High Capacity Silicon Anodes Enabled by MXene Viscous Aqueous Ink. *Nature communications* **2019**, *10* (1), 1–9.
(280) Billaud, J.; Bouville, F.; Magrini, T.; Villevieille, C.; Studart, A. R. Magnetically Aligned Graphite Electrodes for High-Rate Performance Li-Ion Batteries. *Nature Energy* **2016**, *1* (8), 1–6.
(281) Sander, J. S.; Erb, R. M.; Li, L.; Gurijala, A.; Chiang, Y.-M. High-Performance Battery Electrodes via Magnetic Templating. *Nature Energy* **2016**, *1* (8), 1–7.
(282) Liu, J.; Zhang, H. G.; Wang, J.; Cho, J.; Pikul, J. H.; Epstein, E. S.; Huang, X.; Liu, J.; King, W. P.; Braun, P. V. Hydrothermal Fabrication of Three-Dimensional Secondary Battery Anodes. *Advanced Materials* **2014**, *26* (41), 7096–7101.
(283) Wang, X.; Sun, L.; Susantyoko, R. A.; Zhang, Q. A Hierarchical 3D Carbon Nanostructure for High Areal Capacity and Flexible Lithium Ion Batteries. *Carbon* **2016**, *98*, 504–509.
(284) Park, S.-W.; Ha, J. H.; Park, J. M.; Cho, B. W.; Choi, H.-J. 2D Silicon Nanosheets/Carbon Composites Based Foldable Anode Electrode for Lithium-Ion Batteries. *Journal of The Electrochemical Society* **2020**, *167* (2), 020556.
(285) Gulzar, U.; Glynn, C.; O'Dwyer, C. Additive Manufacturing for Energy Storage: Methods, Designs and Materials Selection for Customizable 3D Printed Batteries and Supercapacitors. *Current Opinion in Electrochemistry* **2020**.
(286) Pang, Y.; Cao, Y.; Chu, Y.; Liu, M.; Snyder, K.; MacKenzie, D.; Cao, C. Additive Manufacturing of Batteries. *Advanced Functional Materials* **2020**, *30* (1), 1906244.
(287) Zhu, C.; Liu, T.; Qian, F.; Chen, W.; Chandrasekaran, S.; Yao, B.; Song, Y.; Duoss, E. B.; Kuntz, J. D.; Spadaccini, C. M. 3D Printed Functional Nanomaterials for Electrochemical Energy Storage. *Nano Today* **2017**, *15*, 107–120.
(288) Zhao, J.; Lu, H.; Zhao, X.; Malyi, O. I.; Peng, J.; Lu, C.; Li, X.; Zhang, Y.; Zeng, Z.; Xing, G. Printable Ink Design towards Customizable Miniaturized Energy Storage Devices. *ACS Materials Letters* **2020**, *2*, 1041–1056.
(289) Zhang, J.; Uzun, S.; Seyedin, S.; Lynch, P. A.; Akuzum, B.; Wang, Z.; Qin, S.; Alhabeb, M.; Shuck, C. E.; Lei, W. Additive-Free MXene Liquid Crystals and Fibers. *ACS Central Science* **2020**, *6* (2), 254–265.
(290) Liang, X.; Garsuch, A.; Nazar, L. F. Sulfur Cathodes Based on Conductive MXene Nanosheets for High-Performance Lithium–Sulfur Batteries. *Angewandte Chemie* **2015**, *127* (13), 3979–3983.
(291) Ali, A.; Hantanasirisakul, K.; Abdala, A.; Urbankowski, P.; Zhao, M.-Q.; Anasori, B.; Gogotsi, Y.; Aïssa, B.; Mahmoud, K. A. Effect of Synthesis on Performance of MXene/Iron Oxide Anode Material for Lithium-Ion Batteries. *Langmuir* **2018**, *34* (38), 11325–11334.
(292) Shen, C.; Wang, X.; Zhang, W.; Kang, F. A High-Performance Three-Dimensional Micro Supercapacitor Based on Self-Supporting Composite Materials. *Journal of Power Sources* **2011**, *196* (23), 10465–10471.
(293) Farizhandi, A. A. K.; Khalajabadi, S. Z.; Krishnadoss, V.; Noshadi, I. Synthesized Biocompatible and Conductive Ink for 3D Printing of Flexible Electronics. *Journal of the Mechanical Behavior of Biomedical Materials* **2020**, *110*, 103960.

(294) Farizhandi, A. A. K.; Zhao, H.; Lau, R. Modeling the Change in Particle Size Distribution in a Gas-Solid Fluidized Bed Due to Particle Attrition Using a Hybrid Artificial Neural Network-Genetic Algorithm Approach. *Chemical Engineering Science* **2016**, *155*, 210–220.
(295) Farizhandi, A. A. K.; Pac\lawski, A.; Szlęk, J.; Mendyk, A.; Shao, Y.-H.; Lau, R. Evaluation of Carrier Size and Surface Morphology in Carrier-Based Dry Powder Inhalation by Surrogate Modeling. *Chemical Engineering Science* **2019**, *193*, 144–155.
(296) Farizhandi, A. A. K.; Zhao, H.; Chen, T.; Lau, R. Evaluation of Material Properties Using Planetary Ball Milling for Modeling the Change of Particle Size Distribution in a Gas-Solid Fluidized Bed Using a Hybrid Artificial Neural Network-Genetic Algorithm Approach. *Chemical Engineering Science* **2020**, *215*, 115469.
(297) Nair, S. A.; Alghamdi, H.; Arora, A.; Mehdipour, I.; Sant, G.; Neithalath, N. Linking Fresh Paste Microstructure, Rheology and Extrusion Characteristics of Cementitious Binders for 3D Printing. *Journal of the American Ceramic Society* **2019**, *102* (7), 3951–3964.
(298) Hu, L.-H.; Wu, F.-Y.; Lin, C.-T.; Khlobystov, A. N.; Li, L.-J. Graphene-Modified LiFePO 4 Cathode for Lithium Ion Battery beyond Theoretical Capacity. *Nature communications* **2013**, *4* (1), 1–7.
(299) Wei, W.; Lv, W.; Wu, M.-B.; Su, F.-Y.; He, Y.-B.; Li, B.; Kang, F.; Yang, Q.-H. The Effect of Graphene Wrapping on the Performance of LiFePO4 for a Lithium Ion Battery. *Carbon* **2013**, *57*, 530–533.
(300) Zhao, H.; Lv, J.; Sang, J.; Zhu, L.; Zheng, P.; Andrew, Greg.; Tan, L. A Facile Method to Construct MXene/CuO Nanocomposite with Enhanced Catalytic Activity of CuO on Thermal Decomposition of Ammonium Perchlorate. *Materials* **2018**, *11* (12), 2457. https://doi.org/10.3390/ma11122457.